

In situ investigation of dusty plasmas in the polar E- and D-region

Dissertation
zur
Erlangung des akademischen Grades
doctor rerum naturalium (Dr. rer. nat.)
der Mathematisch-Naturwissenschaftlichen Fakultät
der Universität Rostock

Universität
Rostock



Traditio et Innovatio

vorgelegt von
Heiner Asmus, geb. am 29.07.1986 in Wismar
aus Rostock

Rostock, 22.06.2018

Gutachter: Prof. Dr. Franz-Josef Lübken (Universität Rostock)
Prof. Dr. Jorge Luis Chau (Universität Rostock)

verteidigt am:
26.10.2018

Contents

1	Introduction	1
1.1	The thermal structure of the Earth's atmosphere	2
1.2	The structure of the Earth's ionosphere	3
1.3	Aerosols in the MLT-region	5
1.3.1	Meteor smoke particles	5
1.3.2	Mesospheric ice particles	7
1.4	Objectives and outline of the thesis	8
2	Theoretical background	11
2.1	Small scale structures and turbulent motions	11
2.1.1	Conservative passive tracer	11
2.1.1.1	Neutral density fluctuations as a passive tracer for turbulent motions	11
2.1.1.2	Plasma density fluctuations as a passive tracer for turbulent motions	12
2.1.2	Spectral model method to obtain ϵ and Sc	13
2.1.2.1	Turbulent energy dissipation rate obtained using a spectral model	15
2.1.2.2	Assessment of Schmidt number by means of a spectral model	15
2.1.2.3	Spectral form in the inertial and viscous subrange	16
2.2	Diffusion in a dusty plasma	17
2.2.1	Diffusion coefficient for charged aerosol particles	18
2.2.2	Diffusion coefficient for electrons in the presence of heavy charged particles	19
3	Measurement techniques and instruments	21
3.1	Combined sensor for neutrals and electrons – CONE	21
3.2	Positive ion probe – PIP	22
3.3	IAP particle detector – PD	23
3.4	Wave propagation experiment	24
3.5	Flux Φ Probe Experiment – FIPEX	24
3.6	Airglow Photometer	25
4	Data reduction and analysis techniques	27
4.1	Charge densities	27
4.1.1	Combined aerodynamic and electrostatic simulations	28
4.2	Electron density from an electrostatic probe - CONE	38
4.3	Positive ion densities from a gridded sphere - PIP	39
4.4	Neutral and plasma fluctuations	40

4.5	Particle radii from Schmidt number	40
5	Results 1: WADIS-2 campaign	43
5.1	The WADIS project	43
5.2	Atmospheric background	45
5.3	Heavy charged particles	49
5.4	Densities of plasma constituents	50
5.5	Small scale fluctuations	52
5.6	Spectral analysis	54
5.7	Mean particle sizes	57
5.8	Estimate of a particle size distribution	58
5.9	Absence of PMWE during WADIS-2	61
6	Results 2: Charging model	65
6.1	Estimate of charged particle fraction	66
6.2	Charging model	67
6.3	Model inputs for WADIS-2 condition	69
6.4	The influence of atomic oxygen	72
6.5	Model results for WADIS-2	75
6.5.1	Adjusting model inputs to reproduce WADIS-2 measurements	75
6.5.2	Charged particle size distribution at 82 km	79
7	Discussion	83
7.1	Charge balance	83
7.2	Small scale structures and mean particle radius	84
7.3	Charged particle size distribution	85
7.4	Size dependent layering of charged MSPs	89
7.5	The role of atomic oxygen in the charging process of MSPs	89
8	Summary and Outlook	91
8.1	Summary	91
8.2	Outlook	94
A	WADIS-2	97
A.1	Launch information	97
A.2	Trajectory fit parameter	97
A.2.1	Altitude	97
A.2.2	Latitude	98
A.2.3	Longitude	98
B	WADIS-2 CONE EP spectra fits	99
C	WADIS-2 CONE NP spectra fits	105
D	Uncertainty estimation	111
D.1	Uncertainty of ϵ and Sc	111
D.2	Uncertainty of particle radius	112
D.2.1	Polarization model	112
D.2.2	Hard sphere model	112
E	SIMION Lua user program	113

Chapter 1

Introduction

An estimated 99 % of the known matter in the universe is in an ionized state. The understanding of fundamental processes in plasmas is hence indispensable. Properties of plasmas such as temperature and density can vary over a wide range challenging both experimental as well as theoretical physicists. The investigation of dusty plasmas, also known as complex plasmas, is a fast growing field of study in physics and has become more and more important. One reason for this development is the increasing use of plasma processes in industry. The other reason is the exploration of space. Here dusty plasmas can be found for example in interstellar nebular, planetary rings and comet trails but also in Earth near space, in the Earth's upper atmosphere. A first hint of the plasma layer surrounding our home planet has been achieved in 1901 as a trans-atlantic transmission by radio waves was established by G. Marconi. This layer is called ionosphere and has still an impact on today's communication and localization systems. It is a partly ionized region of Earth's atmosphere created by incoming radiation and high energetic particles. The first observations of ionospheric phenomena were linked to particle precipitation events causing luminous structures in the high latitude atmosphere called *aurora borealis*. It was suggested that there are free electrons and ions in the upper atmosphere creating a conductive layer. Yet it were the experiments with transmitting electromagnetic waves that yielded an insight into the vertical structure of the ionosphere [e.g., Appleton and Barnett, 1925]. The role of dusty plasma in the mesosphere lower thermosphere (MLT) region has become of major interest in the middle atmosphere community in recent years since it is responsible for the formation of a number of phenomena. In the lower ionosphere charged constituents are bound to neutral gas motion via collisions since neutral densities are much larger than plasma densities (typical ratio is neutral to ionized species is $1 \cdot 10^{12}$). Hence, observed plasma parameters can be used to obtain information about the atmosphere acting on the plasma. This makes plasma observations a useful tool to study the MLT region. Neutral winds for instance, can be inferred from drifting plasma trails caused by meteoroids but also from coherent dusty plasma structures [e.g., Elford and Robertson, 1953; Elford and G., 1959; Hocking et al., 2016]. Also turbulence parameters can be estimated using the by enhanced plasma densities backscattered radio signal [e.g., Roper, 1966; Hocking, 1985]. In situ measurements using rockets have high spatial resolution and can thus resolve fluctuations in plasma densities which are also used to estimate turbulence in the MLT region [Lübken et al., 1994; Blix et al., 1990]. However, if charged particles are used to monitor neutral dynamics, the understanding of the underlying physics of dusty plasma in the middle atmosphere is a key task. This includes properties of charged aerosols and their impact on the other plasma constituents. A huge effort has been made to elucidate the role of dusty plasma in the MLT region [e.g., Cho et al., 1992; Lübken et al., 1994; Havnes et al., 2001; Havnes and Kassa, 2009; Havnes et al., 2011; Rapp, 2003; Rapp et al., 2005, 2010;

Robertson *et al.*, 2009, 2014]. Since it is a great challenge to investigate this part of atmosphere there are still open questions which have to be tackled. This work aims at a contribution in this fascinating and challenging field of research. For the rest of this introductory chapter the atmosphere and ionosphere will be briefly described. Additionally, the topic of aerosol particles in the MLT region will be elucidated.

1.1 The thermal structure of the Earth’s atmosphere

The gaseous layer around our home planet is indispensable for the existence of life on Earth. First of all it provides essential substances for life and protects us from highly energetic radiation and particles having their origin in the Sun and space. In the so called *homosphere* which is the part of the atmosphere from 0 to roughly 100 km, the main constituents are molecules of nitrogen (78 %) and oxygen (21 %) as well as atomic argon (0.9 %) [Brasseur and Solomon, 2005]. It is a region of constant mean molecular mass. Exceeding the *turbopause/homopause* which is the transition to the *heterosphere* where atmospheric composition starts demixing and lighter species such as atomic oxygen, helium and hydrogen become more abundant. A more common way of dividing the atmosphere is obtained by classifying layers defined by temperature gradients. Fig. 1.1 shows temperature profiles for summer (red) and winter (blue) for 69° N obtained from the model NRLMSISE-00 [Picone *et al.*, 2002]. The profiles show local maxima and minima also called pauses which are used to define the boundary of the individual layers. The lowermost layer is the *troposphere* which contains 75 % of the atmospheric mass and is place of weather phenomenas we experience every day. In the troposphere temperature is decreasing with approximately the moist adiabatic lapse rate $\frac{dT}{dz} \approx 6.5 \text{ K km}^{-1}$ until temperature increases again. This layer is called *stratosphere* and is governed by photochemical processes and ~20 % of the mass is placed inside this layer. UV light from the Sun is absorbed mainly by ozone which heats this region and yields a positive temperature gradient. The ozone layer protects us against harmful radiation coming from the Sun. The next layer further up is called *mesosphere* and is again characterized by a negative temperature gradient until it reaches a minima. The high latitude *mesopause* shows the coldest temperatures found on Earth in summer which is caused by a residual circulation driven by breaking gravity waves [e.g., Becker and Schmitz, 2003]. This is counter-intuitive when considering just balance by radiative heating. However only dynamics can explain the low temperatures (~130 K) found in the mesopause region [Lübken *et al.*, 1990; Becker and Schmitz, 2003]. Even though 99 % of the water vapor is in the troposphere, there

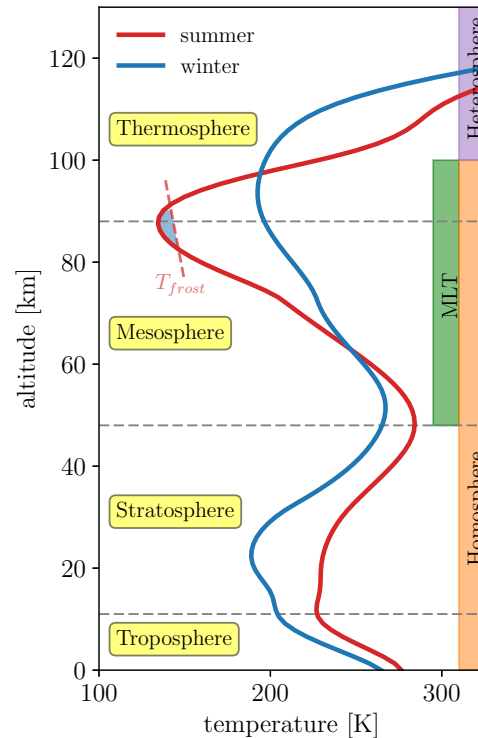


Figure 1.1: Atmospheric layers, temperature profiles for July the 1st, 2013 (summer) and January the 1st, 2013 (winter) for 69° N and 16° E [Picone *et al.*, 2002]. Red dashed line indicates the frostpoint temperature for a water mixing ratio of 5 ppmv.

can be ice clouds called *noctilucent clouds* (NLC) in the summer mesopause region [Leslie, 1885; Jesse, 1896]. This is possible when the temperature is colder than the frost point temperature which depends on pressure and water vapor mixing ratio. In the summer mesopause the water vapor mixing ratio is between 2 and 10 ppmv [e.g., Grossmann et al., 1987]. In Fig. 1.1 the region where ice particles can evolve is marked by the blue area around the mesopause. Mesospheric aerosols are described in more detail in Sec. 1.3. Above the mesosphere the *thermosphere* begins, showing a rapid temperature increase which maximizes and remains constant above 500 km. Depending on the solar activity temperatures can reach values around ~ 1000 K [e.g., Schunk and Nagy, 2004]. In this region photodissociation leads to the destruction of molecular nitrogen as well as oxygen and the atmosphere is changing its composition. The mesosphere and lower thermosphere (MLT) region is a place of large interest since it is coupled to the layers below and to incoming radiation. The latter causes a part of the MLT region to be in a low dense cold plasma state as neutral compounds are ionized and have a long enough life time. This ionized part of the Earth's atmosphere is called ionosphere and will be elucidated in the subsequent section.

1.2 The structure of the Earth's ionosphere

Like the neutral part of the atmosphere can be layered by its thermal structure, one can divide the ionosphere by its electron density structure. Fig. 1.2 shows typical electron density profiles for day and night time over northern Norway. The lowermost layer is the *D*-region expanding from roughly 60 km to 90 km which is usually most prominent during daytime and is created mainly by solar Lyman- α (121.6 nm) radiation. However, during so called polar cap absorption (PCA) events high energetic solar protons can penetrate deep into the atmosphere and increase ionization in the *D*-region. Next up is the *E*-region located between 90 and up to 150 km. Solar extreme ultra violet (EUV) and X-rays are responsible for the creation of this layer. In this altitude range, sporadic layers E_s of enhanced electron density might evolve having their origin in locally increased ionization [Schunk and Nagy, 2004]. Both *D* and *E*-region are controlled by chemical processes and molecular ions are most abundant. Heavier cluster ions dominate in the *D*-region up to a transition height of 85 km being formed by hydrated NO^+ , O_2^+ [Friedrich and Torkar, 1988]. Chemical reactions involve up to three bodies and also negative ions can exist [Schunk and Nagy, 2004; Thomas and Bowman, 1985]. Dominant ions in the *E*-region are NO^+ , O_2^+ and N_2^+ and reactions involve only two bodies. The region with the largest density of free electrons is found higher up and is called *F*-region extending

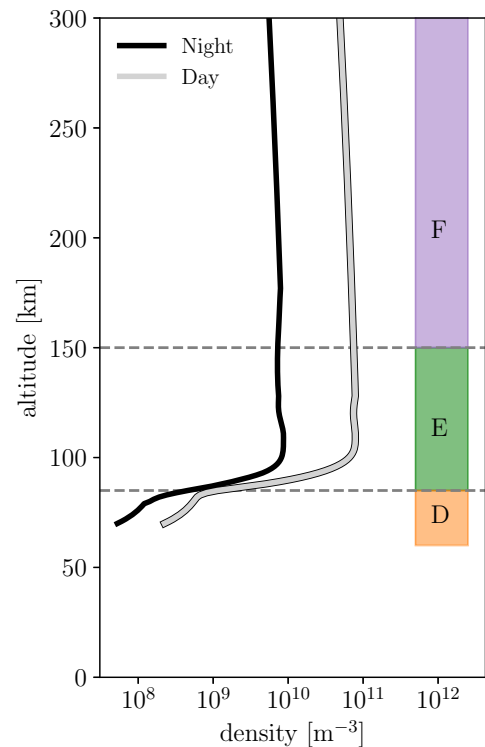


Figure 1.2: Annual mean electron density profiles for day (light gray) and night (black) above 69° N and 16° E of 2015 [Bilitza et al., 2014]. Altitude range of main ionospheric layers are marked by colored patches.

from approximately 150 km to 500 km. Whereas during night time this layer has only one distinct maximum near 300 km, during day time the layer divides into two separate layers called F_1 and F_2 having their maxima around 250 and 300 km, respectively. The region above the F_2 electron density peak is known as the *topside ionosphere*.

The transmission of electro magnetic waves through a plasma is depending on electron density. Electromagnetic waves with frequencies larger than the corresponding F_2 -peak plasma frequency can leave the ionosphere. The plasma frequency is the cyclic frequency at which the electron density is oscillating around a mean density and is defined as [e.g., *Schunk and Nagy, 2004*]

$$\omega_p = \sqrt{\frac{n_e e^2}{\epsilon_0 m_e}} \approx 56.41 \cdot \sqrt{n_e}, \quad (1.1)$$

where n_e is the electron density in m^{-3} , e is the elementary charge, ϵ_0 is the vacuum permittivity and m_e is the electron mass. By means of Eq. 1.1 one can retrieve the electron density as a function of altitude using different frequencies. This is done by means of ionosondes, which are antennas able to sweep through a wide range of frequencies. Electromagnetic waves are reflected as their frequency approaches the plasma frequency ω_p . By means of the time it takes for the reflected signal to return to the transmitter one can obtain altitude information.

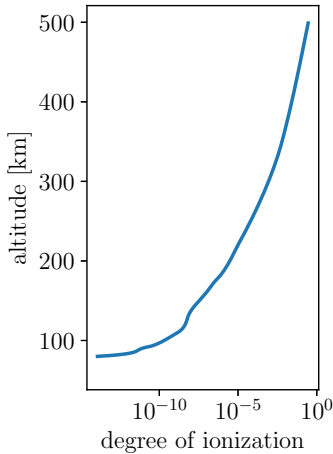


Figure 1.3: Fraction of plasma with respect to the neutral density $\alpha = \frac{n_e}{n_n}$ calculated using NRLMSISE-00 and IRI data for March 5th 2015 [*Picone et al., 2002; Bilitza et al., 2014*].

In contrast to e.g. fusion plasmas the ionospheric plasma is of low density and cold. Typical values for electron densities are in the range of $1 \times 10^7 \text{ m}^{-3}$ to $1 \times 10^{12} \text{ m}^{-3}$ and temperatures from 120 K to 1000 K. For most of the ionosphere neutral gas density by far exceeds the charged fraction by several orders of magnitude. The density ratio of charged to neutral species is called degree of ionization which is shown in Fig. 1.3 as diurnal mean for March the 5th of 2015. At lower altitudes e.g., in the D -region the charged species are collisional dominated by neutral molecules causing them to be in thermal equilibrium and follow the neutral flow. With increasing altitude this effect diminishes and electric as well as magnetic field effects gain importance. At polar regions the Earth's magnetic field lines are almost perpendicular to the surface, which causes streams of energetic solar particles to enter the ionosphere predominately at high latitudes. The charged particles are moving with the magnetic field lines and gyrate due to the Lorentz force with a frequency ω_c . For e.g., electrons this frequency is given by [e.g., *Schunk and Nagy, 2004*]

$$\omega_c = \frac{|e| \hbar}{m_e} B, \quad (1.2)$$

where B is the magnetic field strength. However this is negligible for the lower part of the ionosphere as the collision frequency with neutrals is much larger.

A fundamental property of plasmas is to be quasi neutral if the Debye length is much smaller as the plasma dimensions. The Debye length describes the scale below which the electric field of a single charge is shielded by particles of the opposite polarity. Charge

neutrality can be expressed in terms of densities of the plasma constituents by

$$\sum_j N_j = 0, \quad (1.3)$$

where the subscript j stands for the j^{th} plasma constituent. This balance is valid if one includes all charge carriers in the ionosphere. It has been shown that charge balance not always can be achieved by electrons and ions alone [e.g., *Friedrich et al.*, 2011]. In the subsequent section we will have a look at aerosols in the MLT region. These aerosols can carry a large part of the charges and therefore are of great importance for the lower ionosphere.

1.3 Aerosols in the MLT-region

Aerosols play an important role in the formation of mid and high latitude mesospheric phenomena such as noctilucent clouds (NLC) and radar echoes known as polar mesospheric summer echoes (PMSE). Additionally, they influence the charge balance of the lower E- and D-region of the ionosphere. In this section a brief overview of meteor smoke and mesospheric ice particles is given.

1.3.1 Meteor smoke particles

The Earth's atmosphere is permanently bombarded by meteoroids. Their velocity is in the range of 11 to 72 km s⁻¹ and they ablate typically in an altitude range between 70-140 km [e.g., *Schult et al.*, 2013]. These meteoroids can be either of sporadic origin or be part of meteor shower events. Sources for sporadic meteors which are a rather constant background are the asteroid belt between the orbits of Mars and Jupiter whereas shower meteors are remains of comets forming a dust cloud whose trajectory intersects with the Earth's orbit. The quantification of mass flux of extraterrestrial material by meteoroids onto the Earth is difficult and varies strongly depending on the measurement method. The values quoted in the literature are in the range of 5 to 250 tons per day [e.g., *Dohnanyi*, 1970; *Hughes and W.*, 1975; *Millman and M.*, 1975; *Love and Brownlee*, 1993; *Cepelcha et al.*, 1998; *Mathews et al.*, 2001]. Entering the Earth's atmosphere the meteors heat up and lose material (especially metal atoms) due to differential ablation [*McNeil et al.*, 1998]. The ablated material is the source of metal layers (e.g., Na, Fe, Mg) which can be found in the MLT region globally [*Plane et al.*, 2003]. They can be studied e.g., by resonant backscatter lidar methods [e.g., *Gardner et al.*, 1986; *Granier et al.*, 1989; *Von Zahn and Hansen*, 1988; *Clemesha*, 1995]. The remnants of the meteors can recondensate and form so-called meteor smoke particles (MSPs) [e.g., *Rosinski and Snow*, 1961; *Hunten et al.*, 1980; *Arnold and Viggiano*, 1982; *Arnold et al.*, 1982; *Megner et al.*, 2006; *Vondrak et al.*, 2008]. The composition of these MSPs is not yet verified, but there is a strong indication from laboratory experiments as well as satellite measurements that they consist of olivine, hematite, magnesium-iron-silicates [*Saunders and Plane*, 2006; *Saunders et al.*, 2010], wüstite or magnesio-wüstite [*Hervig et al.*, 2012]. The existence of MSPs was mainly shown by rocket borne measurements in an altitude range between 75 to 100 km [e.g., *Arnold and Viggiano*, 1982; *Arnold et al.*, 1982; *Gelinas et al.*, 1998; *Lynch*, 2005; *Rapp et al.*, 2005, 2008, 2011; *Robertson et al.*, 2014]. The lower height limit is set by aerodynamic limitations of rocket measurements and other instrumental constraints rather than by geophysical reasons. In addition, MSP properties were obtained by remote sensing techniques such as incoherent scatter radars and solar occultation [*Rapp et al.*, 2007; *Strelnikova et al.*, 2007; *Fentzke et al.*,

during night and more positively charged MSPs during day time.

Despite the enormous efforts made in the past, there are still open questions to clarify the role of MSPs in the MLT region. The size distribution of charged and neutral MSPs for example is still not well understood. The role of charged MSPs in electron diffusivity is also not known and needs to be investigated. Both questions will be tackled in the course of this work.

Besides MSPs there can be ice particles in the mesosphere being part of the lower ionosphere dusty plasma. In the following section the phenomenon of mesospheric ice particles is elucidated.

1.3.2 Mesospheric ice particles

Water ice can only exist if the temperature is below the so-called frost point temperature T_{frost} , i.e., the temperature where the ratio of specific humidity and saturation humidity of water vapor is equal to one. In the mesosphere this criterion is fulfilled for the polar mesopause region around summer solstice when the temperature reaches approximately 140 K [Rapp and Thomas, 2006]. Ice particles in the mesosphere emerge by heterogeneous nucleation, i.e., growing by deposition of water molecules on the surface of a nuclei. Furthermore, there are also other mechanisms such as homogeneous nucleation. Nucleation induced by ions or strongly bipolar molecules may be possible [Witt, 1969; Gumbel et al., 2003; Plane, 2000; Murray and Jensen, 2010]. The positive proof that water ice is the primary component of mesospheric ice particles was first provided by Hervig et al. [2001]. A number of candidates have been under debate serving as a nuclei for heterogeneous nucleation. However, most studies in the past assumed MSPs to be the most likely candidate for serving as nuclei. The nucleation process is still under investigation as numerous questions remain open. One specific question came up whether the nuclei temperature is different from the background and if so what the impact on ice nucleation might be. Therefore micro physical modeling of nucleation rates for non isothermal growth have been performed, showing that the nuclei temperature is critical for the nucleation rate [Asmus et al., 2014]. A difference of particle temperature to the ambient gas temperature by 1 K decreases the nucleation rate by five orders of magnitude. This effect seems to be stronger if the relative iron content of the MSP is higher [Asmus et al., 2014]. These effects are currently under investigation for example in laboratory experiments described in Duft et al. [2015] but also by complex modeling [Wilms et al., 2016].

As the ice particles grow from nuclei of nanometer size their radii span from those small values to roughly 100 nm [e.g., Rapp and Thomas, 2006; von Cossart et al., 1999; Berger and von Zahn, 2002]. Particles with large sizes can be seen by naked eye as the so called "Noctilucent clouds" (NLC) first observed in the late 19th century by e.g., Jesse [1885]; Backhouse [1885]; Tseraskii [1890]; Foerster and Jesse [1892]; Archenhold [1894]. From modern Lidar-measurements it is known, that the mean altitude of those clouds above Andøya is at a surprisingly stable altitude of 83.20(2) m [Fiedler et al., 2009]. One essential condition to see NLC by naked eye is the Sun is a few degrees below the horizon which is fulfilled in summer in mid and high latitudes after dusk around midnight. By optical observation one can achieve a glance at ongoing dynamical processes since the ice particles are moving with the background flow. Evolution of NLCs and ice particle trajectories have been studied by models to elucidate

the influence of background atmosphere on the existence of NLC [e.g., *Berger and von Zahn, 2002, 2007*]. Gravity wave activity, for example, limits the growing time of ice particles due to the balance of sedimentation and vertical winds [*Wilms et al., 2016*]. Horizontal winds transport the ice particles from their origin of nucleation from high to lower latitudes where they sublime again [*Berger and von Zahn, 2007*]. The shape of those particles are thought to be mainly disc like but also needles are possible [*Baumgarten and Fricke, 2002; Kiliani et al., 2015*].

Immersed in the ionospheric plasma mesospheric ice particles can be charged. This has been shown by rocket-borne measurements by e.g., *Havnes et al. [1996]* and *Rapp et al. [2009]* but also model calculations indicate that icy particles becoming charged is likely [e.g., *Reid, 1990; Rapp and Lübken, 2001; Rapp and Thomas, 2006*]. The number of charges the particle can carry depends on its size. Model calculations showed for radii smaller than ~ 8 nm the maximum number of charges is one whereas larger particles can have more charges [*Rapp and Lübken, 2001*]. Whereas larger ice particles (≥ 50 nm) can be observed by naked eye, lidars observe particles down to >30 nm and the smallest particles have radii in the order of 1 nm. Charged ice particles are responsible for strong radar returns between 80 km to 90 km which are called polar mesospheric summer echoes PMSE [e.g., *Cho et al., 1992; Röttger et al., 1988; Rapp and Lübken, 2004*]. Coupled to the neutral dynamics via collisions the particles follow turbulent motions. However, due to their larger mass they are forced to smaller scales as neutral molecules. Since the ice particles are charged all remaining plasma constituents are connected to them via Coulomb forces [*Rapp et al., 2008*]. Electrons and ions are bound to the heavier particles motion and therefore reproduce the small scale turbulent structures. Backscattered radar signals are large when these structures fulfill the Bragg-criteria i.e. have dimensions of half the radar wavelength. Those events have high occurrence rates of up to $\sim 100\%$ in June to July for the Northern hemisphere [*Latteck and Bremer, 2013*].

1.4 Objectives and outline of the thesis

This thesis aims at the investigation of properties of dusty plasma constituents in the polar MLT region. In the course of this general objective, several more detailed questions will be addressed in this work:

1. Do charged dust particles alter the response of free electrons to neutral turbulent motions in winter?
2. Which dust sizes contribute to charged fraction of the dust ensemble? How is the shape of their size distribution?
3. Can smallest charged dust particles explain huge electron depletions above 80 km?
4. How does atomic oxygen impact the charging of MSP?

In order to answer the above questions this thesis is structured in the following way, whereas partial results of the present work were published in *Asmus et al. [2017]*:

In Chapter 1 basic information about atmospheric structure, The Earth's ionosphere and aerosols in the MLT region are given. Theoretical concepts essential for the presented work are recapitulated in Chapter 2. In Chapter 3 rocket borne instruments which were used

in the course of this work to obtain physical parameters are described technically. In the following Chapter 4 the derivation of physical parameters like particle density for the main instruments is presented as well as instrumental limitations. Additionally, an extended method to derive mean charge particle radii. In Chapter 5 the results of the WADIS-2 sounding rocket campaign are presented. This includes a campaign description, background conditions, charged particles and plasma measurements, small scale fluctuations and spectral analysis, particle sizes and size distribution and absence of radar echoes. A charging model is presented and applied to WADIS-2 results in Chapter 6. First of all the model is described briefly. In Chapter 7 all results are discussed with respect to established and recent research. Finally the results are summarized and the questions raised above are answered point by point in Chapter 8. Here also an outlook and open questions are given.

Chapter 2

Theoretical background

2.1 Small scale structures and turbulent motions

Turbulent fields are characterized by fluctuations in the velocity field. Observations of turbulence in the MLT region are generally difficult. In situ measurements of neutral gas velocity for example are not possible yet because of instrumental limitations. Hence, in order to obtain turbulent parameters one can look at the consequences of turbulence in the atmospheric gas or just in parts of its constituents. One method is the measurement of turbulent induced fluctuations in a conservative and passive tracer.

2.1.1 Conservative passive tracer

Conservative in this context means that the tracer remains constant over time and does not e.g. decay or react chemically. Tracers are passive if they do not influence the flow by changing for example its density or viscosity. Conservative and passive tracers used for in situ turbulence measurements in the MLT region are for example

1. neutral density fluctuations [Lübken, 1992]
2. electron density fluctuations [Lübken et al., 1998]
3. positive ion density fluctuations [Blix et al., 1990]
4. charged aerosol density fluctuations [Strelnikov et al., 2009]

2.1.1.1 Neutral density fluctuations as a passive tracer for turbulent motions

Let us first consider neutral density fluctuations. If a neutral air parcel is moved adiabatically in vertical direction by Δz , there will be a relative change in density with respect to the background density given by [Thrane and Grandal, 1981; Lübken, 1992]

$$\frac{\Delta n}{n} \approx \left(\frac{1}{H_n} - \frac{1}{\gamma H_p} \right) = \frac{\omega_B^2}{g} \Delta z, \quad (2.1)$$

where n is the background density and Δn its fluctuations, H_n and H_p are the density and pressure scale height, respectively. The ratio of the specific heat capacities is given by $\gamma = c_p/c_v$ and g is the Earth's gravitational acceleration. ω_B is the Brunt-Väisälä frequency given by

$$\omega_B = \sqrt{\frac{g}{T} \left(\frac{\partial T}{\partial z} + \frac{g}{c_p} \right)}, \quad (2.2)$$

where $\frac{\partial T}{\partial z}$ is the vertical temperature gradient and $\frac{g}{c_p}$ is the adiabatic lapse rate. Neutral density fluctuations in the middle atmosphere are typically in the order of 0.1% to 1% [Lübken, 1992].

The power spectral density of the neutral density fluctuations can be described by a model under the assumption that the driving turbulence is homogeneous, isotropic and stationary. One spectral model for example was developed by Heisenberg [1948]. In the frame of this study this model is used to deduce turbulent parameters from neutral density fluctuations such as the turbulent energy dissipation rate ε . This rate is a measure of the conversion of kinetic energy into heat and hence gives the "strength" of turbulence. It is defined by [e.g., Landau and Lifschitz, 1991]

$$\varepsilon = \frac{\nu}{2} \overline{\left(\frac{\partial u_i}{\partial x_j} \right)^2}, \quad (2.3)$$

where ν is the kinematic viscosity, u_i is the i -th coordinate of velocity and x_j is the j -th cartesian component. By comparing the spectral model with the measured spectra one can obtain ε . Used spectral models and the method to obtain physical parameter are described in Sec. 2.1.2.

2.1.1.2 Plasma density fluctuations as a passive tracer for turbulent motions

As the MLT plasma is dominated by collisions electrons are bound to the motions of neutral gas flow. Thus, the plasma constituents will also show density fluctuations in regions of neutral turbulence as they are coupled to the background flow. This interaction is mainly driven by ions which are transported by turbulent air packages. Free electrons follow those ions as they are bound to them by Coulomb force. However, the amplitude of density fluctuations in neutrals and charged species is not equal. They are related by an factor F given by [Thrane and Grandal, 1981; Giebeler, 1995]

$$\begin{aligned} \frac{\Delta n}{n} &= F \frac{\Delta n_{i/e}}{n_{i/e}}, \\ F &= \frac{\frac{\gamma H_p}{H_n} - 1}{\frac{\gamma H_p}{H_{i/e}} - 1}, \end{aligned} \quad (2.4)$$

where the indexes i/e denote ions and electrons, respectively. $H_{i/e}$ is the ion/electron density scale height. Fluctuations of neutral and plasma density may also reveal a phase delay as the plasma is also influenced by photochemical processes. The phase delay can be written as [Thrane et al., 1994; Fritts and Thrane, 1990]

$$\varphi_i = \tan^{-1} \left[\frac{\beta \left(\frac{1}{2} - \frac{1}{F} \right)}{\frac{1}{2} + \frac{\beta^2}{F}} \right] \quad (2.5)$$

where the variable β is defined by

$$\beta = 2\pi \frac{\tau_i}{\tau_w}, \quad (2.6)$$

where τ_i is the time constant for recombinations of ions and τ_w is the period of a wave introducing perturbations in the plasma density. The fluctuations of ion and neutral density are in anti-phase ($\varphi_i = \pi$) if adiabatic motions dominate and photochemical processes can be neglected. They are in phase ($\varphi_i = 0$) if photochemical processes dominate [Fritts and

Thrane, 1990; Thrane et al., 1994].

Typical values of fluctuation amplitudes are e.g., for electron density fluctuations in the order of $\sim 5\%$ [Lübken et al., 1994]. However, it was shown by e.g., Lübken et al. [1994] that the spectral behavior of the electron density fluctuations may not necessarily be the same as for the neutral constituents. This can be addressed to the presence of heavy charged particles changing the diffusivity D of electrons [e.g., Hill, 1978; Cho et al., 1992; Rapp, 2003]. Spectral models accounting for the dependence of the electron diffusivity were developed by e.g., Batchelor [1959] and Driscoll and Kennedy [1985]. In the frame of this work the latter model is used to obtain the electron Schmidt number which is generally defined by

$$Sc = \frac{\nu}{D}, \quad (2.7)$$

where ν is the kinematic viscosity of air and D is the diffusivity of the tracer. The method of obtaining the Schmidt number from electron density fluctuations is described in the following section.

2.1.2 Spectral model method to obtain ε and Sc

A turbulent spectrum describes a so-called energy cascade or rather the conversion of the energy input at larger scales into smaller eddies right up to the molecular diffusion. Fig. 2.1 illustrates the shape of a turbulent spectrum as a function of wavenumber.

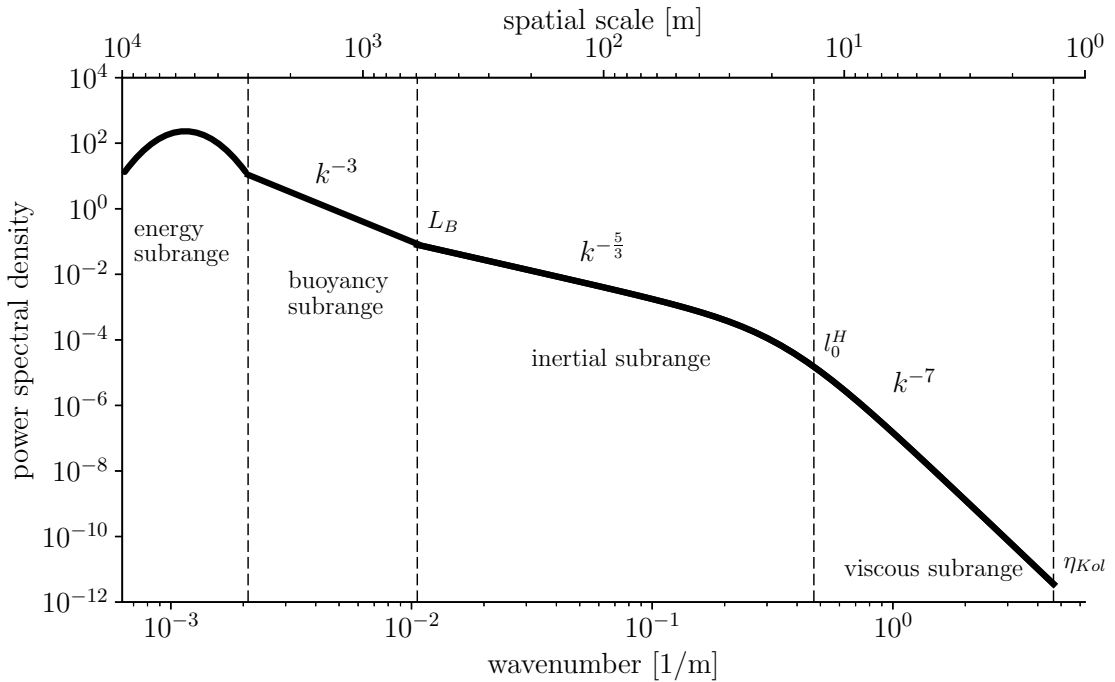


Figure 2.1: Turbulent energy spectrum for typical mesospheric values with its subranges calculated for scales smaller than the outer scale L_B by the Heisenberg [1948] model using a kinematic viscosity of $\nu = 1 \text{ m}^2 \text{ s}^{-1}$ and a turbulent energy dissipation rate $\varepsilon = 0.3 \text{ W K}^{-1}$. The power law for each subrange is indicated.

The subrange at which energy is injected is called energy subrange and in the mesosphere can be found at scales larger than $\sim 3000 \text{ m}$. Next comes the buoyancy subrange where energy

change with k^{-3} and turbulent motions have gravity wave like characteristics in the case of strong static stability. Both subranges are usually not seen in fluctuation analysis due to trend removals. The scale at which transition to the subsequent inertial subrange occurs is called *outer scale* L_B which is defined as [Weinstock, 1978; Lübken, 1992]

$$L_B = 9.97 \left(\frac{\varepsilon}{\omega_B^3} \right)^{\frac{1}{2}}, \quad (2.8)$$

where ε is the turbulent energy dissipation rate and ω_B is the Brunt-Väisälä frequency. In the inertial subrange energy is transported to smaller scales whereas the amplitude per scale decrease with $k^{-5/3}$ until the viscous subrange is reached. The scale of transition is called *inner scale* l_0 . The smallest scale of a turbulent flow in the case that density fluctuations projects the velocity fluctuations of the flow ($v \approx D$), is the *Kolmogorov* microscale η_{Kol} . It is defined by the kinematic viscosity ν and the energy dissipation rate ε by the relation

$$\eta_{Kol} = \left(\frac{\nu^3}{\varepsilon} \right)^{\frac{1}{4}}. \quad (2.9)$$

In the case of $\nu \gg D$ or $\nu \ll D$ the smallest scale of turbulent motion of the tracer is defined by the *Batchelor* scale η_{Ba} which is connected to the *Kolmogorov* microscale via

$$\eta_{Ba} = \frac{\eta_{Kol}}{\sqrt{Sc}}. \quad (2.10)$$

For Schmidt numbers larger than one η_{Ba} is smaller than η_{Kol} meaning that the tracer is structured to smaller scales than the velocity fluctuations of the flow. Theoretical models of such turbulent spectra are used to obtain physical parameters from in situ measured density fluctuation spectra such as the turbulent energy dissipation rate and the dimensionless Schmidt number [Lübken, 1992, 1993; Giebler *et al.*, 1993]. In the use of those rocket-borne instruments one usually assumes the turbulent field to be "frozen" for the time (~ 1 s) the rocket passes the field. This condition is fulfilled since life time of turbulent processes are in the order of 10 s to 100 s [Thrane and Grandal, 1981]. Generally, a single instrument on a rocket cannot resolve the three dimensional turbulent field. One usually obtains a one dimensional time series of density fluctuations along the rocket's path. Therefore the three dimensional power spectrum $\Phi_{\vartheta}(k)$ of fluctuations of tracer ϑ is transformed into a one dimensional spectrum in the rocket's frame of reference using the relation $k = \omega/v_R$ [Tatarskii, 1971],

$$W_{\vartheta}(\omega) = \frac{2\pi}{v_R} \int_{\frac{\omega}{v_R}}^{\infty} \Phi_{\vartheta}(k) k dk. \quad (2.11)$$

The power spectrum describes the contribution of a spatial scale to the variance of the tracer in isotropic turbulence. It is therefore normalized to the variance $\langle \vartheta'^2 \rangle$ as

$$\langle \vartheta'^2 \rangle = \int_{-\infty}^{\infty} W_{\vartheta}(\omega) d\omega, \quad (2.12)$$

where $\vartheta' = \vartheta - \bar{\vartheta}$ is the fluctuation of a local value from a mean.

2.1.2.1 Turbulent energy dissipation rate obtained using a spectral model

The first spectral model used in the course of this work describing the energy for high wavenumbers, i.e. in the dissipation regime is the model of *Heisenberg* [1948]. It obeys the classical $k^{-5/3}$ power law in the inertial subrange of the spectrum where turbulent motions, so called eddies, are larger than eddies in the viscous subrange. Here energy decays with k^{-7} . The one dimensional power spectrum in frequency space is given by

$$W_{\vartheta}(\omega) = \frac{\Gamma(5/3) \sin(\pi/3)}{2\pi v_R} \cdot C_n^2 \cdot f_a \cdot \frac{(\omega/v_R)^{-5/3}}{\left[1 + \{(\omega/v_R)/k_0\}^{8/3}\right]^2}. \quad (2.13)$$

where $\Gamma(5/3) = 0.902745$ is the Gamma function, v_R is the rockets velocity, $\omega = 2\pi f$ is the cyclic frequency in the rocket frame of reference. The structure function constant C_n^2 is defined as

$$C_n^2 = a^2 \frac{N_{\vartheta}}{\varepsilon^{1/3}}, \quad (2.14)$$

where $a^2 = 1.74$ is a constant [Lübken, 1992], N_{ϑ} is the rate at which fluctuations in the tracer are produced or destroyed, i.e. variability dissipation rate, ε is the turbulent energy dissipation rate which can be related to a heating rate by $h = \varepsilon/c_p$ ($c_p \approx 1004 \text{ J kg}^{-1} \text{ K}^{-1}$ is the heat capacity of air at constant pressure). f_a in Eq. 2.13 is a constant and for density fluctuations has a value of 2 according to Lübken [1993]. The turbulent kinetic energy dissipates into heat when molecular diffusion sets in. In the case of the *Heisenberg* spectrum this happens when $k_0 \equiv \omega_0/v_R$ which is the intersection between inertial and viscous subrange of the spectrum. The equivalent scale to k_0 is called *inner scale* l_0^H which are related as $l_0^H = \frac{2\pi}{k_0}$. The *inner scale* is defined for the *Heisenberg*-model as [Lübken, 1992]

$$l_0^H = 9.90 \cdot \eta_{Kol}. \quad (2.15)$$

Using Eq. 2.9, 2.14, 2.15 and $\omega = 2\pi f$ one can write the spectral function from Eq. 2.13 as

$$W_{\vartheta}(f) = \frac{\Gamma(5/3) \sin(\pi/3)}{2\pi v_R} \cdot a^2 \frac{N_{\vartheta}}{\varepsilon^{1/3}} \cdot f_a \cdot \frac{(2\pi f/v_R)^{-5/3}}{\left[1 + \left(\frac{9.90 \cdot f}{v_R} \left(\frac{v^3}{\varepsilon}\right)^{1/4}\right)^{8/3}\right]^2}. \quad (2.16)$$

The model described by Eq. 2.16 is fitted to the measured neutral density fluctuation spectrum. The unknown parameters are N_{ϑ} and ε . Typical values for N_{ϑ} for neutral density fluctuations from rocket measurements are in the order of $1 \times 10^{-6} \text{ s}^{-1}$ to $1 \times 10^{-8} \text{ s}^{-1}$ [Lübken, 2014].

2.1.2.2 Assessment of Schmidt number by means of a spectral model

To describe the spectral behavior of plasma density fluctuations a model is needed which depends on the Schmidt number in the viscous subrange of the spectrum [e.g., Giebeler et al., 1993; Lübken et al., 1994]. One model fulfilling this criterion is described in detail in *Driscoll and Kennedy* [1985]. An applicable version of this model can be obtained by transformation of the original series expansion by *Driscoll and Kennedy* [1985] into an integral form [Giebeler, 1995]. Furthermore, the energy spectrum $W_{\vartheta}^{D\&K}$ is normalized by the energy dissipation rate ε , the *Kolmogorov* microscale and a constant

$$\epsilon_{\vartheta} = \frac{4\pi AN_{\vartheta}}{\alpha\beta},$$

where $\alpha = 0.83$ and $\beta = 1$. The normalized one dimensional power spectrum is then defined as

$$\tilde{W}_{\vartheta}^{D\&K}(k) = \frac{W_{\vartheta}^{D\&K}(k)}{\epsilon_{\vartheta} \varepsilon^{-\frac{1}{3}} \eta_{Kol}^{\frac{5}{3}}}. \quad (2.17)$$

In the next step a variable y is introduced for simplification

$$y = Q^{\frac{3}{2}} \eta_{Kol} k, \quad (2.18)$$

where $Q = 2$ is a constant [Driscoll and Kennedy, 1985]. Subsequently $\tilde{W}_{\vartheta}^{D\&K}(k)$ is transformed to $\tilde{W}_{\vartheta}^{D\&K}(y)$ which introduces further simplification. The one dimensional power spectrum from the *Driscoll-Kennedy*-model reads [Giebeler, 1995]

$$\tilde{W}_{\vartheta}^{D\&K}(y) = \frac{1}{2v_R} A_1 \beta \int_{y_w}^{\infty} \frac{y}{y_{\vartheta}^2 + y^2} \left((y_{\vartheta}^2 + y^2)^{-\frac{5}{6}} + (y_{\vartheta}^2 + y^2)^{-\frac{1}{2}} \right) \cdot \exp \left[-A_{3\vartheta} \left(\frac{3}{2} (y_{\vartheta}^2 + y^2)^{\frac{4}{6}} + y_{\vartheta}^2 + y^2 \right) \right], \quad (2.19)$$

where $A_1 = \alpha Q^{\frac{5}{2}}$ and $A_{3\vartheta} = \frac{\alpha}{Q^2 Sc}$. The variable $y_{\vartheta} = y(k_0)$ which yields $y_{\vartheta} = Q^{\frac{3}{2}} \eta_{Kol} k_0$. The energy in the *Driscoll and Kennedy*-model also decays with a slope of $-5/3$ in the inertial subrange. In contrast to the *Heisenberg*-model the viscous subrange for the *Driscoll and Kennedy*-model is subdivided into a viscous convective and a viscous diffusive subrange. The energy in the viscous convective subrange decays with k^{-1} whereas in the viscous diffusive subrange the decay is exponentially. The inner scale of the *D&K*-model $l_0^{D\&K}$ is the scale at which the transition into the diffusive subrange occurs. It is defined as the deviation from the power slopes of $-5/3$ and -1 by a factor of $1/e^2$ [Lübken et al., 1994]. $l_0^{D\&K}$ can be found by solving the relation

$$\frac{1}{e^2} \left(\frac{1}{y_w} + \frac{3}{5} y_w^{-5/3} \right) = \int_{y_w}^{\infty} \left(\frac{1}{y^2} + y^{-8/3} \right) \exp \left[-\frac{\alpha}{Q^2 Sc} \frac{3}{2} \left(y^{4/3} + y^2 \right) \right] dy, \quad (2.20)$$

where $y_w = Q^{3/2} \eta_{Kol} k_0$ and $k_0 = 2\pi/l_0^{D\&K}$ [Lübken et al., 1994].

The Schmidt number Sc can now be obtained by using the energy dissipation rate from the neutral density fluctuations as a fixed parameter and the model described in Eq. 2.19 is fitted to the measured spectrum of plasma density fluctuation.

2.1.2.3 Spectral form in the inertial and viscous subrange

Tracers which are affected by turbulence but do not identically reproduce the velocity fluctuations of the turbulent flow show a different spectral behavior in the viscous subrange. Fig. 2.2 shows the spectral models of *Heisenberg* [1948] (blue) and *Driscoll and Kennedy* [1985] (orange) as a function of wavenumber k for the inertial and viscous subranges. The *Heisenberg*-model has a $-5/3$ slope in the inertial subrange and the energy decrease with k^{-7} in the

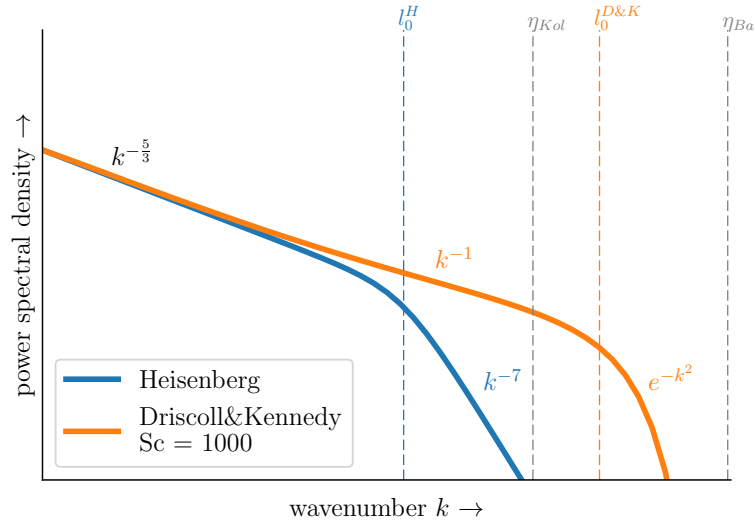


Figure 2.2: Theoretical spectral shapes by *Heisenberg* [1948] in blue and by *Driscoll and Kennedy* [1985] in orange. Also labeled are the slopes of the regimes of the turbulent spectra. The dashed lines mark the inner scale l_0^H (blue) for the Heisenberg-model and the inner scale $l_0^{D\&K}$ for the *Driscoll&Kennedy*-model according to *Lübken* [1993]. Additionally the Kolmogoroff microscale η_{Kol} and the Batchelor scale η_{Ba} are shown by grey dashed lines.

viscous subrange and is independent of Sc . The scale at which the transition between inertial and viscous subrange occurs is the inner scale l_0^H . The inner scale for the *Heisenberg*-model is indicated by the blue dashed line in Fig. 2.2. The inner scale for the *D&K*-model is indicated by the orange dashed line in Fig. 2.2. For Schmidt numbers larger than one the viscous subrange of the *Driscoll&Kennedy*-model extends to smaller scales. This behavior is linked to the tracer's diffusivity D which is inversely proportional to the Schmidt number. In the following section diffusion in a dusty plasma will be described briefly.

2.2 Diffusion in a dusty plasma

Diffusion is change of concentration with time and is described by Fick's second law

$$\frac{\partial N_j}{\partial t} = D_j \Delta \cdot N_j, \quad (2.21)$$

where the index j refer to each plasma constituent, N_j is the constituents concentration, t is time, D_j is the diffusion coefficient and Δ is the Laplace operator. Assuming chemical equilibrium each constituent obeys a continuity equation which is

$$\frac{\partial N_j}{\partial t} + \nabla \cdot \vec{\Gamma}_j = 0, \quad (2.22)$$

where $\vec{\Gamma}_j$ is the diffusion flux of the j -th specie. From kinetic theory using the Einstein relation one can write the diffusion coefficient as

$$D_j = \mu_j k_B T, \quad (2.23)$$

where k_B is the Boltzmann constant, T is the temperature and μ_j is the mobility which is for charged particles in a gas phase

$$\mu_j = \frac{q_j}{m_j \nu_j}, \quad (2.24)$$

with the j -th particle charge q_j , its mass m and the momentum transfer collision frequency ν_j . In a plasma the charged constituents are also coupled by Coulomb forces. Charge separation give rise to an electric field which in the diffusion case is also known as ambipolar electric field \vec{E} . The ambipolar diffusion flux is than

$$\vec{\Gamma}_j = -D_j \nabla N_j + N_j \mu_j \vec{E} \quad (2.25)$$

which can be defined for charged particles other than electrons as [Rapp, 2003]

$$\Gamma_{j \neq e} = -D_j \nabla N_j + \frac{q_j N_j}{q_e N_e} D_j \nabla N_e. \quad (2.26)$$

2.2.1 Diffusion coefficient for charged aerosol particles

In this section the model for the diffusivity of cluster ions and aerosols by *Cho et al.* [1992] will shortly be recapitulated. Aerosols in the MLT region can for example be ice particles, cluster ions or meteor smoke particles. One assumption made is that all particles are in thermal equilibrium which is not necessarily the case for aerosols under sunlit conditions [e.g., *Eidhammer and Havnes*, 2001; *Espy and Jutt*, 2002; *Asmus et al.*, 2013, 2014]. However, this temperature difference is negligibly small for the derivation of diffusion and its application in the course of this work. The diffusion coefficient is given by

$$D_d = \frac{3k_B T}{16\mu_{dn} N_n \Omega_{dn}}, \quad (2.27)$$

where T is the temperature, $\mu_{dn} = \frac{m_d m_n}{m_d + m_n}$ is the reduced mass with the dust particles mass m_d , the mean molecular mass m_n , N_n is the neutral air density and Ω_{dn} is the collision integral.

For particles with $r_d \gtrsim 0.52$ nm the diffusivity D_d can be precisely described by a hard sphere model [Cho et al., 1992]

$$D_d^H = \frac{3}{8N_n(r_d + r_n)^2} \sqrt{\frac{k_B T}{2\pi\mu_{dn}}}, \quad (2.28)$$

where $r_n = 1.8 \times 10^{-10}$ m is the effective neutral molecule radius (N_2) [Cho et al., 1992] and r_d is the MSP radius and $m_d = \frac{4\pi}{3} \rho r_d^3$ its mass. For particles with $r_d \lesssim 0.52$ nm a polarization model has been shown to be applicable [Cho et al., 1992, and references therein] since for the smallest particle induced polarization fields in neutral molecules become more relevant. The diffusion coefficient is then defined as

$$D_d^P = \frac{9.06 \cdot 10^5 k_B T}{N_n |Z_d| e} \sqrt{\frac{\epsilon_0}{\pi \alpha \mu_{dn}}}, \quad (2.29)$$

where Z_d is the dust's charge number, e is the elementary charge, ϵ_0 is the vacuum permittivity and the neutral atom polarizability $\alpha = 1.76 \times 10^{-18} \text{ m}^{-3}$ [Cho et al., 1992].

The transition between polarization and hard sphere interaction can be derived by equating the collision integrals for both models and solving for the particle transition radius yields [Cho et al., 1992]

$$r_{tr} = 4.55 \times 10^{-4} \left(\frac{2\alpha Z_d^2 e^2}{\epsilon_0 k_B T} \right)^{\frac{1}{4}} - r_n, \quad (2.30)$$

where $\alpha = 1.76 \times 10^{-18} \text{ m}^{-3}$ is the neutral atom polarizability, Z_a is the particles charge number, e is the elementary charge, ϵ_0 is the vacuum permittivity, k_B is Boltzmanns constant and T is the temperature (assumed to be in thermal equilibrium with the ambient gas). Note that Eq. 2.30 only depends on temperature. A typical value for the winter mesosphere for single charged particles at $T = 200 \text{ K}$ is $r_{tr} = 0.45 \text{ nm}$.

2.2.2 Diffusion coefficient for electrons in the presence of heavy charged particles

In this section a general expression of electron diffusivity will be briefly described by following *Hill* [1978]; *Rapp* [2003]. First of all we will introduce a variable to describe the ratio between charged dust and electron density $\Lambda = |Z_d|N_d/N_e$. Using quasi neutrality one can introduce a new variable which represents the density of all plasma constituents other than electrons.

$$N_{\dagger} = N_i + N_d. \quad (2.31)$$

Furthermore, fluctuations n_j of the density around a mean N_{j0} are introduced such that $N_j = N_{j0} + n_j$, where the index j stands for the j -th plasma component. One can now write the continuity equations for the perturbations n_e and n_{\dagger} by using Eq. 2.22 and 2.26 as [*Rapp*, 2003]

$$\frac{\partial n_e}{\partial t} = \frac{D_i - D_d}{2} \nabla^2 n_{\dagger} + \left[D_i + \frac{D_i + D_d}{2} (1 + 2\Lambda) \right] \nabla^2 n_e \quad (2.32)$$

$$\frac{\partial n_{\dagger}}{\partial t} = \frac{D_i + D_d}{2} \nabla^2 n_{\dagger} + \left[D_i + \frac{D_i - D_d}{2} (1 + 2\Lambda) \right] \nabla^2 n_e. \quad (2.33)$$

Here the diffusion coefficient for ions D_i is analog to Eq. 2.27 defined as

$$D_i = \frac{3k_B T}{16\mu_{in} N_n \Omega_{in}}, \quad (2.34)$$

and the diffusion coefficient for charged dust particles is given by Eq. 2.28 and 2.29. The linear equation system formed by Eq. 2.32 and 2.33 has two eigenmodes. The corresponding eigenvalues are given in *Rapp* [2003]

$$D_{1/2}^0 = \frac{1}{2} [D_i + (D_i + D_d)(1 + \Lambda)] \pm \frac{1}{2} \sqrt{D_i^2 (\Lambda + 2)^2 + 2D_i D_d (\Lambda - 2)(\Lambda + 1) + D_d^2 (\Lambda + 1)^2} \quad (2.35)$$

$D_{1/2}$ describe the influence of the Coulomb interaction between electrons and ions (1) and electrons and charged dust (2). The interaction between electrons and ions is more or less independent of the dust size but increases when the number density of dust particles exceeds the electron concentration. The influence of charged dust onto the diffusion of electrons is mainly depending on the particles size. However, if there are more charged dust particles than electrons the diffusion of electrons is further decreased [*Rapp*, 2003].

In the case that there are much less electrons than charged particles the electron diffusivity is dominated by the charged particles and one may write [*Lübken et al.*, 1998]

$$D_e \approx D_d, \text{ for } Z_d \cdot N_d \gg N_e, \quad (2.36)$$

where D_e and D_d are the electron and charged dust diffusivity, respectively, Z_d is the dust charge number, N_d its number density and N_e is the electron number density. Under this assumption the electron diffusivity is dependent on the dusts size. This is explicitly the case for Eq. 2.28 and implicitly for Eq. 2.29 via μ_{dn} .

Chapter 3

Measurement techniques and instruments

This chapter includes the description of rocket borne instruments used in the course of this work to obtain geophysical parameters. These are electron density N_e , neutral density N_n and their fluctuations $\Delta N_{e/n}$, neutral temperature T , charged dust density and atomic oxygen density. The instruments and corresponding measured parameters are given in Tab. 3.1.

Table 3.1:

Instrument	Parameter
3.1 CONE	$N_e, N_n, T, \Delta N_e, \Delta N_n$
3.2 PIP	N_i
3.3 PD	N_d
3.4 Wave prop.	N_e
3.5 FIPEX	N_O
3.6 Photometer	N_O

3.1 Combined sensor for neutrals and electrons – CONE

The CONE (COmbined sensor for Neutrals and Electrons) instrument is primarily an ionization gauge [Lübken, 1987]. A unique feature of this instrument is its ability to measure neutral gas and electron density with the same instrument as it consists of a ionization gauge and an electrostatic probe. It has an open design using spherical grids to be less affected by aerodynamics and to lower the instruments time constant. Giebeler *et al.* [1993] give a full technical description of the instrument. Fig. 3.1 shows a schematic and a picture of the instrument. The outermost grid (5) is held at a positive bias with respect to the payload potential and represent an electrostatic probe to measure electrons. The positive bias repels positive ions and at the same time attracts electrons. The current onto the grid is hence proportional to the local electron density. The current onto the probe also depends on the ratio between the probes' surface and the reference probe, which in the case of sounding rocket measurements is the payload body (conducting surface). Since electrons have a much larger mobility than ions they cause a much higher electron current which has to be balanced by an equally sized positive ion return current. In order to obtain undamped electron currents the area of the reference (payload body) has to be significantly larger. Szuszczewicz [1972] found that the

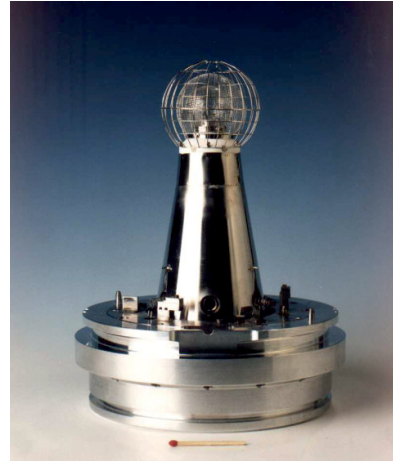
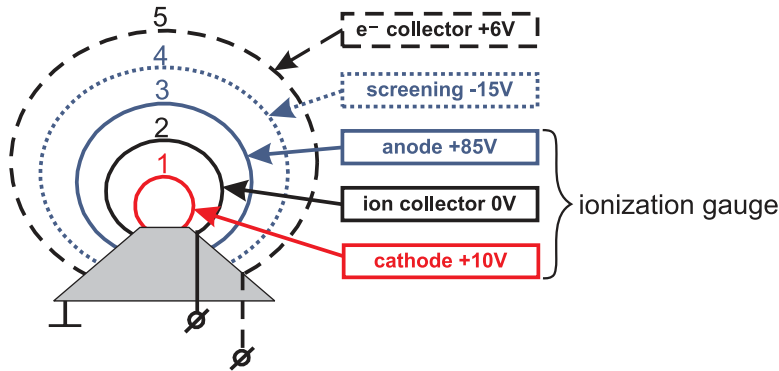


Figure 3.1: Left: Schematic of the sensor head. Right: Photo of the sensor without electronics [Strelnikov, 2006].

reference probe area has to be larger by a factor of at least 1×10^4 with respect to the electron probe to have non disturbed measurements.

The screening grid (4) is biased to -15 V and repels electrons. The sensor inner grids (1,2,3) form an ionization gauge whereas the middle grid (2) is the ion collector. The electron emission current at cathode (1) is stabilized. Thus, the collected current on grid 2 is proportional to the amount of ionized molecules and hence the number density of neutral molecules. By means of the open design the time constant of electron and neutral density measurement mainly depends on the electronics yielding less than 1 ms . The sensitive electrometers enable resolving fluctuations down to 0.01% .

3.2 Positive ion probe – PIP



Figure 3.2: Positive ion probe as flown by the Technische Universität Graz. Same version was flown on WADIS-2 sounding rocket.

Positive ion density can be measured for instance by the positive ion probe (PIP). PIP is a fixed negatively biased spherical probe surrounded by a grid held at payload potential [Folkestad, 1970]. Electrons are repelled and positive ions are attracted by the negative biased probe. Hence the current to the biased inner probe is a true ion current. The probe is designed to attract all ions up to masses of approximately 100 amu [Friedrich, 2016]. These

probes are typically placed on booms allowing to have an aerodynamically favorable position on both up- and downleg. However, typically there is a strong spin modulation of the signal due to angle of attack larger than zero. This results in one side of the payload being in a more ram- and one in a more wake-like position. Fig. 3.2 shows a version of the probe as flown on the WADIS-2 sounding rocket in pre-flight position. The golden colored sphere inside the grid is the probe held at -6 V with respect to the payload potential. The measured current to the central probe can be converted to a relative ion density. The procedure is described in Sec. 4.3.

3.3 IAP particle detector – PD

The Faraday cup principle was first applied to a rocket borne instrument by *Havnes et al.* [1996] and was extensively used to measure charged aerosols in the high latitude lower ionosphere [e.g., *Gelinas et al.*, 1998; *Lynch*, 2005; *Rapp et al.*, 2011]. The instrument principal design is as follows. A metal cup with an electrode inside is shielded by two oppositely biased grids against the ambient thermal plasma. Hence only particles with sufficient kinetic energy can penetrate into the cup and hit the electrode. The obtained current is proportional to the number of particles. Rocket borne Faraday cups are known to have an aerodynamical cut-off below 80 km, prohibiting small particles to be detected [*Hedin et al.*, 2007; *Strelnikova et al.*, 2009; *Plane et al.*, 2014]. *Rapp et al.* [2009] combined the classical Faraday cup principle with a xenon flash lamp to actively photoionize aerosols and collect the resulting photo electrons. This technique enables the detection of initially neutral aerosol particles.

The IAP particle detector is a relatively small instrument. Its cup has a radius of $r_{cup} = 30$ mm and the electrode is at the bottom 38 mm inside the cup. The inter grid distance is 15 mm, whereas the grid has a transmissivity of 74 %. Fig. 3.3 shows a picture of the whole instrument which includes the cup (upside) and its electronic box (downside). The PD has two grids G_1 , G_2 and the electrode. The upper grid, G_1 was biased at $+6$ V and the lower grid G_2 at -6 V with respect to the payload skin to shield the electrode from thermal ions and electrons. This was the configuration for the WADIS-2 flight. The electrode as well as the two grids were connected to electrometers. The current measured by the electrode is therefore proportional to the number density of the heavy charged aerosols (MSP or NLC particles). The derivation of charged particle density is described in detail in Sec. 4.1. The time constant of the sensor electrode was estimated by a laboratory experiment. Therefore the sensor was placed in a vacuum chamber into an afterglow plasma [*Hannemann et al.*, 2003]. The shielding grids of the instrument were used to produce sudden increase of plasma density inside the cup. This was achieved by switching on and off the grids bias of ± 6 V. The response in the electrodes electrometer was instantly with full magnitude which lead us to the conclusion that the sensors time constant τ_s is less than the sampling rate of the electronics ($\tau_s < 1$ ms).

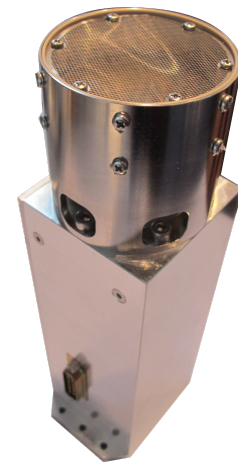


Figure 3.3: Picture of the IAP particle detector (PD) with cup and electronic box.

3.4 Wave propagation experiment

In this section the wave propagation experiment also known as Faraday rotation on sounding rockets will be described briefly. For a more detailed description the reader is referred to e.g., *Mechtly et al.* [1967]; *Bennett et al.* [1972]. This technique is hitherto the only one providing in situ absolute electron densities [*Mechtly*, 1974]. This experiment is operated by the Technical University of Graz (TUG), Austria. The data from numerous sounding rocket flights have been used for a semi-empirical lower ionosphere model [*Friedrich and Torkar*, 2001]. The experiment consists of a transmitter on ground and receiving antennas on board the rocket. It uses the fact that the complex refractive index $n = \mu + i\kappa$ of an electromagnetic wave depends on electron density and the ability of magnetized plasma to change the polarization plane of a polarized electromagnetic wave which is called Faraday rotation. Its rate dF per unit length ds is given by [*Bennett et al.*, 1972]

$$dF = \frac{\omega}{2c}(\mu_o - \mu_x)ds, \quad (3.1)$$

where ω is the frequency of the emitted electromagnetic wave, c is the speed of light, μ_o and μ_x are the real part of the refractive index of the ordinary, extraordinary part of the wave, respectively. The refractive index in the MLT region is mainly determined by free electron density and can be derived via the *Appleton-Hartree* formula or in a more generalized form by *Sen and Wyller* [1960]. Therefore electron density can be obtained from the change of polarization of a transmitted electromagnetic wave. The derivation of absolute electron densities is not part of this work and therefore for a detailed description of the experiment the reader is referred to e.g., *Mechtly et al.* [1967]; *Bennett et al.* [1972]; *Friedrich* [2016].

Fig. 3.4 shows the antennas (yellow tape measure strips) and also PIP on board a sounding rocket. Those antennas are unfolded until they are perpendicular to the payload's hull.

During launch the antennas are bound to the payload by a wire which is cut during motor separation. The flexible antennas unfold themselves into their initial position which is perpendicular to the payload body. The altitude resolution is determined by the spin rate of the rocket. For typical rates of ~ 4 Hz this yields an absolute electron density value for each kilometer in vertical direction. To get a reasonable altitude coverage one usually uses multiple frequencies. Typical frequencies used are 1.3 MHz, 2.2 MHz, 3.883 MHz and 7.835 MHz [*Friedrich*, 2016].

3.5 Flux Φ Probe Experiment – FIPEX

A relatively new concept developed and operated by the Institute of Space Systems (IRS) of the University of Stuttgart, Germany is based on solid electrolyte sensors which was first

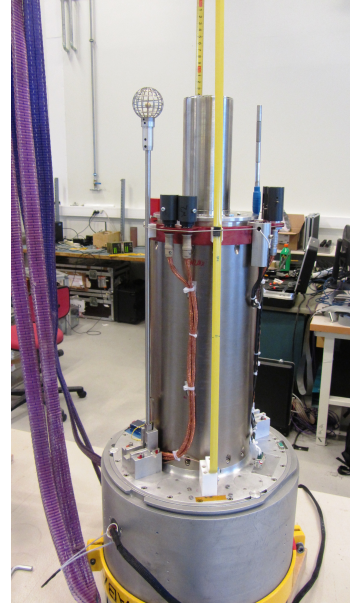


Figure 3.4: Picture of the aft instrument section of the WADIS-2 payload (see Sec. 5.1 for details on WADIS). The yellow tape measure strips are the antennas for the wave propagation experiment. They are unfolded to the side after motor separation.

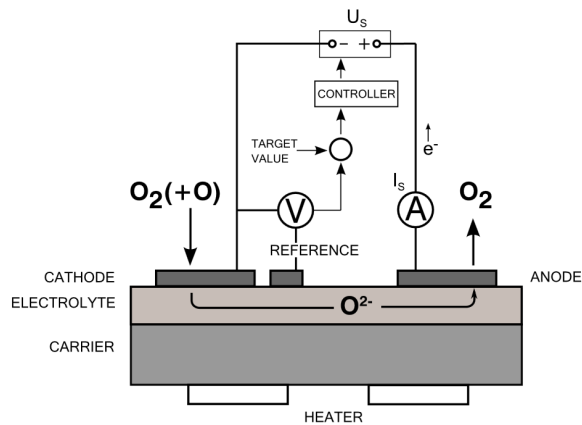


Figure 3.5: Measurement principle of the FIPEX sensor [Eberhart *et al.*, 2015].

flown on a sounding rocket in 2013 [Eberhart *et al.*, 2015; Strelnikov *et al.*, 2017]. Golden electrodes are used for the sensor being sensitive to atomic oxygen. Platinum is for molecular oxygen. A reference electrode with a low bias voltage is placed between anode and cathode. This electrostatic potential is used to pump oxygen ions through the solid electrolyte. Material of the ceramic electrolyte is Yttria Stabilized Zirconia (YSZ). In order to optimize the conductivity of the ceramic the sensors have to be heated to 500 °C. The flowing current between anode and cathode is proportional to oxygen density. The sensors are calibrated in the laboratory to obtain absolute densities. The current is sampled with 100 Hz which gives an altitude resolution of approximately ~10 m.

3.6 Airglow Photometer

Rocket-borne airglow photometry provides a direct in situ measurement of the chemical composition in the mesosphere and lower thermosphere (MLT). The Department of Meteorology at Stockholm University, Sweden (MISU) has a long history of airglow measurements from sounding rockets and provides one airglow photometer for the WADIS payload. During nighttime the photometer measures the emission from the O_2 ($b^1 \Sigma_g^+ - X^3 \Sigma_g^-$) atmospheric band at 762 nm. This emission is related to the photolysis of O_2 and a retrieval of O is possible [Gumbel, 1997; Hedin *et al.*, 2009]. Thus this photometer provide altitude profiles of O. The neutral air density (and temperature) measurements by the CONE instruments and accurate information about payload attitude are very important for the analysis of this data. This photometer concept is based on experience from the Swedish PHOCUS sounding rocket campaign in 2011.

Chapter 4

Data reduction and analysis techniques

In this chapter first of all the data handling is presented. This includes the conversion of measured quantities like currents into densities and a procedure to estimate the detectable sizes of MSP, the derivation of electron density residuals and its spectral analysis.

4.1 Charge densities

The measured current onto the sensor of the PD is proportional to the charge density of particles hitting the sensor electrode. This holds if one assumes that secondary charging is negligible. This assumption is reasonable, for our case ($v < 1000 \text{ m s}^{-1}$, Faraday-cup type sensor) since

- direct electron secondary emission does not play a role at velocities of $\leq 1000 \text{ m s}^{-1}$, it needs velocities larger than $10\,000 \text{ m s}^{-1}$ for this effect to matter [Dalmann *et al.*, 1977; Havnes and Næsheim, 2007]. Dalmann *et al.* [1977] studied micrometer sized particles with kinetic energies in range of 50 GeV to 4 TeV. In contrast to that kinetic energies of MSPs hitting the rocket at 1000 m s^{-1} are thought to be in the range of 5 eV to 10 keV.
- charging effect for lower velocities ($\leq 1000 \text{ m s}^{-1}$) is thought to have its origin from particles impacting on a surface at a relatively large incident angle relative to the surface zenith and carry away electrons or ions leaving the surface. Whatsoever, since the majority of particle trajectories are perpendicular to the surface this effect is negligible for the sensor electrode.
- Currents due to photo emission can be neglected during night time in the absence of Sun light

Analysis of particle trajectories reveals that the kinetic energy decreases rapidly, when the particles enter shock front of the rocket (reduced by $\sim 60\%$, see Sec. 4.1.1). This is also an indication that the majority of particles will have low kinetic energy (~ 10 to 100 eV) in comparison to micro meteoroids when they hit a surface of an instrument, thereby supporting the arguments above.

The measured current is reduced by particles hitting the grids' in front of the sensor electrode. The fraction of lost particles is determined by the grids' transparency. The initial current I_0 is reduced by a factor of $1 - \sigma$ where σ is the cross section of the grid. For the grid

of the PD $\sigma = 0.26$. A schematic of the detector is shown in Fig. 4.1. Since there are two grids

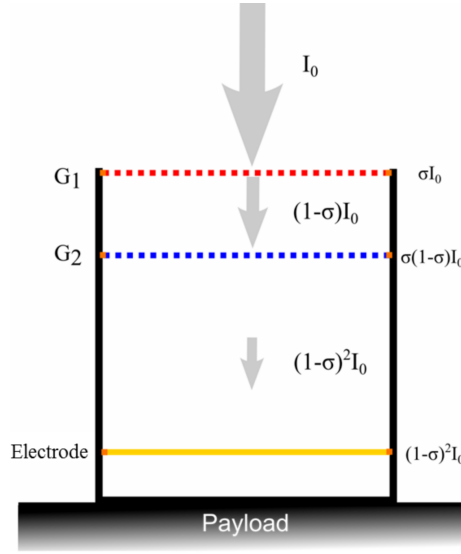


Figure 4.1: Schematics of the PD (i.e. Faraday cup). The two grids G_1 and G_2 are biased -3 V and $+3$ V, respectively. The grey arrows indicate the flow of the dust particles. The dust current into the cup is reduced by collisions with grids which depends on the grids' cross section σ . $1 - \sigma$ represents the grids transmissivity and I_0 is the undisturbed dust particle current. Reprinted from *Asmus et al.* [2013].

the current reaching the sensor electrode is

$$I_s = (1 - \sigma)^2 I_0. \quad (4.1)$$

The initial current can be estimated by the simple relation [*Havnes et al.*, 1996]

$$I_0 = eAv_R Z_d N_d \quad (4.2)$$

where e is the elementary charge, A is the sensor inlet area, v_R is the rocket velocity, $Z_d N_d$ is the charge density, the product of the number of charges Z_d and particle density N_d . Inserting Eq. 4.2 into Eq. 4.1 and solving for $Z_d N_d$ yields

$$Z_d N_d = \frac{I_s}{eAv_R(1 - \sigma)^2}. \quad (4.3)$$

One assumption here is that in the reference frame of the rocket all particles move with the rocket velocity. This is not necessarily the case since particles are slowed down by the shock front of the rocket and light particles may be significantly slower. However, this uncertainty is in the order of a factor of 2 which is in the range of the estimated uncertainty of this measurement. The role of aerodynamics and electrostatic fields will be elucidated in the subsequent section.

4.1.1 Combined aerodynamic and electrostatic simulations

The velocity of a sounding rocket with an apogee in the lower thermosphere is typically in the order of 1000 m s^{-1} . Since this is a multiple of the speed of sound ($\sim 300 \text{ m s}^{-1}$) there are significant aerodynamical effects accompanying rockets flight. A major phenomenon known

from all objects moving with super sonic velocity is the so-called shock-front. It is a region of enhanced gas density, temperature and changing velocity components developing in front of the moving object. All measurements which depend on the air flow onto the instrument are affected by the shock front. The measured parameters are distorted by the shock front and hence represent disturbed atmospheric values. However, one can for example derive the distortions introduced by the super sonic flow. The today most reliable way to estimate disturbances in density, temperature and velocity fields around the payload is to simulate them by means of the Direct Simulation Monte Carlo (DSMC) method developed by *Bird* [1994]. In the sounding rocket community this technique has widely been used in the past, e.g., by *Gumbel* [2001]; *Rapp and Lübken* [2001]; *Hedin et al.* [2007]; *Plane et al.* [2015]; *Staszak* [2015]. The shape of the shock front depends on the rockets' speed and payload configuration as well as ambient air density. For this reason it is necessary to perform a dedicated aerodynamic simulation for every sounding rocket flight. This becomes even more important for instruments which are not in a prominent upstream position. The PDs on board the WADIS-2 payload were placed next to the CONE electronic cylinder. The PDs were much likely influenced by CONEs shock front. For a detailed description of the WADIS project and the payload configuration see Sec. 5.1. To get an insight into the altitude dependence of aerodynamic effects, the simulations were done for four height levels, i.e., for 70, 75, 82, and 95 km. For all simulations the frame of reference is the payload.

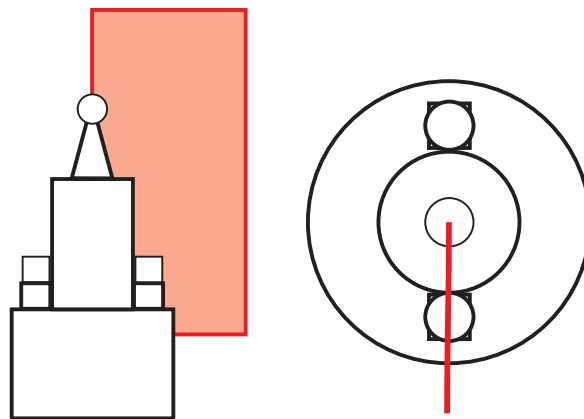


Figure 4.2: Forward part of the payload and the section used in the 2d DSMC marked in red.

Since the forward deck is symmetric, half of a cross section was used for the simulation to reduce computational time and complexity. In this 2d simulation the geometry of the shielding grids cannot be resolved. Thus, in the first step the cups interior is represented as a solid body which is a good approximation in terms of flow disturbances in front of the instrument. The background parameters such as temperature and velocity for the simulations were taken from WADIS-2 measurements and are given in Tab. 4.1. The simulations were performed by means of the free available software *DS2V* [Bird, 2017]. The simulated velocity fields of the neutral gas around the forward deck at 70 and 95 km are shown in Fig. 4.3. The shock front is well defined by the change of the streamline direction. The flow field at lower heights reveals rapid changes as the gas approaches payload which well defines the edge of the shock front. Close to the rocket body there are even regions of reverse flow directions. At 95 km the situation looks different, here the flow almost follows the shape of the payload. The shock front is not visible here since it is less well defined and rather coarse.

Besides the aerodynamical effects, the detection of charged aerosols is influenced by applied electric fields for example by shielding grids. Those electric fields can be easily simulated by

Table 4.1: Boundary conditions for the 2d DSMC.

height [km]	temperature [K]	density [m^{-3}]	velocity $_x$ [m s^{-1}]
70	216.14	$1.24 \cdot 10^{21}$	1030.0
75	220.34	$5.69 \cdot 10^{20}$	971.0
82	233.24	$2.04 \cdot 10^{20}$	909.4
95	168.95	$2.40 \cdot 10^{19}$	777.5

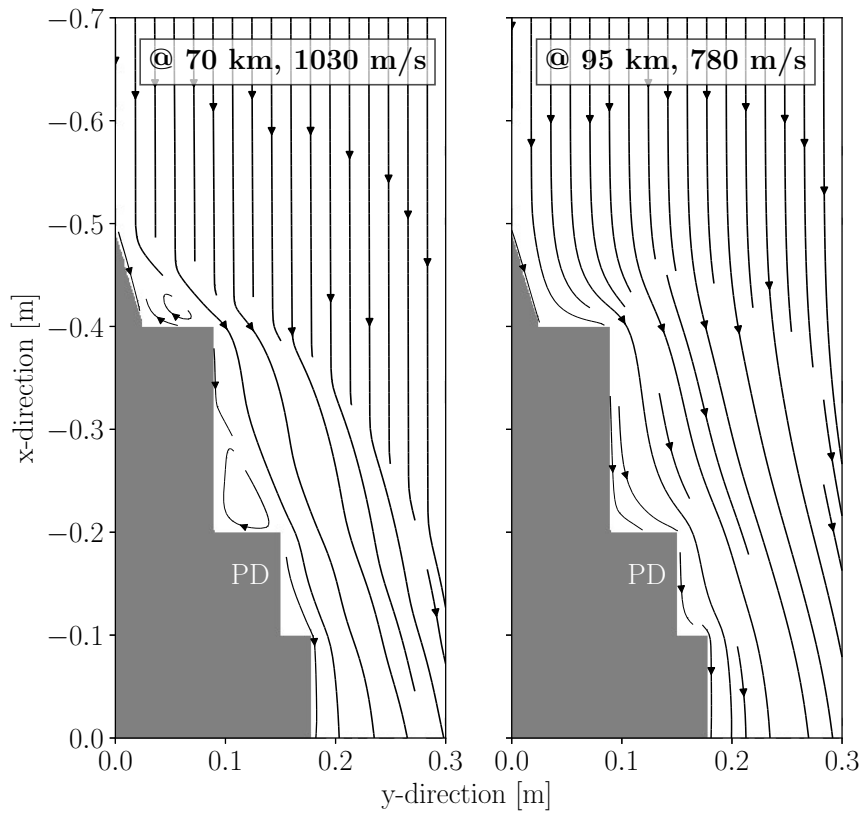


Figure 4.3: Velocity field shown by black streamlines at 70 km (left) and at 95 km (right). Grey shaded area is the payload structure inclusive instruments.

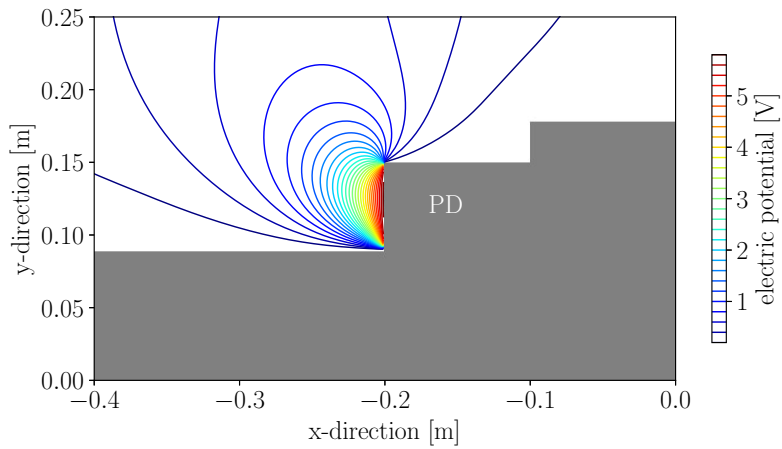


Figure 4.4: Distribution of electro static potential induced from the PDs outer grids. Grey shaded area is the payload structure inclusive instruments.

e.g. proprietary software like SIMION[®]. The electric field distribution in front of the Faraday cup is shown in Fig. 4.4. Here the outer grid is represented as a single electrode biased at 6 V with respect to the payload body. The isolines show regions of equal potential and the magnitude is given by the color. The potential rapidly decreases to < 2 V in ~ 5 cm distance from the grids. Furthermore, the shape of the potential distribution is not symmetric due to the potential of the payload body. The electric field has lensing effects for charged particles, also known from e.g., ion optics and therefore influence the particles' trajectory. To assess the size range of charged particles reaching the outer grid i.e. the particle detector entrance, trajectories of particles through the distorted flow field have to be derived considering also the electrostatic forces. This can be achieved using SIMION[®] in non vacuum conditions. The DSMC results were used as background fields (temperature, density, and velocity). Results of the simulations using two groups of particles are shown in Fig. 4.5 where part of the rocket body is shown in black, the colored background show the density of ambient air, and simulated trajectories of the dust particles are shown as white, and red lines for masses of 1000 and 60 000 amu, respectively. As also can be inferred from the neutral gas flow field shown in Fig. 4.3 the shock front is also present in the density. Since the density of the atmosphere and the velocity of the rocket increases with decreasing altitude, the shock front is more pronounced at lower heights. However, the main shock front is formed in front of the CONE instrument from -0.5 to -0.4 m in the x-direction. Here ram factors, i.e. the ratio of undisturbed ambient density to those inside the measurement volume, are between 3.5 and 6 near the payload body. It is apparent that at 70 km height (Fig. 4.5c) aerodynamics prohibits dust measurements even for huge particles with masses of 60 000 amu, which corresponds to radii of approximately 2.3 nm. As they are more affected by aerodynamics, light particles are blown away from the PD by the shock front.

To estimate a probability for particles to reach the PD's outer grid i.e. its entrance, a number of trajectories were simulated to achieve appropriate statistics. The derived probabilities for 4000 randomly injected particles above the PD are summarized in Fig. 4.6. The y-axis shows

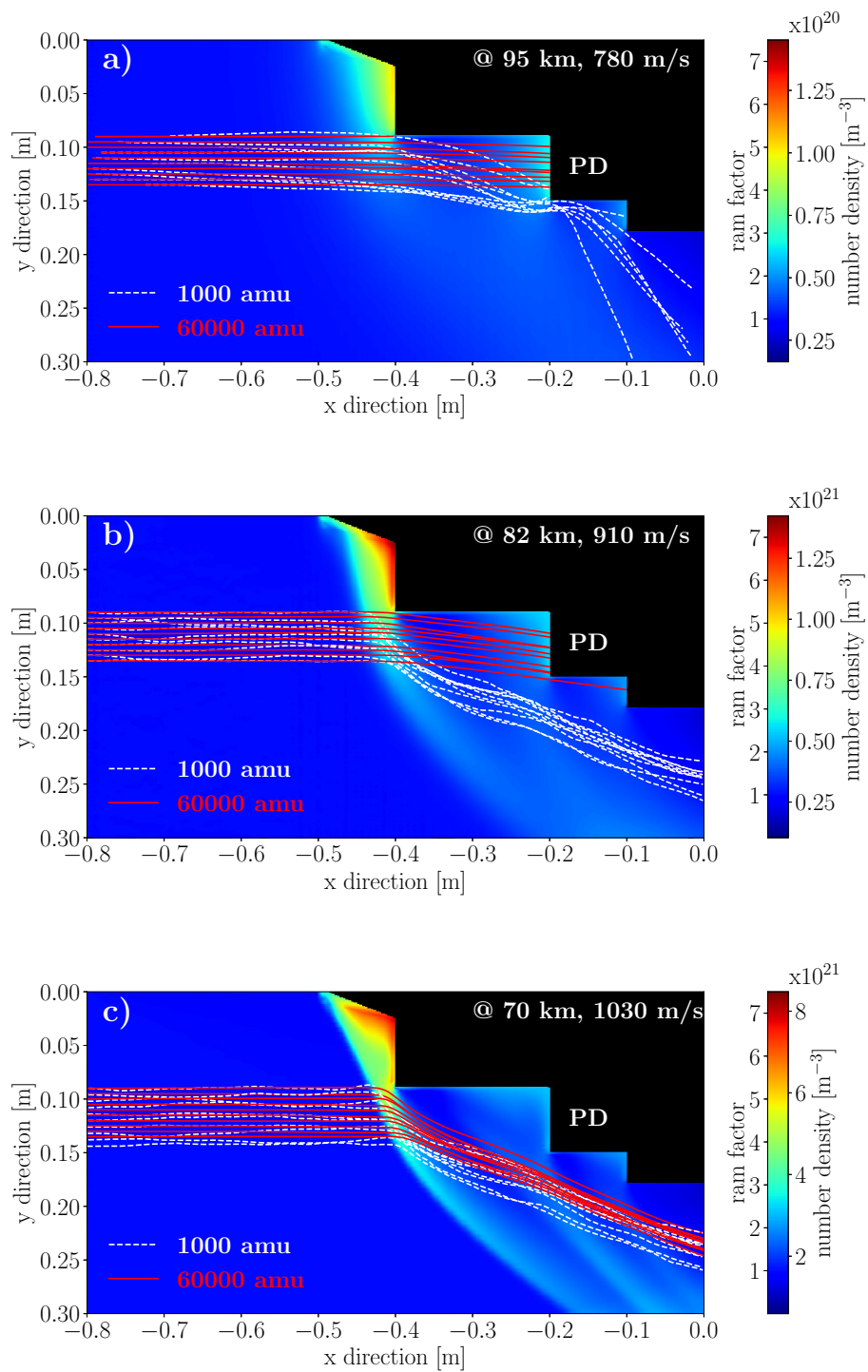


Figure 4.5: Results of combined DSMC and electrostatic simulations for WADIS-2 payload. Black area shows the one half of the WADIS-2 front deck. X-axis is along the rockets roll axis. The position of the particle detector is indicated with PD. Density field derived using the DSMC for 95, 82, and 70 km. White and red lines correspond to trajectories of particles with 1000 and 60 000 amu, respectively. Reprinted from *Asmus et al.* [2017]

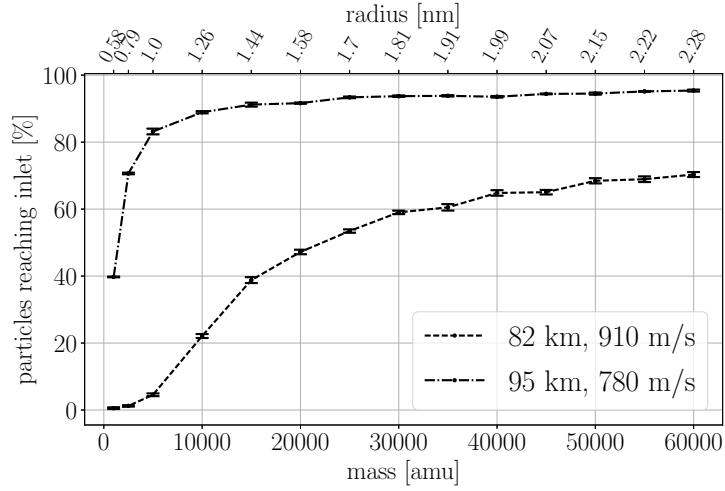


Figure 4.6: Simulated probabilities that particles reach the PD as a function of mass (radius) for 82 and 95 km. The velocity and background atmosphere correspond to WADIS-2 flight conditions. The statistics was derived from 4000 particle trajectories. Reprinted from *Asmus et al.* [2017].

probability in % that an MSP reaches the PD. The dashed and the dotted lines show results for 82 and 95 km height, respectively. Here only the cases of 95 and 82 km are shown since the probabilities for the altitudes 70 and 75 km are zero in the mass range from 0 to 60 000 amu. The probability was calculated by dividing the number of particles hitting the inlet surface of the PD by the total number of simulated particles $p = \frac{n_{hit}}{N}$.

Besides the influence by collisions with neutral molecules, charged particles are also influenced by attracting or repelling electrostatic forces. The origin of those electrostatic fields are the biased electrodes and the shielding grids of the particle detector. Thus, the applied bias will also limit the minimum detectable particle mass of the PD. This mass can be estimated, assuming the particles are moving with the rockets velocity by using the energy conversation law

$$\frac{m}{2}v_R^2 = eU, \quad (4.4)$$

where U is the grids' bias of 6 V, e is elementary charge, v_R the rocket (particle) velocity, and m is the mass of a particle. Assuming spherical particles with a mass density $\rho = \frac{3m}{4\pi r^3} = 2 \text{ g cm}^{-3}$ one can derive the critical radius r_{cE} at which particles can overcome the electrostatic barrier is given

$$r_{cE} = \sqrt[3]{\frac{3eU}{2\pi\rho v_R^2}}, \quad (4.5)$$

Typical kinetic energies of MSP are shown in Fig. 4.7 as a function of particle radius and velocity. The red line indicates the 6 eV kinetic energy level which is necessary for a particle to overcome the PD shielding grid. For a typical rocket velocity of 1000 m s^{-1} this yields a minimum detectable particle radius of $\sim 0.6 \text{ nm}$. This plot also shows that variation of the minimum detectable radius due to electrostatic fields is $\pm 0.1 \text{ nm}$ for velocity changes around the typical value of $1000 \mp 200 \text{ m s}^{-1}$. With a velocity profile from the WADIS-2 flight an altitude dependent minimal critical radius due to electrostatic barrier was determined. In Fig. 4.8 this is compared with the critical radius of particles able to reach the outer grid due

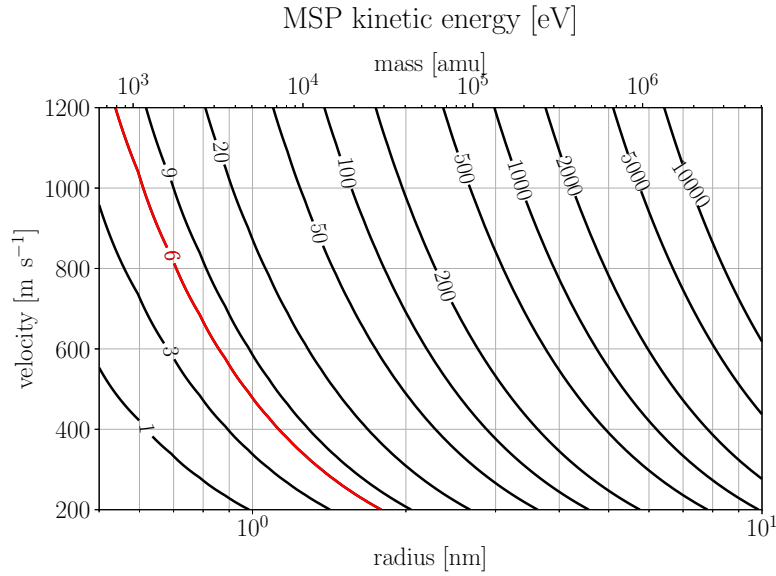


Figure 4.7: Kinetic energy of MSP ($\rho=2 \text{ g cm}^{-3}$) as a function of radius and velocity.

to aerodynamics only. The detection limit between 65 to 115 km due to electrostatics is in the range of 0.6 to 1 nm. As the rockets' total velocity decreases with altitude, the kinetic energy of particles decreases and hence the radius of the smallest detectable particle enlarges. The aerodynamical filtering on the other hand sets in below 95 km. However the aerodynamic effect dominates below ~ 84 km. Below that altitude the critical radius increases exponentially indicating the dependence on neutral air density. At 70 km particles with radii smaller than 4.5 nm can not be detected. The majority of MSP radii ($>99\%$) are thought to smaller than this limit and thus no particle detection by means of the PD is possible below 70 km. This has also been found by earlier studies [e.g., *Hedin et al.*, 2007; *Strelnikova et al.*, 2009]. By means of the additional information about the minimum detection limits of the PD we are able to make conclusions of the present charged particle sizes during WADIS-2. Above 92 km there were less than 10 cm^{-3} of charged particles larger than ~ 0.7 nm. Below 75 km there were less than 10 cm^{-3} of charged particles smaller than 2.5 nm. 10 cm^{-3} is the approximate lower resolution of the PD. Note, that the final critical radius is determined by the combination of aerodynamic and electrostatic effects. Hence, the critical radii shown in Fig. 4.8 represent minimum values of undetectable particle radii. Moreover, the detection efficiency of the particle detector is given by the probability of particles hitting the inner sensor electrode.

Obviously, one has to resolve the instruments mechanical design in the simulations to also account for filtering by the shielding grids. For this purpose we used 3d simulations to resolve the detector in detail. For the background density, temperature and density fields a method by *Scanlon et al.* [2010] was used, which allows the use of large computer clusters. It was shown to be appropriate for highly resolved sounding rocket instrumentation by *Staszak et al.* [2015]. Despite using a large number of CPUs the simulation still needs a relatively long time to converge (days to weeks) in contrast to the single core 2d simulations. To reduce computational time one particular height was chosen to derive the sensors detection efficiency which is the height of maximum measured dust density i.e. 82 km. There are several reasons to chose this altitude. First of all, the maximum dust density was measured

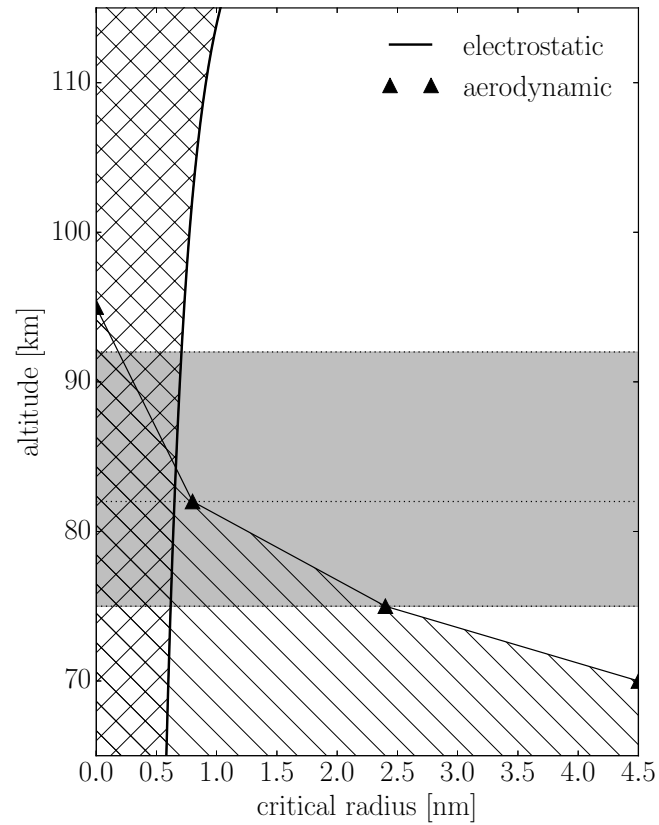


Figure 4.8: Minimal detectable critical radius of particles shown for electrostatic filtering (solid black line) and by pure aerodynamics (black triangles). Hatched areas show regions where particle detection is not possible. Grey shaded areas indicate the altitude range where charged particles were measured and the dotted black line at 82 km marks the measured density maximum. Reprinted from *Asmus et al.* [2017].

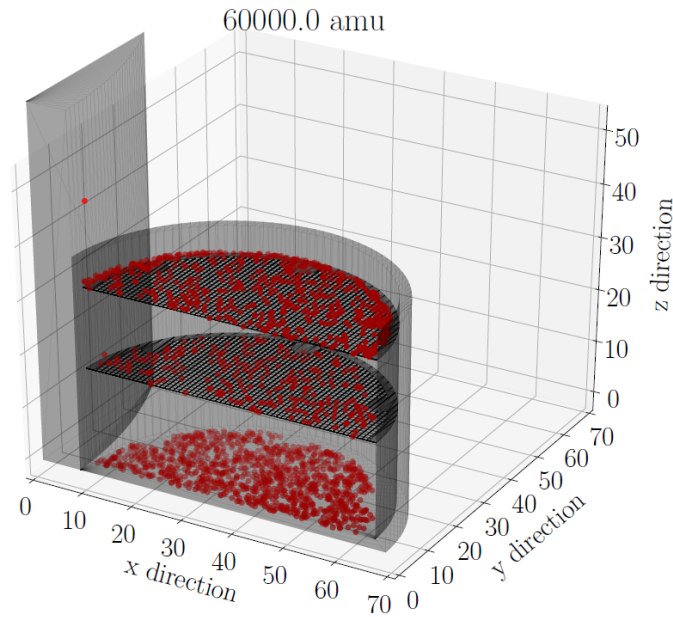


Figure 4.9: 3d simulation volume with a part of the CONE electronic cylinder (at $x = 0$) and half of the PD cup. The red dots mark the endpoints i.e. impact of particle trajectories with a mass of 60000 amu.

here and a better understanding of the detector's size depending detection properties at this height will be crucial for the estimation of a size distribution described in Sec. 5.8. Secondly, from Fig. 4.8 we learned that here the effect of electrostatics and aerodynamics should be nearly the same.

To further decrease the computational effort, we simulated a half of the particle cup plus 20 mm in front of the cup and a part of the CONE electronics cylinder. The initial conditions for the 3d simulation were taken from the 2d case. This includes the temperature, density and velocity at the boundary above the PD cup. The orientation of the simulation is shown in Fig. 4.9, where gray shaded faces indicate instrument or payload surfaces. Additionally, the impact points of 60000 amu particles are indicated by red dots. It is apparent that almost half of the particles are hitting the inner electrode whereas the other half hit the inner or outer grids. This simulation was performed using both, aerodynamics and electrostatics. Again, 4000 particle trajectories were simulated to keep the statistical error below 1% and the probability is calculated counting particles hitting the inner electrode and divide the sum by all particles simulated. The result is shown in Fig. 4.10 as the dashed dotted gray line. The theoretical transparency of the grids of 55% is well reproduced by the simulations. Surprisingly, the detection seems to be more or less independent of the aerodynamics since the detection efficiency after increasing suddenly between 1.26 and 1.44 nm stays more or less constant. It appears, that the threshold is due to the electrostatic barrier, which is increased in contrast to the simplified case given in Eq. 4.5 since the velocity of MSPs is decreased after the main shock front. The simulation volume in the 3d case includes only the cup of the instrument and a limited space in front of the cup which are both behind the shock-front. Some particles are already being blown away by the main shock front and are not able to reach this volume. Therefore the final detection efficiency of the PD in the WADIS-2 payload configuration is given by the combination of the 2d and 3d simulation. The result is shown

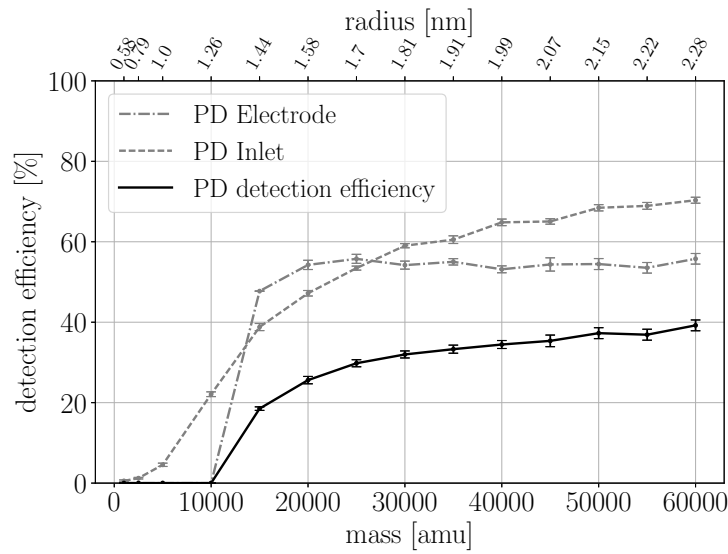


Figure 4.10: PD detection efficiency (black solid line) at 82 km as a function of particle mass (radius) by means of the product of the probabilities of particles reaching the inlet (dashed gray line) of the PD and its electrode (dashed dotted gray line). Reprinted from *Asmus et al.* [2017].

as black solid line in Fig. 4.10. And indeed, the critical radius at 82 km is determined by the electrostatic barrier given by the shielding grids.

Summarizing the combined simulations of electrostatics and aerodynamics we conclude that below ~ 80 km the influence by aerodynamical effects rapidly increases and prevents even huge (~ 4.5 nm) particles from being detected at altitudes around 70 km. If one would neglect the aerodynamic effect the critical radius would only slightly increase below 100 km as seen in Fig. 4.8. However, since aerodynamic effects play an important role at altitudes below 80 km it is indispensable to perform aerodynamic simulations to obtain detection efficiencies. The procedure of the simulation was as follows. First of all the flow onto a larger part of the rocket payload was simulated. Due to computational limitations this was performed in 2d. In a second step the results of the 2d simulation were used to feed a detailed 3d simulation of the sensor and its nearest surrounding. The third step was an electrostatic simulation for the larger and the smaller volume in non vacuum conditions using the resulting fields of the aerodynamic simulations. In the last step particle trajectories were calculated for both large and small volume. In the large volume case the particles reaching the detector entrance were counted whereas in the detailed simulation we count the particles reaching the sensor surface inside the cup. From this the detection efficiencies for both cases were calculated and combined by multiplication to a final detection efficiency of the Instrument for the WADIS-2 flight.

- The 2d simulation gives:
 1. Radii of particles which are transported out of the PD inflow.
 2. Neutral Density and Temperature. Particle velocity in front of the PD.

- From the 3d simulation we obtain the sizes of particles which are stopped by the shielding grids and which reach the sensor electrode.
- The combination of both gives the detection efficiency of the instrument in the WADIS-2 configuration.

The particles detectable sizes by the particle detector are now well defined for 82 km. That is, the PD current at 82 km is produced by MSP of $r \gtrsim 1.44$ nm. The DMSC method derives macroscopic parameters for each grid cell by averaging over the particles in the cell, e.g., calculating the mean temperature of the particles in one grid cell. The derivation of mean values is reasonable after the simulation converges, i.e., the number of simulated particles converges. Hence, the uncertainty of the macroscopic parameter is determined on the one hand by the number of particles in the grid cells and on the other hand by the statistical uncertainty of the number of particles to be simulated. It was shown qualitatively that simulation results are in agreement with wind tunnel test by *Gumbel* [2001]. We therefore assume that the uncertainty of background fields derived from DSMC are negligible for the calculation of critical radii.

4.2 Electron density from an electrostatic probe - CONE

The CONE instrument is at the same time both an ionization gauge and an electrostatic probe. The outer grid of the sensor seen in Fig. 3.1 is positively biased to 6 V or 3 V *Giebler et al.* [1993]; *Asmus et al.* [2017]. The current to the probe depends on the thermal speed of electrons

$$v_{th} = \sqrt{\frac{8k_B T_e}{\pi m_e}}, \quad (4.6)$$

where the electron temperature T_e is assumed to be equal the ambient temperature. Thus, the current due to the thermal speed of electrons is

$$I_0 = \frac{1}{4} e N_e v_{th} \quad (4.7)$$

Neglecting the inhomogeneities of the electric field produced by the gridded structure of the probe one may write the current to a spherical probe as [*Friedrich et al.*, 1997; *Friedrich*, 2016]

$$I = I_0 A \left(1 + \frac{eV}{k_B T_e} \right) \quad (4.8)$$

where $A = 4\pi r^2(1 - Tr)$ is the grids surface, $r = 3.2$ cm its radius and $Tr \approx 0.9$ the grids transparency. The potential of the probe seen by an electron is the sum of probe potential plus the payload potential

$$V = V_{probe} + V_{payload}. \quad (4.9)$$

Solving Eq. 4.7 for N_e using Eq. 4.8 and 4.9 yields

$$N_e = \frac{4I}{eA v_{th} \left(1 + \frac{eV}{k_B T_e} \right)}. \quad (4.10)$$

Eq. 4.10 can be used to estimate the electron density. This can be done assuming a payload potential. However, since the payload potential is usually neither known nor constant over

time/height the result still represents a relative electron density. An absolute profile can be obtained by normalizing the relative density to the electron density of the Faraday rotation experiment since it is the technique that provides absolute electron densities. To account for the change in the payloads potential with altitude one might use an altitude dependent polynomial function to obtain an altitude dependent normalization factor.

4.3 Positive ion densities from a gridded sphere - PIP

As mentioned in Sec. 3.1 the positive ion probe (PIP) is an electrostatic probe consisting of a spherical probe surrounded by a grid. The inner probe is biased to -6 V attracting positive ions and repelling electrons whereas the surrounding grid is at payload potential. The ion flux to the probe is on the one hand determined by the rocket's velocity v_R which is on the order of 1000 m s^{-1} . On the other hand also the thermal velocity v_{th} of the ions is important since it is on the order of $\sim 300\text{ m s}^{-1}$ and therefor comparable to v_R . The ion thermal velocity is defined as

$$v_{th} = \sqrt{\frac{8k_B T}{\pi m_i}}, \quad (4.11)$$

where T is the ions temperature and m_i its mass. The current due to the ions' thermal motion is then

$$I_0 = \alpha \pi r_0^2 e N_i v_{th}, \quad (4.12)$$

where α is the grid's effective cross section (1 for a solid sphere; $1 - tr$ for grids, where tr is the grids transparency), r_0 is the inner probe radius, e is the elementary charge and N_i is the positive ion number density. Finally the total current to the probe is defined as [Folkestad, 1970]

$$I = I_0 \left(\frac{1}{2} \exp(-t^2) + \sqrt{\pi} \left(\frac{t}{2} + \frac{1}{4t} \right) \text{erf}(t) \right). \quad (4.13)$$

Here $t = \frac{2v_R}{v_{th}\sqrt{\pi}}$ and $\text{erf}(t) = \frac{2}{\sqrt{\pi}} \int_0^t \exp(-p^2) dp$ is the so-called error function. The current to the probe also depends on the payload potential. The larger the probes surface is the less prominent is this influence since the return current of positive ions is larger. Positive ions entering the inside of the probe are attracted to the inner sensor. Only ions with masses below a certain limit can reach the sensor. Ions with larger masses will be dragged out of the probe due to inertia. The critical mass can be estimated following Folkestad [1970] by

$$m_{crit} = \frac{2V_b e}{v_R^2 \left(\left(\frac{r_1}{r_0} \right)^2 - 1 \right)}, \quad (4.14)$$

where V_b is the applied bias to the inner probe with respect to the payload potential and r_1 is the radius of the outer grid. For a bias $V_b = 6\text{ V}$, a rocket velocity $v_R = 1000\text{ m s}^{-1}$ and a ratio $\frac{r_1}{r_0} = 1.25$ this will lead to a critical mass of $\sim 2000\text{ u}$.

This design was and is still used in a variety of versions [e.g., Blix et al., 1990; Asmus et al., 2015a]. With a sufficient spatial resolution and sensitivity this instrument can also be used to obtain small scale fluctuations [Blix et al., 1990; Strelnikov et al., 2006].

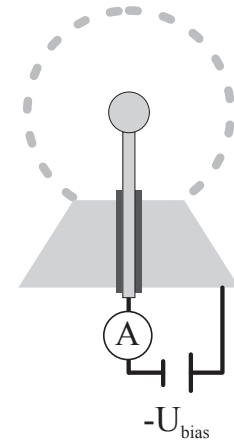


Figure 4.11: Schematic of a gridded sphere positive ion probe.

4.4 Neutral and plasma fluctuations

Density fluctuations are represented by the variation of the density around its mean value, the residuals. The residuals are generally defined as [Lübken, 1993; Strelnikov, 2006]

$$r_{\vartheta}(t) = \frac{N_{\vartheta}(t) - \langle N_{\vartheta}(t) \rangle}{\langle N_{\vartheta}(t) \rangle} = \frac{\delta N_{\vartheta}(t)}{\langle N_{\vartheta}(t) \rangle}, \quad (4.15)$$

where $N(t)$ is the density, $\langle N(t) \rangle$ is the reference density derived as a e.g., running mean, $\langle \dots \rangle$ denotes spatial averaging, and subscript ϑ refer to neutrals, electrons, positive ions and charged aerosols, respectively. If density is direct proportional to a measured current $I_{\vartheta}(t)$ the residuals can also be written as

$$r_{\vartheta}(t) = \frac{\delta I_{\vartheta}(t)}{\langle I_{\vartheta}(t) \rangle} = \frac{\delta N_{\vartheta}(t)}{\langle N_{\vartheta}(t) \rangle} \quad (4.16)$$

An example of the derivation of residuals is illustrated by Fig. 4.12. In the left panel measured electron density $N_e(t)$ and its mean profile $\langle N_e(t) \rangle$ are shown. By means of Eq. 4.16 and multiplied by 100 one obtain residuals in percent which are shown in the right panel of Fig. 4.12.

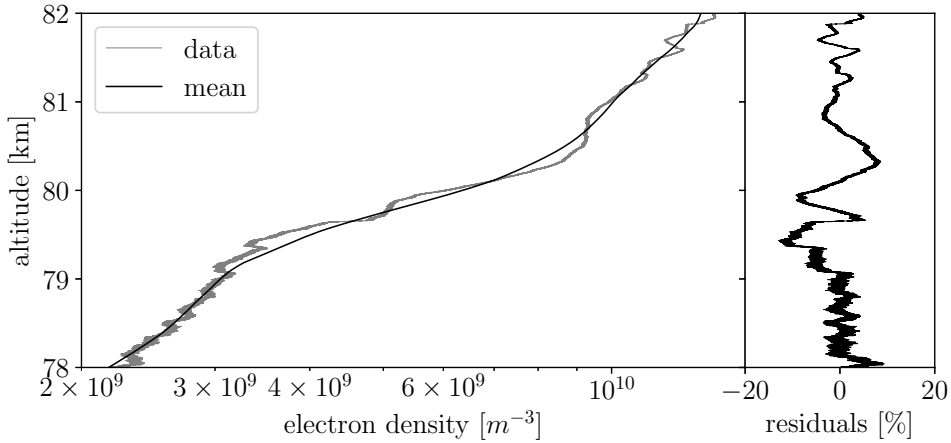


Figure 4.12: Left panel: Measured electron density in grey and the mean/trend profile in black. Right panel: Fluctuations around the mean profile.

By transforming the residuals into frequency space by means of e.g., a Fourier or Wavelet transform one can get an insight of the energy at a certain frequency or scale [Strelnikov *et al.*, 2003]. If the fluctuations in the tracer are caused by turbulent processes the energy spectrum has a distinct shape and can be described by a theoretical model. By fitting a theoretical spectra to the measured data one can obtain physical parameters. This method is described in more detail in Sec. 2.1.2. In the next section the connection between particle size and Schmidt number will be described.

4.5 Particle radii from Schmidt number

Lübken *et al.* [1998] found that in Summer under the condition that there are more charged particles than electrons (see relation 2.36) the Schmidt number is related to the particle radius

by

$$Sc = 6.5 \cdot r_d^2 \quad (r_d \text{ in nm}). \quad (4.17)$$

However, this is valid only for particles much larger than the mean neutral molecule radius, as will be shown later in this section. As mentioned in Sec. 2.2.1 there are two expressions of diffusivity depending on the dominating interaction model. For particles smaller than the transition radius r_{tr} , which is approximately 0.45 nm, the polarization interaction is dominating. In this case the diffusion coefficient is indirectly related to the particle radius via the particle mass which (assuming spherical particles) is given by

$$m_d = \frac{4\pi}{3} \rho r_d^3 \quad (4.18)$$

with the MSP radius r_d and its mass density $\rho = 2 \text{ g cm}^{-3}$. Using Eq. 2.7, 4.18, 2.29 and 2.36 one can derive the particle radius as a function of Sc .

$$Sc = \frac{\nu}{D_d^P} = \frac{\nu N_n Z e}{9.05 \cdot 10^5 k_B T} \sqrt{\frac{\pi \alpha \mu_n}{\epsilon_0 \left(\frac{m_n}{m_d} + 1 \right)}} \quad (4.19)$$

Using Eq. 4.18 and solving for r_d gives

$$r_d^P = \sqrt[3]{\frac{3}{4\pi \rho} \frac{m_n}{\left(\frac{\nu}{Sc C_P} \right)^2 - 1}}, \quad (4.20)$$

where $C_P = \frac{9.06 \times 10^5 k_B T}{N_n |Z_d| e} \sqrt{\frac{\epsilon_0}{\pi \alpha m_n}}$. The diffusivity D_d can be described by a hard sphere model for particles with $r_d > r_{tr}$ [Cho *et al.*, 1992]. Using the definition of D_d given in Eq. 2.28 and inserting into Eq. 2.36 yields

$$Sc = \underbrace{\frac{8}{3} \nu N_n \sqrt{\frac{2\pi m_n}{k_B T}}}_{C_H} \underbrace{\frac{(r_d + r_n)^2}{\sqrt{1 + \frac{m_n}{m_d}}}}_{r_{eff}^2} = C_H \cdot r_{eff}^2, \quad (4.21)$$

where ν is the kinematic viscosity of air and r_{eff} is an effective radius. C_H can be calculated using in situ measurements of density and temperature, r_{eff} can be derived for each Schmidt number by means of

$$r_{eff} = \sqrt{\frac{Sc}{C_H}}. \quad (4.22)$$

The coefficient C_H can be compared to the constant found by Lübken *et al.* [1998]. For WADIS-2 conditions C_H is around $8 \pm 0.1 \text{ nm}^{-2}$ between 80 and 85 km. This is slightly higher than the value of 6.5 found for Summer conditions by Lübken *et al.* [1998] which can be attributed to the different densities and temperatures. The mean charged particle radius, however, is the parameter which we are interested in. For $r_{eff} \gtrsim 0.4 \text{ nm}$ the functional behavior between r_d and r_{eff} can be approximated by a linear equation of the form $r_d = a \cdot r_{eff} + b$. This can clearly be seen in Fig. 4.13. The functional behavior of $r_{eff}^2 = \frac{(r_d + r_n)^2}{\sqrt{1 + m_n/m_d}}$ is shown by the blue and linear fit by the green line. It is apparent that for small particles the ratio m_d/m_n becomes important. The fitted linear equation for r_d^H in nm reads

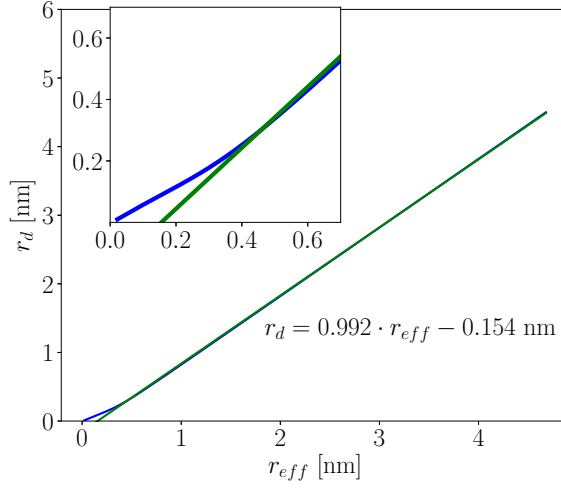


Figure 4.13: The blue line shows the MSP radius r_d as a function of the effective radius r_{eff} . A linear fit is show by the green line. Reprinted from *Asmus et al.* [2017].

$$r_d^H = 0.992 \cdot r_{eff} - 0.154. \quad (4.23)$$

The mean charged particle radius at a given height is derived as

$$\begin{aligned} r_d^H &= 0.992 \cdot \sqrt{\frac{Sc}{C_H}} - 0.154 \\ &= 0.992 \cdot \sqrt{\frac{3Sc}{8vN_n} \sqrt{\frac{k_B T}{2\pi m_n}}} - 0.154. \end{aligned} \quad (4.24)$$

We now can calculate the mean charged particle radius for both, polarization and hard sphere interaction. In addition, since we use derived Schmidt numbers for the radii derivation it is necessary to calculate the transition Schmidt number to define whether to use the polarization or the hard sphere interaction model. The transition can be found using Eq. 2.7 and 2.30,

$$Sc_{tr} = \frac{v}{D_d^{H,P}(r_{tr})}. \quad (4.25)$$

Since $D_d^H(r_{tr}) = D_d^P(r_{tr})$, the definition of the diffusion coefficient for either polarization or hard sphere interaction can be used. Where D_d^H is the diffusion coefficient of dust in the hard sphere regime and D_d^P in the polarization regime. Sc_{tr} is the corresponding Schmidt number to the particle radius at which transition between polarization and hard sphere interaction occurs.

Chapter 5

Results 1: WADIS-2 campaign

In this chapter the results of thesis are presented. In situ measurements of neutral and charged components conducted during the second campaign of WADIS ("WAVE propagation and DISSIPATION in the middle atmosphere: Energy budget and distribution of trace constituents") project were analyzed. Some of the results were also published in *Asmus et al.* [2017] and are reproduced here in a revised form. The chapter is structured as follows. First a brief overview of the project is given which then is followed by the presentation of background conditions into which the sounding rocket was launched. Subsequently, instrumental properties of the particle detector on the WADIS-2 payload are analyzed. In what follows, the derivation of charged particle density is presented and afterwards small scale structures in neutrals and electrons are studied. From those density fluctuations particle parameter are deduced. A charged particle size distribution is derived by combining results of charged particle, electron, positive ion and neutral measurements in the following section. In addition, by means of the measured parameters the reason for absence of coherent radar echoes at $\lambda_{\frac{1}{2}} = 2.8$ m is investigated.

5.1 The WADIS project

WADIS stands for "Wave propagation and dissipation in the middle atmosphere: Energy budget and distribution of trace constituents" and was a research project initiated by the Leibniz Institute of Atmospheric Physics (IAP) in partnership with the Institute of Space Systems (IRS) in Stuttgart. Additional contributions came from Austria, Sweden, the USA, and Norway. In the course of this project two instrumented sounding rockets were launched in two field campaigns conducted at the Andøya Space Center (ASC) in northern Norway (69°N, 16°E). The first campaign was conducted during PMSE conditions in June 2013 whereas the second campaign took place in a pure winter state of the atmosphere in March 2015 [Asmus et al., 2017]. The project was devoted to the investigation of gravity waves (GW), their dissipation and their influence on trace constituents. Both rockets were identically equipped and the arrangement of instruments is shown in Fig. 5.1. Two CONE instruments (for a detailed description see in Sec. 3.1) were on board the payload, one on the forward and one on the aft deck enabled the measurement of highly resolved densities of electrons and neutrals on up- and downleg. On the forward deck there were also two particle detectors from IAP (detailed description see Sec. 3.3), catalytic sensors (FIPEX, forward and aft deck) by IRS and photometers by the Department of Meteorology of the Stockholm University (MISU), Sweden. Positive ion probe (PIP), the wave propagation experiment both operated by the Graz University of Technology (TUG), Austria, and an electrostatic probe operated

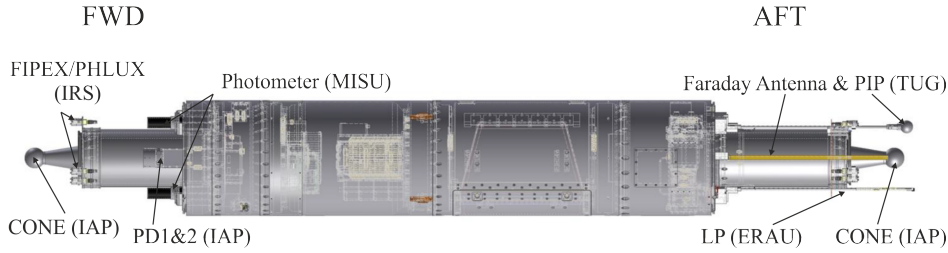


Figure 5.1: WADIS payload configuration with its instruments (corresponding institution abbreviation): CONE (IAP), FIPEX (IRS), two PDs (IAP) and two photometer (MISU) on the forward deck (FWD) and a wave propagation experiment/ Faraday antennas, PIP (both TUG), LP (ERAU) and CONE on the aft deck (AFT).

Table 5.1: WADIS payload instrumentation.

Instrument	Parameter	Institution
CONE (NP)	absolute neutral density	IAP
CONE (EP)	relative electron density	IAP
PD	charged aerosols	IAP
FIPEX	atomic oxygen density	IRS
PIP	relative positive ion density	TUG
Wave prop.	absolute electron density	TUG
Photometers	atomic oxygen density	MISU
EP	relative electron density, neutral aerosols	ERAU

by Embry-Riddle Aeronautical University, USA was mounted on the rear deck of the payload conducting measurements during up- and downleg. Tab. 5.1 gives a short overview of the instruments, the measured parameter and the corresponding responsible institution. Detailed information on the project, as well as the WADIS-1 flight can be found in *Strelnikov et al. [2017]*.

In the frame of the present work the focus lies on the WADIS-2 in situ measurements. The instrumented sounding rocket was launched on March 5th, 2015 at 01:44 UT. The trajectory of the flight is shown in Fig. 5.2. The orange shaded faces show the Norwegian coast, the black solid line is the relevant altitude range of measurement. Red dots indicate altitudes and corresponding time of flight. The green dotted line indicate the zenith over the launch pad.

Subsequently, the results of measurements of mesospheric dusty plasma during WADIS-2 sounding rocket campaign are presented. First, a brief overview of the atmospheric state during the campaign is given including measured parameters by remote sensing techniques.

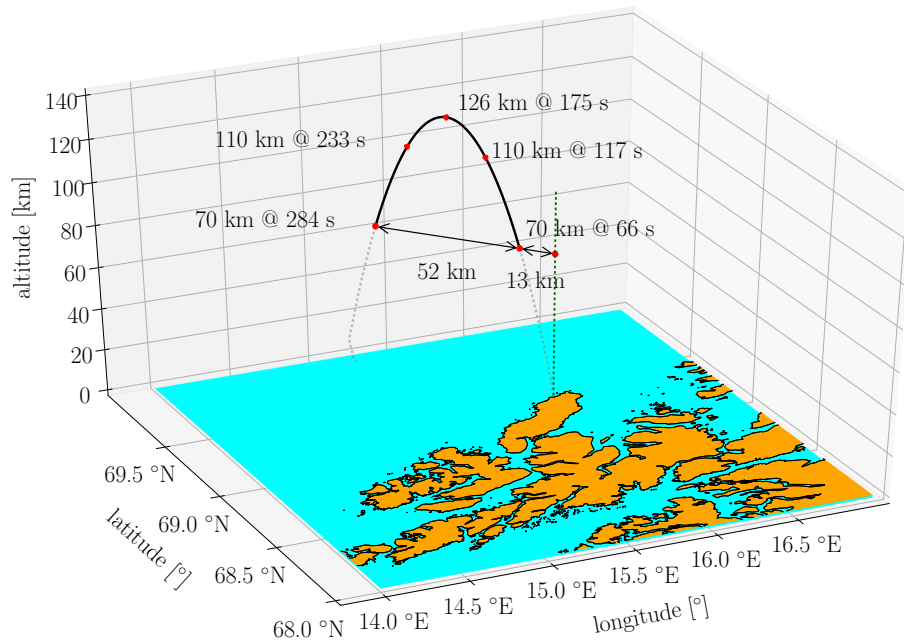


Figure 5.2: Trajectory of WADIS-2 launched on March the 5th 2015 at 01:44 UT from the Andøya Space Center.

5.2 Atmospheric background

Since the main aim of WADIS was the investigation of gravity waves good launch conditions required the observation of GW. The ionospheric state was of minor importance. To classify the conditions in the mesosphere and lower ionosphere during the launch it is necessary to look at parameters such as geomagnetic activity, winds and temperatures. The geomagnetic activity is characterized by e.g., the K -index, high energetic proton or X-ray flux. The planetary or K_p -index is derived using the standardized K -index. It is divided into integers in the range of 0.. 9 and obtained from different magnetic observatories and gives qualitative impression of the geomagnetic activity [Bartels *et al.*, 1939]. For the time around the WADIS-2 launch the K -index for the Tromsø region is shown in Fig. 5.3. The values found for K -index are in the range from 0 to 5. The launch itself was at a time of a low K -index of 1 shortly after a higher geomagnetic activity. Having said this, one does not expect high ionization rates due to particle precipitation in the D-region.

In addition to the in situ measurements, there were also remote sensing instruments involved into the campaign. Active instruments like radars need fluctuations in the radio refractive index which in the mesosphere is solely determined by the electron density [Skolnik, 2008]. For VHF radars mesospheric echoes due to coherent scattering processes at the Bragg scale which is half the radar wavelength. Next to the launch facilities on Andøya there is the Middle Atmosphere Alomar Radar System (MAARSY) which monitors the MLT region for coherent radar echoes ($\lambda_{\frac{1}{2}} = 2.8$ m) [Latteck *et al.*, 2012]. A quantitative information about the strength of radar backscatter is the signal-to-noise ratio (SNR). Fig. 5.4 shows the SNR as a function of time and altitude for March the 5th 2015, the day of launch of the instrumented sounding rocket. Around the launch time of the rocket (01:44 UT) there were no radar echoes. From statistics of polar mesospheric winter echoes (PMWE) it is known

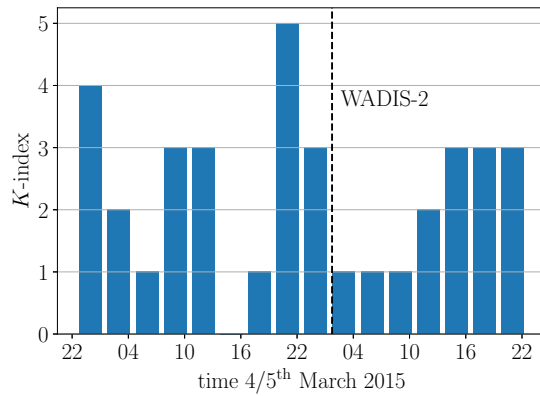


Figure 5.3: K -index for Tromsø for 4th and 5th March 2015 [Hall, 2017]. The dashed line marks the time of the rocket launch.

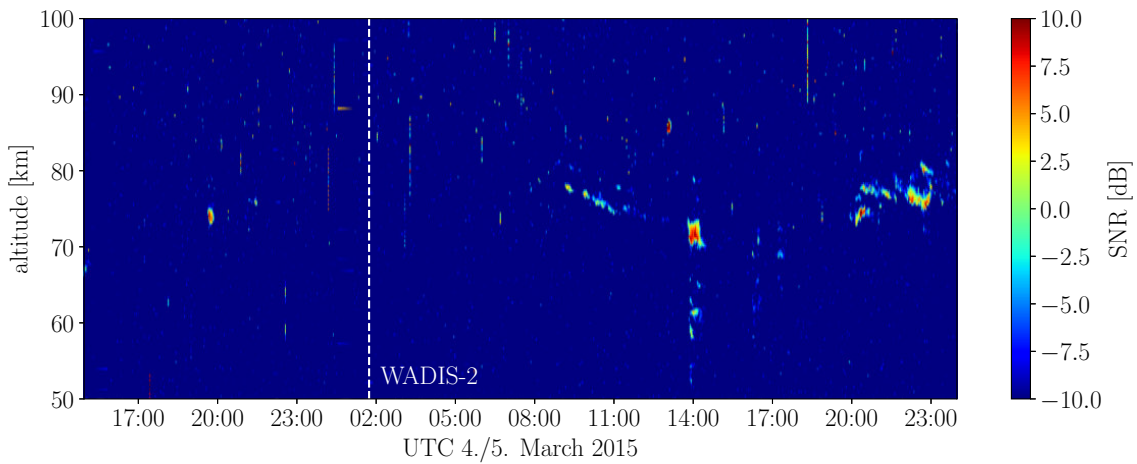


Figure 5.4: MAARSY signal-to-noise ratio as a function of time and altitude from 4th to 5th of March, 2015. The vertical white line indicates the launch of the instrumented sounding rocket. Data courtesy of Ralph Latteck.

that their occurrence has a maximum around noon and is minimal during night time as they are highly depending on electron density [Zeller *et al.*, 2006; Latteck and Strelnikova, 2015].

Besides the observation by radar there were also measurements by the ALOMAR RMR-lidar and the mobile IAP-Fe-lidar which yield e.g., temperature profiles [von Zahn *et al.*, 2000; Lautenbach and Höffner, 2004].

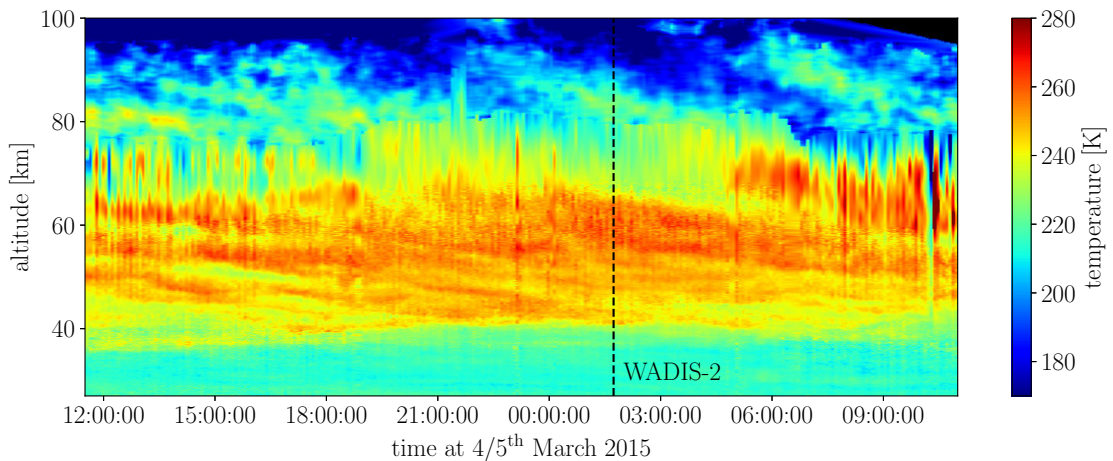


Figure 5.5: Temporal evolution of temperature above ALOMAR as a function of altitude in the night from 4th to 5th of March, 2015, deduced from RMR and Fe lidar data. The black dashed line marks the launch of the instrumented sounding rocket. Data courtesy of Gerd Baumgarten and Josef Höffner.

Combining RMR- and Fe-lidar measurements temperature profiles of the whole middle atmosphere. The temporal evolution of temperature around the WADIS-2 launch is shown in Fig. 5.5. There are tidal features especially between 60 km to 100 km indicated by wavelike structures with a horizontal wavelength of approximately 8 h and amplitudes up to ~ 30 K. High temperatures coincide with high OH-emission which is due to a temperature dependent emission rate [e.g., Wallace and Wallace, 1962].

Notably, the rocket passed MLT region while a temperature enhancement was present between 80 and 90 km. This can be seen in a smoothed temperature profile from the lidars shown in Fig. 5.6. Those temperature enhancements are thought to originate from nonlinear interactions between gravity and tidal waves [e.g., Meriwether and Gerrard, 2004]. Moreover, the so-called mesospheric inversion layers (MIL) were also found to coincide with regions of enhanced neutral turbulence [Szewczyk *et al.*, 2013]. Notably, there is a relative obvious signature of the 8 h tide in the lidar temperature measurements. Hence, the temperature enhancement in this case is caused by tide rather than by the creation by turbulence as proposed by Szewczyk *et al.* [2013].

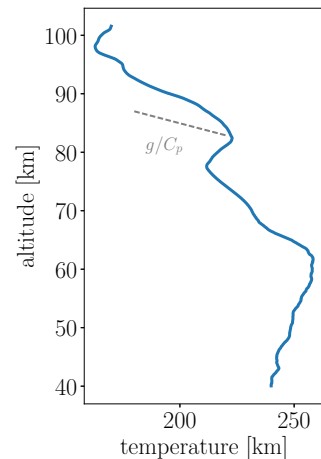


Figure 5.6: Smoothed lidar temperature March 05.03.2015 01:44: UT. The dashed grey line represents the adiabatic lapse rate $\Gamma = \frac{g}{C_p}$. Data courtesy of Gerd Baumgarten and Josef Höffner.

Finally, we look at the mesospheric winds obtained by the ALOMAR sodium-Weber lidar which is a resonance fluorescence lidar and is described in detail by She *et al.* [2002]; Arnold and She [2003]. The results of Na-lidar wind measurements are displayed in Fig. 5.7 also show tidal signatures as have been found in the temperatures. The wind speeds between 80

and 90 km are in the range of -50 m s^{-1} to 25 m s^{-1} . Larger amplitudes are found above 90 km.

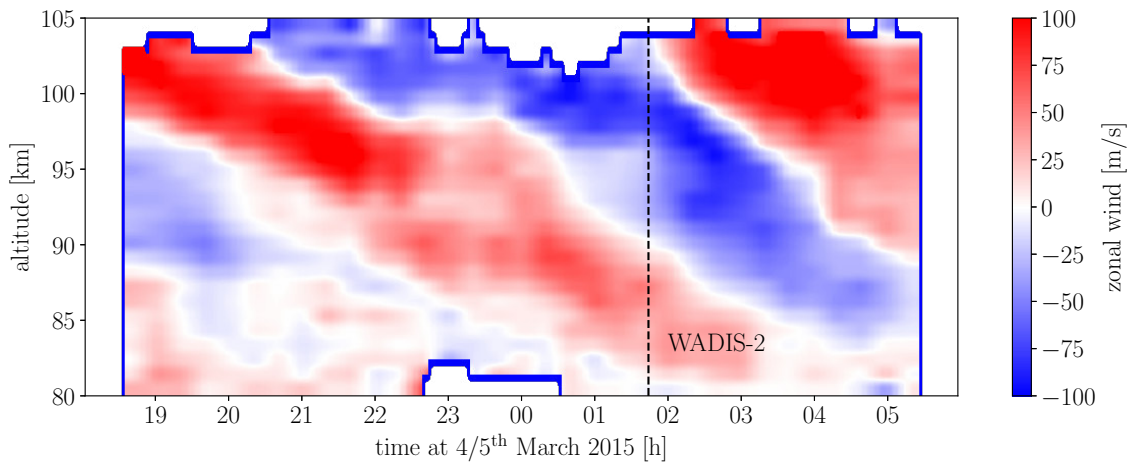


Figure 5.7: Temporal evolution of zonal wind above ALOMAR as a function of altitude in the night from 4th to 5th of March, 2015, deduced from Na-Weber lidar data. The black dashed line marks the launch of the instrumented sounding rocket. Data courtesy of Bifford P. Williams

Conclusions from the background conditions are summarized hereafter. Geomagnetic activity indicates that the ionosphere was in a moderate state. The MAARSY radar did not detect any radar echoes during the launch as well as several hours before and after the launch. Temperature and wind measurements by lidars show strong tidal signatures superposed with lower gravity wave activity.

5.3 Heavy charged particles

Charged aerosols were measured by two identical PDs, placed 180° on the forward deck (see Fig. 5.1 or 4.2).

In this section the current analysis is shown for the particle detectors. The procedure is the same for both instruments. Fig. 5.8 shows raw current measured by the PD1 & 2 as grey noisy profile. To reduce noise level produced by the electronics, a running mean

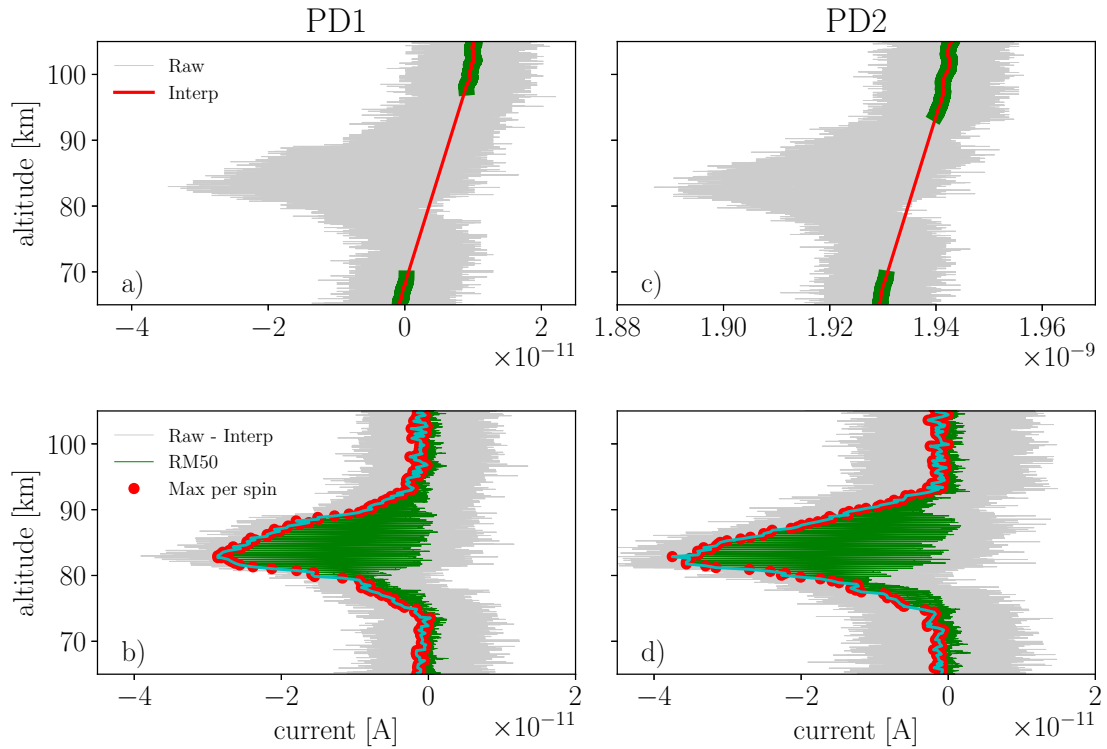


Figure 5.8: WADIS-2 05.03.2015 01:44:00 UT Left panels: Conversion from raw current to charge density for PD1. a): Raw current (gray) and the interpolated trend (red). Green is the smoothed raw current. b): Raw current subtracted by the interpolated trend from the upper panel. Running mean over 50 values (green) and the maximum current per spin (red dots).

over 50 values was applied and the result is shown in Fig. 5.8 by the green line. First of all it appears that both instruments detected a layer being qualitatively in good agreement in terms of altitude range and shape. This is a strong indication that the detected signal is not only an instrumental effect. The PDs were mounted next to the CONE electronic cylinder on the payload's forward deck. Due to an in terms of aerodynamics unfavorable position on the payload the PD-currents are inevitably modulated by the spin frequency of the rocket. This modulation is due to aerodynamics which resulted in periodically changing shock front ahead of the PD. This influence is demonstrated in Fig. 5.9, where an altitude bin of 1 km is shown. The two symmetrically mounted PDs show sinusoidal spin-modulation with clear anti-correlation. When the detectors are faced to the flow, they show maxima in the measured currents. When the PDs are in the shadow, they reveal minimum values, which depend on orientation of the payload relative to velocity vector of the rocket.

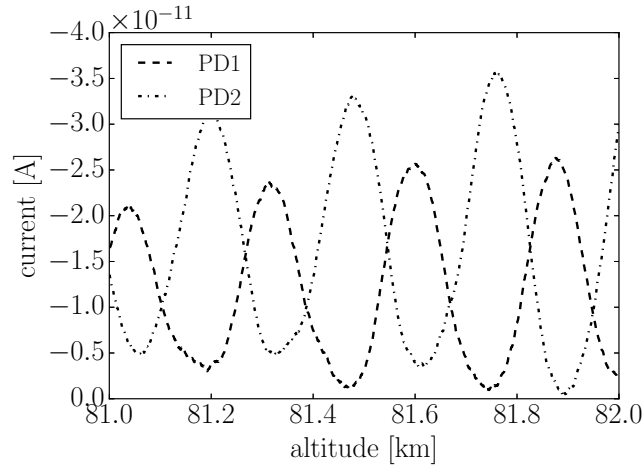


Figure 5.9: Smoothed PD currents (dashed: PD1, dashed-dotted: PD2) as a function of altitude. Reprinted from *Asmus et al.* [2017].

From this aerodynamical reasoning we consider the maxima of the spin-modulated currents for each spin period as the most representative value for the density measurements of the charged MSP. Thus, to derive the charge density based on Eq. 4.3, we pick the local maximum in each spin period from the smoothed green profile. The resulting values are shown in Fig. 5.8 by the red dots. Hence, the altitude resolution of the absolute density measurements by the PDs is limited to the spin rate of 3.27 Hz, i.e. to ~ 300 m. The maximum currents per spin period can now be used to derive charge densities applying of Eq. 4.3 given in Sec. 4.1. In the next section the result of this derivation is presented together with the results from the wave propagation experiment and the positive ion probe.

5.4 Densities of plasma constituents

Fig. 5.10 summarizes the plasma density measurements. The charged dust density obtained from the PDs (see Sec. 5.3) are shown in the left panel. The green and black lines, represent PD1 and PD 2 measurements, respectively. Both instruments detected a pronounced layer of negatively charged MSPs. The shape of the layers is remarkably similar, despite there is systematic offset by a factor of 1.3 of the current measured by PD 1 relative to PD 2. This is due to a lower sensitivity of PD 1 electronics and therefore the green curve is scaled by the offset value. The maximum density can be found around 82 km and revealed a value of $-224 e \text{ cm}^{-3}$. Electron density obtained by the wave propagation experiment (see Sec. 3.4) and positive ion density measured by PIP (see Sec. 3.1 and 4.3) is shown in the right panel of Fig. 5.10. As already mentioned in Sec. 3.4, the wave propagation experiment is not influenced by payload charging effects. Thus, they are considered the best absolute electron density values though with poor altitude resolution. If the negative charge species are represented by free electrons only, quasi neutrality for the ionosphere requires that positive ion density equals electron density. This holds for the ionosphere above ~ 100 km [*Friedrich et al.*, 2011, 2012]. Using this approach, one can normalize measured relative positive ion density above ~ 100 km altitude which was done in this case at 104 km. The resulting absolute positive ion density is shown by the solid black line the right panel of Fig. 5.10. Below 104 km the electron density is decreasing more rapidly than the positive ion density. Hence, there is an increasing dis-

crepancy between both. This indicates strikingly that at these heights the charge balance between electrons and positive ions is not fulfilled. The difference is larger than one order

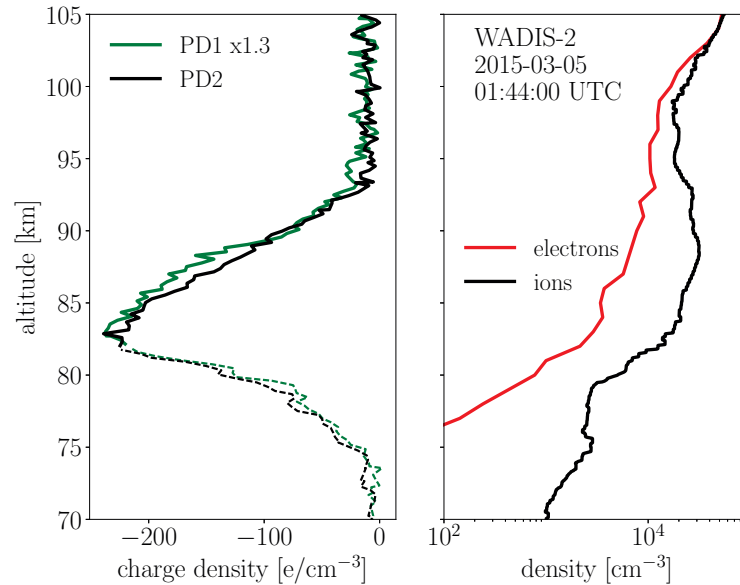


Figure 5.10: Left: Charged MSP profiles measured by the two PDs. The density of PD 1 (green) is multiplied by 1.3. Right: Absolute electron density (red) and positive ion density (black) measured by the wave propagation experiment and PIP, respectively.

of magnitude at 85 km. At least between 75 and 92 km this discrepancy can be attributed to the presence of heavy charged MSPs (left panel in Fig. 5.10). However, the absolute value of this discrepancy between electrons and ions is not reproduced by the PD measurements ($N_i - N_e \sim 1 \times 10^4 \text{ cm}^{-3} \neq N_d \sim 1 \times 10^2 \text{ cm}^{-3}$) which is due to the particle detection efficiency described in Sec. 4.1.1. By means of the combined aerodynamic and electrostatic simulations it was shown that the PDs were not able to detect small MSPs ($r < 1.44 \text{ nm}$ at 82 km). Hence, the missing charge is thought to be on MSPs which are smaller than the detection limit of the PDs.

MSPs are thought to consist of metal rich silicates or iron oxides [Saunders and Plane, 2006; Saunders et al., 2010]. As these materials include iron atoms comparing the measured charged MSP density and the mesospheric iron density measured by resonant fluorescence lidar is of great interest. The existence of iron atoms in altitude ranges where also MSPs are present supports the assumption that iron is part of MSP material. Fig. 5.11 shows both, iron density in the left and charged MSP density in the right panel. The atomic iron layer is located between 78 and 100 km. Its maximum density exceeds $1 \times 10^4 \text{ cm}^{-3}$ around 82 km. The layer has a second density maximum at $\sim 93 \text{ km}$ and has a steep negative gradient above that height. At the lower edge of the layer atomic iron density decreases even more rapidly. The maximum iron density coincides with the peak density of the measured charged MSP. This is yet another experimental evidence that iron is part of MSP material. However, the shape of the iron layer is not reproduced by the charged MSP density which is possibly due to instrumental effects like aerodynamic and electrostatic filtering. Interestingly, the charged MSP layer expands to lower altitudes compared to the iron layer. Since the metal layer has its origin in ablated meteoroids one can use the iron density profile to estimate the meteor

ablation peak height. This will become useful in Sec. 6.5. Sodium densities (not shown here) were measured during WADIS-2 by lidar. However, sodium is thought to be no major constituent of the MSP material and hence results are no shown here.

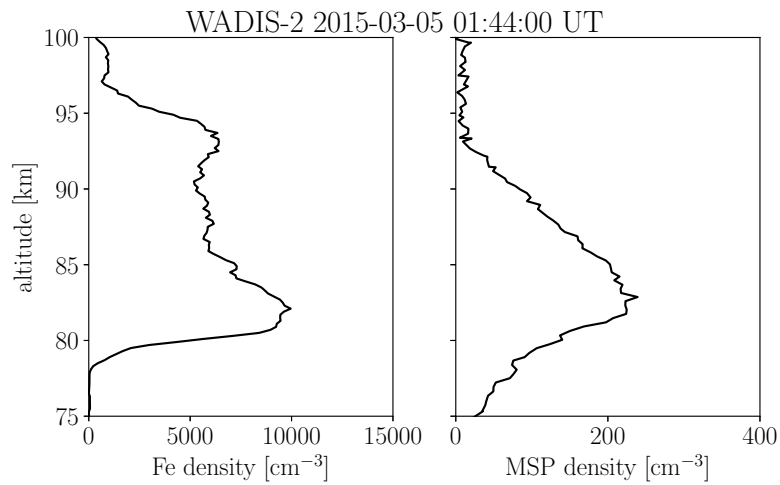


Figure 5.11: Left: Atomic iron density obtained by resonant fluorescence lidar measurements. Right: MSP density obtained from PD 2. Fe data courtesy of Josef Höffner.

5.5 Small scale fluctuations

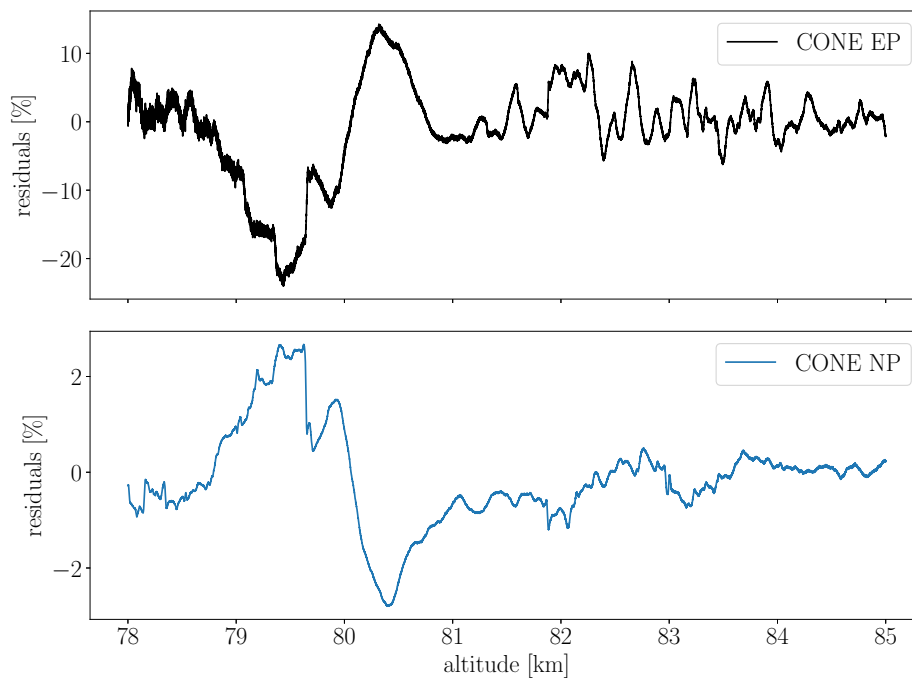


Figure 5.12: Residuals of electron (black) and neutral (blue) density measured during the upleg of WADIS-2 flight (05.03.2015 01:44:00 UT).

In this section fluctuations of neutral- and electron density are presented. In Fig. 5.12 the residuals of electron (CONE EP) and neutral (CONE NP) densities between 78 and 85 km are shown.

The electron density fluctuations are larger compared to the neutral density fluctuations by a factor of approximately 5. Plasma fluctuations are usually larger than fluctuations in the neutral gas since the scale heights of neutrals and electrons are not equal ($H_e \neq H_n$). This has also been shown by measurements e.g., *Lübken et al.* [1994] and *Thrane et al.* [1994]. There are similar structures in the fluctuations of both electron and neutral density. Notably, the structures are in anti phase which means a region with decreased electron density corresponds to an increased neutral density. This is in agreement with previous rocket measurements conducted in the vicinity of PMSE [*Lübken et al.*, 1994].

A useful tool to visualize the structures in density fluctuations is to look at their wavelet transform [*Torrence and Compo*, 1998; *Strelnikov et al.*, 2003]. Figs. 5.13 and 5.14 show in left panels the altitude profile of the residuals of electron and neutral density, respectively. In right panels the power spectral density obtained from wavelet transform as a function of spatial scale and altitude is illustrated. It is apparent, that starting at 78 km electron density fluctuations become larger and show well defined structures around 79, 82 and 83 km.

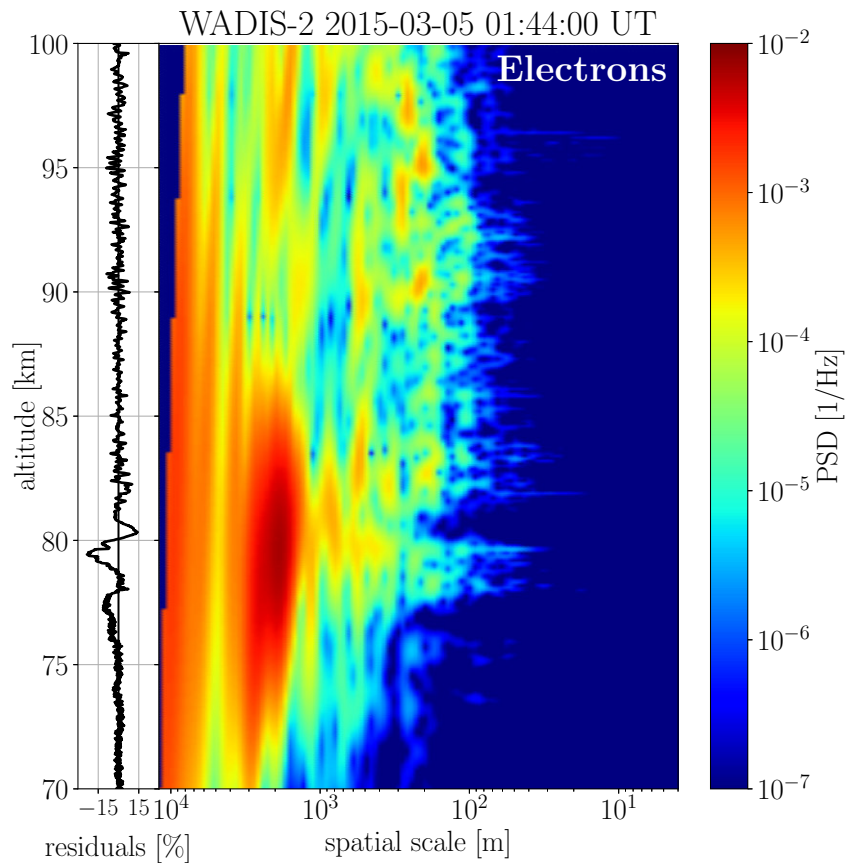


Figure 5.13: Left: measured electron density fluctuations (residuals) of the forward CONE EP from the upleg part of the WADIS-2 flight. Right panel: Wavelet power spectrum of the residuals. The wavelet transformation was performed using a 12th order Morlet wavelet. Reprinted from *Asmus et al.* [2017].

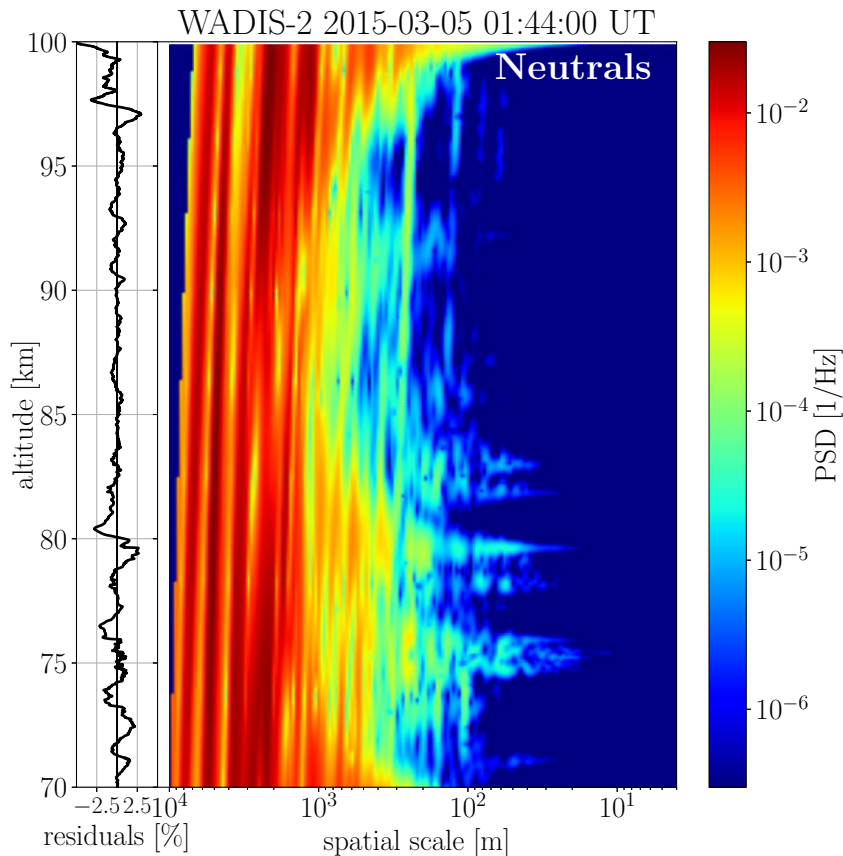


Figure 5.14: The same as Fig. 5.13, but for neutral density. Reprinted from *Asmus et al.* [2017].

Layers of enhanced fluctuations in electron and neutral density are present at the same altitudes as also seen in Fig. 5.12. Since the measurements were conducted in both the same space and time, they describe the collective motion of dusty plasma which is a striking advantage of the measurement technique. Moreover, from the spectral behavior of these fluctuations we can derive the energy dissipation rate and thereby the Schmidt number. This is described in the subsequent section.

5.6 Spectral analysis

The wavelet spectra presented in Sec. 5.5 were further analyzed using the method described in Sec. 4.4. Fig. 5.15 shows spectra of electron and neutral density fluctuations at 82 km and the corresponding theoretical models fitted to the data. The power spectrum of the electron density fluctuation is extended to smaller scales by approximately 10 m than the neutral density fluctuation power spectrum. Fitting the theoretical *D&K*-spectrum [*Driscoll and Kennedy*, 1985] to the electron density fluctuation spectrum yields a Schmidt number of 4.2 ± 1.4 . At higher frequencies $f \gtrsim 150$ Hz the power spectral density is determined by the instrumental noise (grey lines). In the case of electron density measurements there is a peak around 200 Hz which may be linked to a feedback of data storage on an SD-card. The noise of the neutral density measurements is flat and has no distinct peaks.

As exemplary shown in Fig. 5.15 energy dissipation rates and Schmidt numbers were derived for numerous height bins. The results are shown in Fig. 5.16.

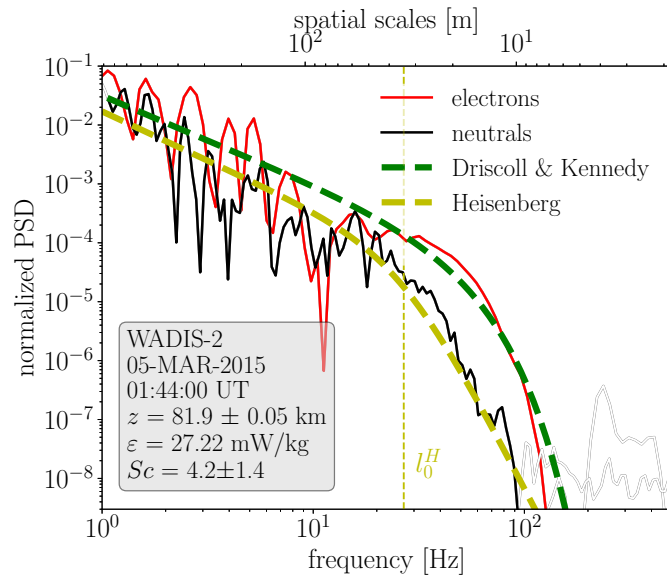


Figure 5.15: Global wavelet spectrum from 81.85 to 81.95 km of electron density fluctuations (solid black line) and of neutral density fluctuations (solid red line). The dashed lines shows the best fit of the theoretical models of *Driscoll and Kennedy* [1985] (green) and of *Heisenberg* [1948] (yellow). ε was kept constant for the fit of the *D&K* model to the electron density fluctuations and is obtained from the fit of the *Heisenberg* model to the neutral density fluctuations. The *D&K* fit yields a Schmidt number of $Sc = 4.2 \pm 1.4$. The vertical dashed yellow lines indicate the inner scale l_0^H . Adapted from *Asmus et al.* [2017].

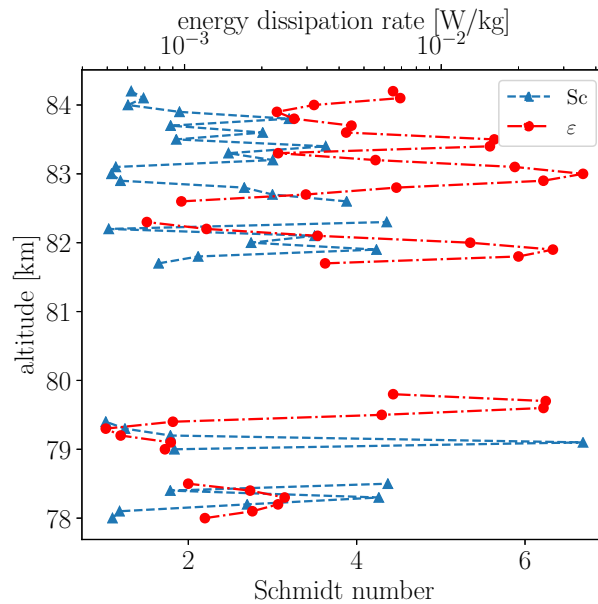


Figure 5.16: Schmidt number (blue, triangles) and energy dissipation rate (red circles) profiles between 78 and 85 km for the WADIS-2 launch (2015-03-05 01:44:00 UT).

At 83 km or between 79 and 80 km larger Schmidt numbers coincide with smaller ε -values. On the other hand there are also layers where increased ε -values accompany increased Schmidt number e.g. at 82 km. Yet, there is no clear evidence that turbulence correlates with electron Schmidt number. This will be further discussed later in Sec. 7.4 of Chap. 7.

However, to clarify whether the ε -values are exceptional or not let us compare to a mean winter profile given in *Lübken* [1997]. Fig. 5.17 shows both profiles, WADIS-2 as red and mean winter as blue line. Indicated by the dashed black line is the minimum dissipation rate

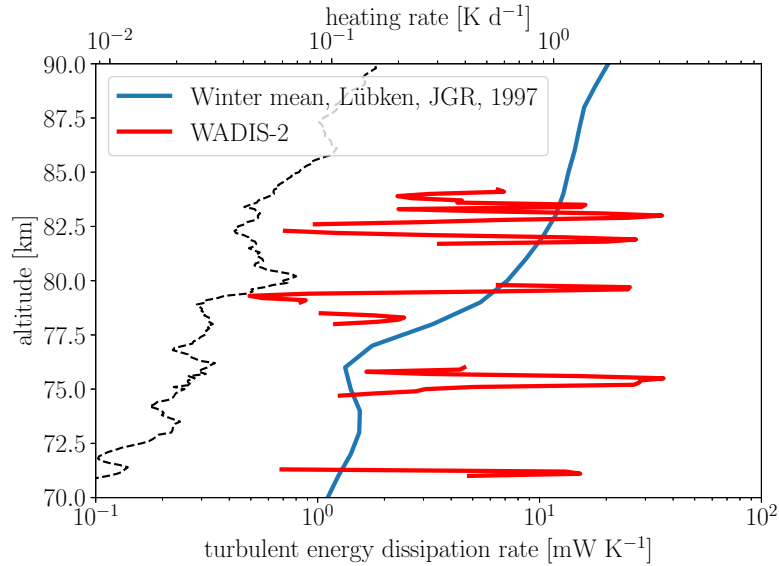


Figure 5.17: Turbulent energy dissipation rate measured in situ during WADIS-2 in red and a mean winter profile also from in situ measurements in blue [*Lübken*, 1997]. The black dashed indicates theoretical minimum dissipation rates ($\varepsilon_{min} \approx \frac{\nu}{N^2}$).

which is approximately $\frac{\nu}{N^2}$ since in the atmosphere turbulent diffusion cannot be smaller than molecular diffusion [*Lübken*, 1993]. Apparently, below 77.5 km the ε -values measured during WADIS-2 are approximately one order of magnitude larger in their maximum values than the winter mean indicating high turbulent activity here. The measured values reveal a large variability of turbulent energy dissipation rates in comparison to the mean profile. To assess the spatial scales down to which density fluctuations of neutrals and electrons were structured the inner scales $l_0^H, l_0^{D\&K}$ were derived (see Sec. 2.1.2.1 and 2.1.2.2). In addition the *Kolmogorov* microscale η_{Kol} and the *Batchelor* scale η_{Ba} were calculated to find the spatial scale where all turbulent energy was dissipated. All scales are shown in Fig. 5.18, where η_{Kol} and η_{Ba} are shown by blue and orange lines, respectively.

The scale where molecular diffusion starts to destroy turbulent structures is defined by the inner scales. This transition is nearly the same for electrons and neutrals at scales between approximately 20 and 80 m. All structures were destroyed by molecular diffusion between approximately 3 and 10 m. Hence, there were no turbulent structures at the radar Bragg wavelength present.

In the next step we relate the derived Schmidt numbers to charged MSP radii as done by *Lübken et al.* [1998] for charged ice particles in summer. We will therefore use the theory of *Cho et al.* [1992] briefly summarized in Sec. 2.2.1 and adapt the idea of *Lübken et al.* [1998] to obtain MSP radii. The derivation and limitation of this method are discussed in section 7.2.

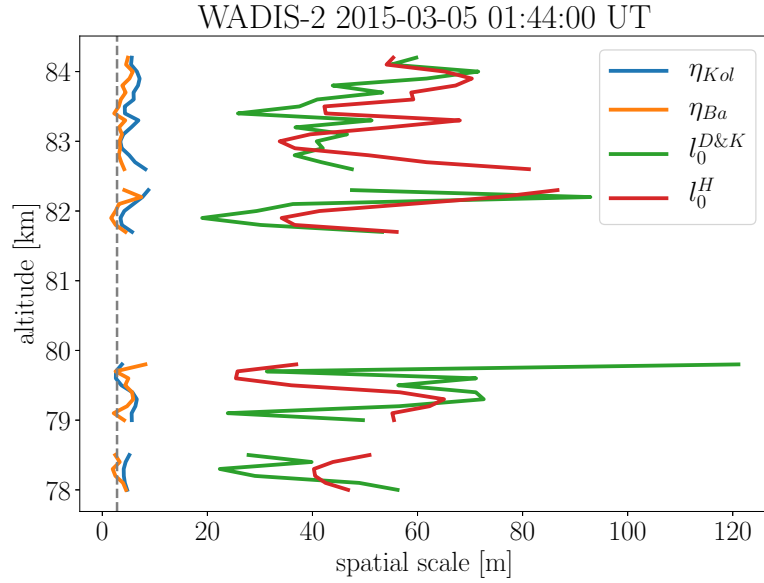


Figure 5.18: Scales of measured density fluctuations. The grey dashed line indicates $\lambda_{\frac{1}{2}}$ of the MAARSY radar.

5.7 Mean particle sizes

As a final result, Schmidt numbers, derived mean charged particle radii and the corresponding transition between polarization and hard sphere interaction is shown in Fig. 5.19. In the left panel red dots indicate derived Sc from electron density fluctuations and their uncertainty is given by black error bars and gray shaded area, respectively. The orange dashed line marks the transition Schmidt number. Apparently, the derived Schmidt numbers are on the order of the transition Schmidt number of which some are significantly larger than one. The right panel of Fig. 5.19 shows calculated charged particle radii (green dots) using Eq. 4.20 for Schmidt numbers smaller than Sc_{tr} and Eq. 4.24 for larger Sc . The uncertainty is given by black error bars and gray shaded areas, respectively. The derivation of uncertainties is given in the Appendix D. The particle radii represent mean radii of the charged particle ensemble [Lübken *et al.*, 1998]. For a maximum Schmidt number of 6.6 and a minimum of 1.0 the corresponding mean radii are 0.75 and 0.08 nm, respectively. For the derivation of mean radius for the maximum Schmidt number the hard sphere case (Eq. 4.24) and for the minimum Schmidt number the polarization interaction case (Eq. 4.20) were used. These values indicate that the majority of the charged MSPs were not detected PD due to the aerodynamic and electrostatic filtering. Nevertheless, this supports the assumption that the difference between electrons and ions are at least above 80 km can be explained by negatively charged primary small MSPs.

MSPs are growing from ablated meteoric material. There is a continuous input of meteoroids into the Earth's atmosphere. Hence, MSP will be existent in a variety of sizes which can be described by a size distribution function. For neutral MSPs the shape of distribution is thought to be log-normal like [e.g., Megner *et al.*, 2006]. However, the distribution function for charged MSPs is still unknown and yet not directly measured. In the next section we assess the width of an assumed distribution function based on the simultaneous common volume in situ measurements described above.

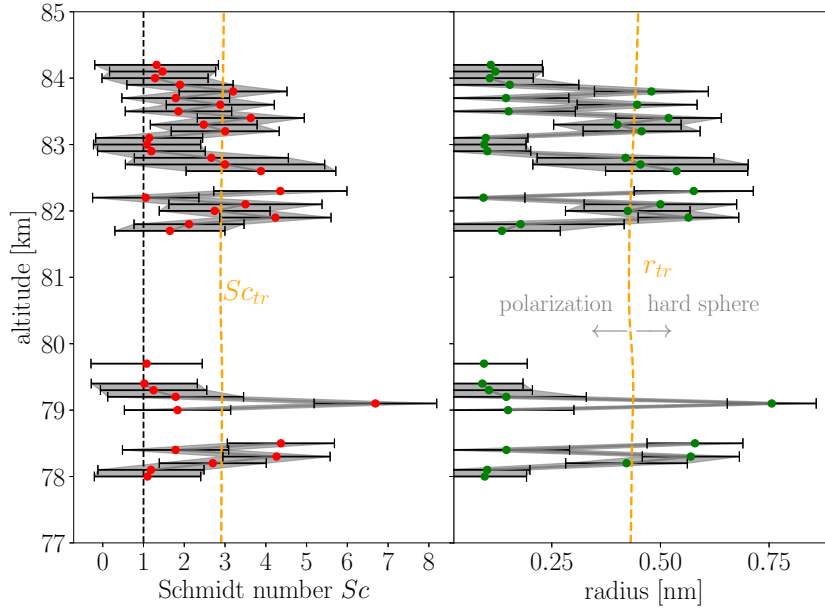


Figure 5.19: **Left:** Schmidt number as a function of altitude obtained from fitting the *D&K* theoretical model (red dots). For orientation $Sc = 1$ is marked by the black dashed line and the transition of polarization and hard sphere interaction by orange dashed line Sc_{tr} . The black bars and grey shaded areas indicate the error of the Schmidt numbers (see text for details). **Right:** Mean charged particle radius ($r \sim \sqrt{Sc}$) obtained from Schmidt numbers (green dots). The orange dashed line indicate again the transition between polarization and hard sphere interaction. Error bars are given in black and grey shaded areas (see text for details). Reprinted from *Asmus et al.* [2017].

5.8 Estimate of a particle size distribution

Model calculations show that neutral MSP size distribution can be described by log-normal like distributions [Megner *et al.*, 2006; Plane *et al.*, 2014]. Furthermore, recent works in the MLT research also make use of log-normal approaches when it comes to particle size distributions [e.g., von Cossart *et al.*, 1999; Berger and von Zahn, 2002; Yamamoto, 2014; Bailey *et al.*, 2015; Rusch *et al.*, 2016]. However, the charged particle size distribution is mainly influenced by two properties. First of all the reservoir of neutral MSP available to be charged and secondly the charging rate of particles which is proportional to r^2 . For smallest particles $\lesssim 1.5$ nm the probability of to the MSP attached electrons remain on the MSP is not necessarily one but smaller [e.g., Megner and Gumbel, 2009; Plane *et al.*, 2014; Baumann *et al.*, 2015]. As neutral MSPs around 80 km have the largest densities at smallest radii the charging process will lead to a shift of the distributions mean value [Megner *et al.*, 2008]. The shape of the distribution function is assumed to remain log-normal. Thus, MSP size distribution function is defined as

$$f(r) = \frac{N_{d^-}}{\sqrt{2\pi} \ln \sigma (r - \lambda)} \exp\left(-\frac{1}{2} \left(\frac{\ln \frac{r-\lambda}{\bar{r}}}{\ln \sigma}\right)^2\right), \quad (5.1)$$

where N_{d^-} is the density of all negative charged MSP, σ is the distributions width and \bar{r} is its mean. We assume a lower radius limit of 0.2 nm given the MSP monomer and hence added λ as a limiting parameter [Hunten *et al.*, 1980].

Integrating Eq. 5.1 over all radii r gives the total number density of charged MSPs

$$N_{d^-} = \int_0^{\infty} f(r)dr. \quad (5.2)$$

This density would be seen by a PD with 100 % detection efficiency at the electrode. However, the instrument measures only particles with radii larger than the critical radius r_c . Thus its current represents only a part of the entire population. This is described for the WADIS-2 conditions in Sec. 4.1.1 yielding a height dependent critical radius. The fraction of the particle distribution which can be measured by the detector is given by the detection probability function $p(r)$. This function was calculated using combined aerodynamical and electrostatic simulations (see Sec. 4.1.1) for particles in a mass range from 1000 to 60 000 amu. By means of $p(r)$ the measured charge density by the PD can be expressed as the integral over all r of the product of the distribution function $f(r)$ and the detection probability $p(r)$.

$$N_{PD} = \int_0^{\infty} p(r) \cdot f(r)dr \quad (5.3)$$

$p(r)$ is a tabulated function and the probabilities for particles with radii between 0.58 and 2.28 nm to be detected are given Tab. 5.2.

Table 5.2: Particle detector detection efficiency $p(r)$ at 82 km.

mass [amu]	radius [nm]	detection efficiency [%]
1000	0.58	0
2500	0.79	0
5000	1.00	0
10000	1.26	0
15000	1.44	18.5
20000	1.58	25.6
25000	1.70	29.8
30000	1.81	32.0
35000	1.91	33.3
40000	1.99	34.5
45000	2.07	35.4
50000	2.15	37.3
55000	2.22	36.9
60000	2.28	39.2

The difference between electron and positive ion density between 75–95 km can be explained by the presence of negative charged heavy aerosols which is in agreement with findings by e.g., Friedrich *et al.* [2011, 2012]; Rapp *et al.* [2011]. Moreover, during night time the charged fraction of MSPs carry only one elementary charge as the majority is smaller than ~8 nm [e.g., Rapp and Lübken, 2001; Rapp *et al.*, 2011; Robertson *et al.*, 2014; Baumann *et al.*, 2013, 2015; Asmus *et al.*, 2015b]. With this known, one can assume that the difference between electrons

and positive ions above 80 km (see Fig. 5.10) is represented by the entire negative charged dust population, N_{d^-} , which therefore can be expressed by the difference of the other two plasma constituents:

$$N_{d^-} = N_{i^+} - N_e \quad (5.4)$$

where measured densities of positive ions and free electrons are N_{i^+} and N_e , respectively.

Now one can relate the measured plasma densities with the size distribution of charged particles by combining Eq. 5.2, and 5.4.

$$N_{i^+} - N_e = \int_0^{\infty} f(r) dr \quad (5.5)$$

As Eq. 5.3 and 5.5 use the same size distribution function $f(r)$ given by Eq. 5.1 only one parameter of the distribution is unknown which is its width σ . From independent Sc -measurements presented in Sec. 4.5 the mean MSP radius, \bar{r} , was derived. The results are summarized in Fig. 5.19. σ can be obtained using an iterative scheme and below the results of this derivation are presented.

From the aerodynamical simulation described in Sec. 4.1.1 it is apparent that below 82 km MSP density measurements are heavily influenced by the aerodynamics. Therefore, to characterize the MSP properties and derive the size distribution function of charged MSP the data measured above that altitude are used since they represent best quality data.

For the derivation of the charged particle size distribution a 100 m layer at 82 km is used which also coincides with the maximum measured charge density. The value of measured charged particles in this layer is $N_{PD} = 224 \text{ cm}^{-3}$ as shown in Fig. 5.10. The independent Sc -measurements presented in Sec. 4.5 reveal a mean MSP radius of $\bar{r} = 0.56 \text{ nm}$ also shown in Fig. 5.19. The total charge difference $N_{i^+} - N_e$ at 82 km is $10\,000 \text{ cm}^{-3}$. This value is two

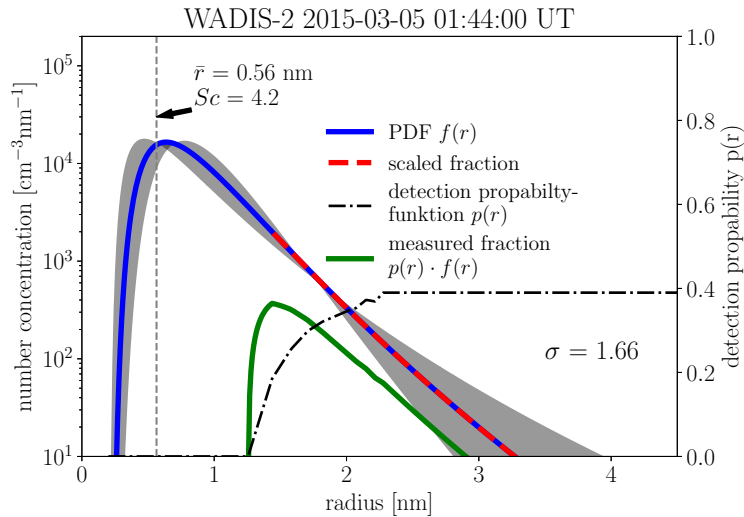


Figure 5.20: Particle size density as a function of radius (solid lines, left hand y-axis). The blue line shows the estimated log-normal size distribution and the green line the size distribution most likely seen as integral by the PD at 82 km. The red dashed line indicates the fraction of the distribution contributing to the PD current. The dashed dotted line shows the detection probability of the PD as obtained from aerodynamic simulations (right hand y-axis). Reprinted from *Asmus et al.* [2017].

orders of magnitude larger than the MSP charge density measured by the PD. Using these values and inserting them into Eq. 5.1, 5.3, and 5.5 the corresponding width is found to be $\sigma = 1.66$. The procedure of the iterative scheme is as follows. Having all parameters fixed except σ , the width is adjusted until the integral of $p(r) \cdot f(r)$ over all r reaches the measured peak value of $224 e \text{ cm}^{-3}$ and the integral of $f(r)$ over all r equals the measured charge difference between electrons and positive ions of $10\,000 e \text{ cm}^{-3}$.

The resulting charged particle size distribution at 82 km is shown in Fig. 5.20 by the blue line. This distribution function, multiplied by the detection probability function given by the dashed-dotted black line (left y-axis) gives the green line which is the size distribution of the MSP measured by the PD. With the green and black dashed-dotted curve the red part of the distribution function (blue) can be reconstructed.

The analysis of Schmidt numbers summarized in Fig. 5.19 suggests, that their might be several sublayers with different mean particle sizes in the measured charged MSP layer in the height range between 75 and 90 km. Hence, a Sc of the height range 81 km to 85 km is derived by means of Schmidt numbers larger than Sc_{tr} which yields $Sc = 3.3$ and a corresponding radius of $r = 0.48 \text{ nm}$. The difference between mean Sc and the value found at 82 km is smaller than uncertainty of the analysis and is therefore not significant.

5.9 Absence of PMWE during WADIS-2

Statistics of PMWE measured by VHF radar showed that those echoes primarily occur around local noon where ionization by UV light is present [Zeller *et al.*, 2006; Latteck and Strelnikova, 2015]. However, despite lower occurrence rates even in the absence of sun light echoes can be observed. It has been shown that in order to form refractive index variations at the Bragg scale of a 50 MHz radar electron density and neutral turbulence has to be sufficiently large [Lübken *et al.*, 2007]. During WADIS-2 the mesosphere was monitored by the MAARSY radar. However, as shown in Fig. 5.4 there were no radar echoes at the time of launch. The lower detection limit of the MAARSY radar ($f = 53.5 \text{ MHz}$) for PMWE was found to be $\eta_{lim} = 4 \times 10^{-18} \text{ m}^{-1}$ [Latteck and Strelnikova, 2015]. Whether this threshold is exceeded between 78 and 85 km during the upleg phase of WADIS-2 can be checked by means of known constants and in situ measured quantities inserted into the equation of radar volume reflectivity given in a corrected version in Lübken [2014] by

$$\eta = 8\pi^2 \cdot k^4 \cdot Q^{9/2} A \chi_n \varepsilon^{-1/3} \eta_{Kol}^{11/3} \cdot \left(y^{-11/3} + y^{-3} \right) \times \exp \left(-A_{3\vartheta} \left(\frac{3}{2} y^{4/3} + y^2 \right) \right), \quad (5.6)$$

where $k = 2 \cdot 2\pi / \lambda$ is the Bragg wavenumber, $Q = 2$, $A = 0.033 \cdot 1.74$, ε is the energy dissipation rate, $\eta_{Kol} = (\nu^3 / \varepsilon)^{1/4}$ is the Kolmogoroff microscale and $y = Q^{3/2} \cdot \eta_{Kol} \cdot k$. ε and the kinematic viscosity ν are obtained from CONE measurements. $A_{3\vartheta} = \frac{\alpha}{Q^2 \cdot Sc}$ with $\alpha = 0.83$ and Sc is the Schmidt number. The variance dissipation rate χ_n is defined as

$$\chi_n = f_\alpha \cdot \frac{Ri \cdot \varepsilon}{Pr^t \omega_B^2} \cdot M_n^2, \quad (5.7)$$

where $f_\alpha = 2$ is a normalization constant, $Ri = 0.81$ is the Richardson number, $Pr^t = 1.0$ is the Prandtl number and ω_B^2 is the buoyancy frequency. The background gradient of potential

refractive index variation M_n is given by

$$M_n = \frac{2\pi r_e}{k^2} \cdot \left(\frac{N_e \omega_B^2}{g} + \frac{dN_e}{dz} - \frac{N_e}{H_n} \right) \quad (5.8)$$

where N_e is the absolute electron density, g is the Earth's gravitational acceleration, $\frac{dN_e}{dz}$ is the electron density vertical gradient and H_n is the neutral density scale height. By means of in situ measurements of temperature, neutral and electron density, turbulent energy dissipation rate and Schmidt number, the volume reflectivity η can be calculated. The results are shown in Fig. 5.21 where Schmidt number and energy dissipation rate are shown in the left panel and the corresponding reflectivity in the right panel. Obviously, the reflectivity never exceeds the MAARSY threshold of $4 \times 10^{-18} \text{ m}^{-1}$. The region below the threshold is indicated by the hatched area. Moreover, the values are several orders of magnitude too small for MAARSY to produce a significant echo. Typical radar volume reflectivities of PMWE are in the range of $4 \times 10^{-18} \text{ m}^{-1}$ to $1 \times 10^{-13} \text{ m}^{-1}$ [Latteck and Strelnikova, 2015].

Based on the measured quantities and the standard theory of radar volume reflectivity we can conclude here that either turbulence was too weak, electron density too low or charged particles too small to create detectable echoes. As shown in Fig. 5.17 the turbulent energy dissipation rates were in the order of mean winter values obtained from rocket measurements Lübken [1997]. The observed electron density was moderately high compared to other

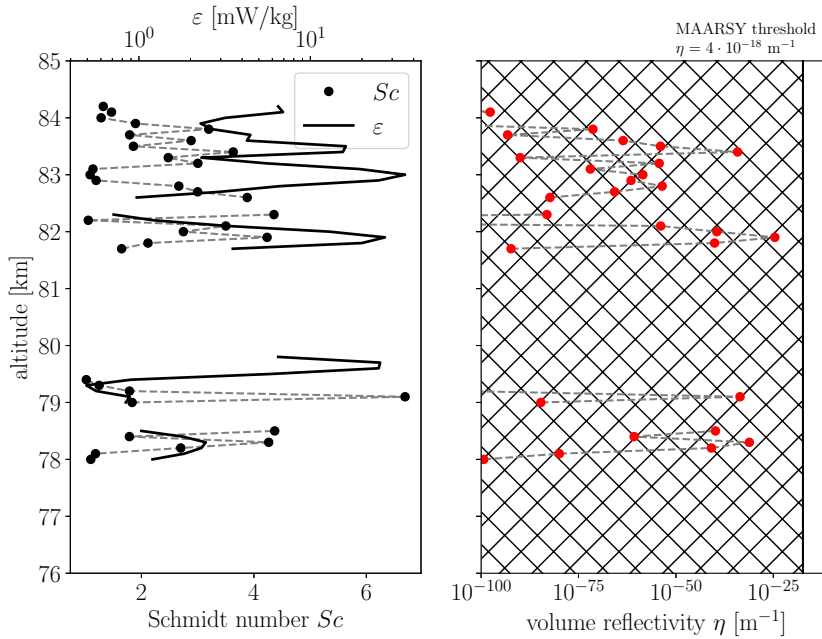


Figure 5.21: **Left:** Schmidt number and turbulent energy dissipation rate profiles for WADIS-2. **Right:** Corresponding volume reflectivity. Hatched area indicates volume reflectivities below the MAARSY threshold.

electron density measurements made by the Faraday rotation technique [Friedrich and Torkar, 2001; Friedrich, 2016]. The MSP mean size was found to be small but in agreement with earlier findings [Strelnikova et al., 2007; Fentzke et al., 2009; Robertson et al., 2014]. Hence, the absence of PMWE can be attributed to both too weak turbulence and too small charged particles. Below 75 km neutral turbulence was also present but in order to create coherent radar echoes

the electron density was too low.

In summary, the fact that PMWE were not detected by MAARSY during the WADIS-2 flight is consistent with in situ measurements of electron density, turbulent energy dissipation rates and electron Schmidt number.

Chapter 6

Results 2: Charging model

During nighttime ionization is mainly due to cosmic rays, energetic particle precipitation and UV scattered light from the geo-corona. The number densities of negatively and positively charges are equal in the ionosphere which is referred to by the term quasi-neutral. But besides free electrons and positive ions there are also other charged constituents involved in the charge balance of the D and lower E-region. Free electrons can form negative ions via three body reactions depending on the background neutral density. The destruction of those negative species is heavily influenced by the ambient density of atomic oxygen (mainly by the reaction $O + O_2^- \rightarrow O_3 + e^-$) [e.g., *Thomas and Bowman, 1985*]. Absolute density measurements of atomic oxygen are highly challenging. A common technique to obtain O is to look for airglow emissions. This can be done e.g., in situ on board of sounding rockets [*Dickinson et al., 1980; Sharp, 1991*] or by remote techniques such as satellite borne optical instruments. A recent development is the usage of rocket borne catalytic sensors to measure atomic oxygen density in the mesosphere [*Eberhart et al., 2015*]. In addition to electrons, positive and negative ions there can be charged aerosols which can be MSP or ice particles. These aerosols can either be positively or negatively charged [e.g., *Rapp and Lübken, 2001; Rapp et al., 2005; Robertson et al., 2014*]. The amount of charged particles can be large and exceed the electron density [e.g., *Friedrich et al., 2012*]. Their effect on lower ionosphere physics is therefore not negligible. To understand the nighttime polar ionosphere including negative ions and charged particles, modeling became more important.

There is a vast number of ionospheric models with various levels of complexity. Simple models, considering meteor smoke particles and negative ions were presented by e.g., *Plane et al. [2014]; Asmus et al. [2015b]*. A more sophisticated attempt was made by *Baumann et al. [2015]* using the Sodankylä Ion Chemistry (SIC) model. However, the main impact of MSP on the charge balance was also reproduced by simplified models, allowing for an easy-to-use application. Notably, the impact of atomic oxygen on the charging of MSPs and hence on the D-region charge balance is still not well understood. In the frame of this work we will use an improved version of the model given in *Asmus et al. [2015b]* to reproduce the dusty plasma measurements conducted during WADIS-2. In the course of this analysis we will try to shed a new light on open questions pertaining to the D-region charge balance involving MSP and atomic oxygen.

After we have a quick look at the measured plasma parameters during WADIS-2 in Sec. 6.1 we shortly recapitulate the model equations and assumptions in Sec. 6.2. A description of model inputs is given in Sec. 6.3 which is followed by the results obtained by using those inputs.

6.1 Estimate of charged particle fraction

During night the fraction of negative charge particles can be estimated by comparing positive ion and electron density [Friedrich *et al.*, 2012]. If one neglects photodetachment processes (which is reasonable during winter night time) and reactions involving atomic oxygen the electron density can be inferred from the positive ion density using [Friedrich *et al.*, 2011, 2012]

$$n_e = \frac{n_i^+}{1 + \frac{\beta}{\alpha_{ii}} \frac{M^2}{n_i^+}} \quad (6.1)$$

where n_i^+ is the positive ion density, β is the electron attachment rate, $\alpha_{ii} = 6 \times 10^{-8} \text{ cm}^3 \text{ s}^{-1}$ is the ion-ion-recombination rate and $M = \text{O}_2 + \text{N}_2$ is the background density [Dieminger *et al.*, 1996]. Ignoring MSPs this assumption involves the balance between electrons, positive and negative ions fulfilling charge neutrality. By means of the difference between calculated and measured electron density one can estimate the fraction of charged aerosols. The result of plasma density measurements for WADIS-2 shown in Fig. 6.1 where blue lines indicate electron and the red line positive ions. We used a ratio $\beta/\alpha_{ii} = 1.9 \cdot 10^{-31}$ which is in

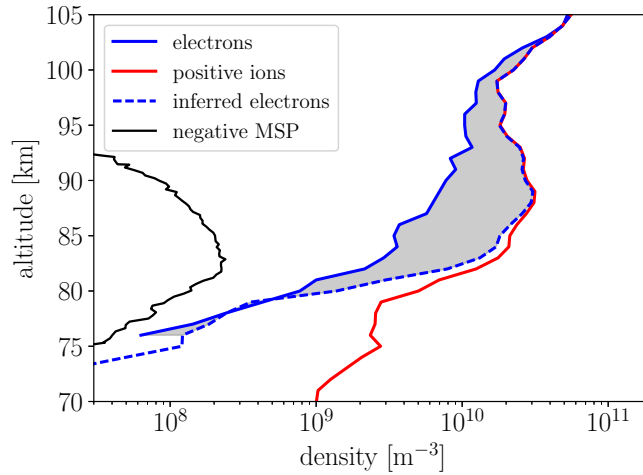


Figure 6.1: Measured electron (solid blue) and positive ion (red) density profiles from WADIS-2 2015-03-05 01:44:00 UT shown by solid lines. The dashed blue lines indicates electron density inferred from Eq. 6.1 neglecting charged MSP and atomic oxygen reactions. Negative charged MSP are given by the black solid line.

agreement with earlier findings by e.g., Friedrich *et al.* [2012]. The measured electron density is lower than would be expected from Eq. 6.1. It is assumed that this difference is due to the presence of negatively charged aerosols. Indeed charged particles were measured by the PDs but cannot explain the difference quantitatively. This is due to the instrumental limitations introduced by aerodynamical and electrostatic filtering (see Sec. 4.1.1). The grey shaded area in Fig. 6.1 represents the difference between the measured and the from Eq. 6.1 inferred electron density. It shows the region where negative species other than negative ions are present. However, this very simple approximation cannot explain the measurements of WADIS-2 quantitatively. We therefor will use a more sophisticated model in the next section to obtain also negative ion and charged MSP densities. The 1d charging model is described in detail in Sec. 6.2.

6.2 Charging model

Charge balance of the ionosphere can be investigated also by models. Here we look at the nighttime case i.e. without sunlight. In a simplified manner one can derive the densities of the ionospheric plasma in an equilibrium state ($\frac{\partial}{\partial t} = 0$) by means of quasi neutrality. Each component of the plasma is determined by sources and losses. The model used is based on the work of *Reid* [1990] and *Jensen and Thomas* [1991] and its further developments by *Rapp and Lübken* [2001]; *Robertson et al.* [2014]; *Asmus et al.* [2015b]. In the present version of the model we calculate the equilibrium density of electrons, positive and negative ions as well as MSPs in their charge state ($Z = -1, 0, +1$). An explanation for the limited range of Z is given later in this section. The densities obey the continuity equations in the steady state

$$\frac{\partial n_e}{\partial t} = Q - \alpha_{ie} n_e n_i - k_M M n_{O_2} n_e + k_{ON} n_i^- - D^- n_e = 0, \quad (6.2)$$

$$\frac{\partial n_i^+}{\partial t} = Q - \alpha_{ie} n_e n_i^+ - \alpha_{ii} n_i^+ n_i^- - D^+ n_i^+ = 0, \quad (6.3)$$

$$\frac{\partial n_i^-}{\partial t} = k_M M n_{O_2} n_e - \alpha_{ii} n_i^+ n_i^- - k_{ON} n_i^- - D^- n_i^- = 0, \quad (6.4)$$

$$\frac{\partial n_d(Z = -1)}{\partial t} = D^- n_e + D^- n_i^- - D^+ n_i^+ = 0, \quad (6.5)$$

$$\frac{\partial n_d(Z = 0)}{\partial t} = D^+ n_i^+ + D^- n_e - D^- n_i^- = 0, \quad (6.6)$$

$$\frac{\partial n_d(Z = +1)}{\partial t} = D^+ n_i^+ - D^- n_e - D^- n_i^- = 0. \quad (6.7)$$

In the following, we will describe each of the above equations. Values of reaction rates used are given in Tab. 6.1. These values are commonly used values [*Plane et al.*, 2014]. Eq. 6.2 defines the equilibrium electron density. The production of an electron-ion pair is controlled by the production rate Q . The loss is given by the recombination with positive ions with the rate α_{ie} , the attachment of electrons to molecules to form negative ions and the attachment of electrons to MSP. Q is estimated by assuming that during nighttime there are no further positive charged particles except positive ions which can be measured and not other negative charge carriers but free electrons. Here we also use the assumption that the rates of ion-pair production and dissociative recombination are balanced as previously used by e.g., *Jensen and Thomas* [1991]; *Plane et al.* [2014]. In this case the temporal change of the electron or positive ion density can be written as

$$\frac{\partial n_e}{\partial t} = Q - \alpha_{ie} n_e n_i^+. \quad (6.8)$$

In a steady state when $\frac{\partial n_e}{\partial t} = 0$ Eq. 6.8 can be rewritten as

$$Q = \alpha_{ie} n_e n_i^+. \quad (6.9)$$

Assuming now that the density of electrons and positive ions is equal to one can calculate Q by

$$Q = \alpha_{ie} n_{i^+}^2. \quad (6.10)$$

The electron-ion recombination rate α_{ie} is obtained using the semi empirical model from *Friedrich et al.* [2004]. The model utilizes the measured electron density. Since the measured electron density may not represent the total amount of negative charges, the electron-ion-recombination rate may be overestimated.

The loss of free electrons due to attachment to molecules is given by

$$k_M M n_{O_2} n_e = [k_{N_2} n_{N_2} + k_{O_2} n_{O_2}] n_{O_2} n_e,$$

where k_{N_2} is the rate of the termolecular reaction of N_2 , O_2 and e^- . Here we use that the primary production of negative ions is due to formation of O_2^- . We neglect further charge transfer forming other negative ions [e.g., *Friedrich et al.*, 2011, 2012; *Plane et al.*, 2014]. k_{O_2} is the rate of the termolecular reaction of two N_2 and e^- . Electrons are released from O_2^- reacting with atomic oxygen to form ozone O_3 . We do not keep track of ozone in this model as it in our simplified case is not involved in other reactions and is a minor species. Finally, free electrons can attach to dust particles. The rate α_e depends on the charge state Z and the radius r of the MSP. The total loss due to attachment of electrons to MSP is given by $D^- n_e$ where D can generally be written as

$$D^\pm = \sum_Z \int_0^\infty \alpha_{e-/i^\pm}(Z, r) n_d(Z, r) dr, \quad (6.11)$$

where Z is the MSP charge number, α_{e-/i^\pm} is the attachment rate of electrons and ions, respectively and n_d is the MSP density.

Eq. 6.7 describes the production and loss of positive ions. Like electrons, positive ions are primarily formed through electron-ion pair production. They can recombine with electrons (α_{ie}) and ions (α_{ii}) forming neutral molecules. In addition, positive ions can lose their charge by transfer of electrons from dust particles.

The equilibrium density of negative ions is defined by Eq. 6.5. It comprises the production of O_2^- as primary negative ion and its depletion by atomic oxygen as well as recombination with positive ions. The production involves, beside electrons and molecular oxygen, a third body, which in this case is above all else molecular nitrogen and oxygen. The destruction of negative ions in this model is completely governed by atomic oxygen. Attachment of an oxygen atom to a molecular oxygen anion will produce an ozone molecule and release an electron. Hence, the presence of atomic oxygen will control the presence of negative ions and electrons.

The neutral and charged densities of MSPs are defined by Eqs. 6.5, 6.6 and 6.7. Attachment rates α_{e-/i^\pm} of electrons and ions on aerosols are calculated using the classical approach by *Natanson* [1960] which has been shown to be in very good agreement with quantum calculations [*Plane et al.*, 2014]. MSPs are assumed to be just singly charged since the rate coefficients for higher charging states are negligibly small. It has been shown by e.g., *Rapp and Lübken* [2001] that only particles with radii larger than ~ 8 nm are able to carry more than one elementary charge. Thus, the allowed charge states Z are -1, 0 and +1. Additionally the charging rate is calculated as a function of aerosol radii. Therefore different groups of different MSP sizes are considered in the model. Additionally, it has been stated by several authors that the charging rate for smallest particles may be further reduced by decreased electron affinity which is highly dependent on the particle's material [*Megner and Gumbel*, 2009; *Plane et al.*, 2014; *Baumann et al.*, 2013, 2015; *Asmus et al.*, 2015b]. We implemented this effect using the approach given in *Baumann et al.* [2013, 2015] who introduced a factor γ_{ch} to reduce the rate of electrons attaching to MSP. This factor is defined as

$$\gamma_{ch} = \begin{cases} 0 & \text{for } r < 0.25 \text{ nm} \\ 0.8 \text{ nm}^{-1} \cdot r - 0.2 & \text{for } 0.25 \text{ nm} \leq r \leq 1.5 \text{ nm} \\ 1 & \text{for } r > 1.5 \text{ nm} \end{cases} \quad (6.12)$$

Table 6.1: Reactions included in the model with corresponding rate coefficients and reference.

Nr.	Reaction	Rate coefficient ¹	Reference
1	$Q \rightarrow e^- + I^+$	$Q = \alpha_{ie}[I^+]^2$	see text
2	$e^- + I^+ \rightarrow \text{products}$	α_{ie}	see text
3	$e^- + O_2 + N_2 \rightarrow O_2^- + N_2$	$k_{N_2} = 1 \cdot 10^{-31}$	<i>Florescu-Mitchell and Mitchell</i> [2006]
4	$I^+ + I^- \rightarrow I + I$	$\alpha_{ii} = 6 \cdot 10^{-8}$	<i>Dieminger et al.</i> [1996]
5	$e^- + O_2 + O_2 \rightarrow O_2^- + O_2$	$k_{O_2} = 1.4 \cdot 10^{29} (300/T) \exp(-600/T)$	<i>Florescu-Mitchell and Mitchell</i> [2006]
6	$O_2^- + O \rightarrow e^- + O_3$	$k_O = 1.5 \cdot 10^{-10}$	<i>Florescu-Mitchell and Mitchell</i> [2006]
7	$e^- + MSP \rightarrow MSP^-$	$\alpha_e = \gamma_{ch} \pi r^2 \sqrt{\frac{8k_b T}{\pi m_e}} \left(1 + \sqrt{\frac{e^2}{8\pi\epsilon_0 r k_B T}} \right)$	<i>Natanson</i> [1960]; <i>Megner and Gumbel</i> [2009]; <i>Baumann et al.</i> [2015]; <i>Plane et al.</i> [2014]
8	$I^+ + MSP \rightarrow MSP^+$	$\alpha_{i+} = \pi r^2 \sqrt{\frac{8k_b T}{\pi m_{i+}}} \left(1 + \sqrt{\frac{e^2}{8\pi\epsilon_0 r k_B T}} \right)$	<i>Natanson</i> [1960]
9	$I^- + MSP \rightarrow MSP^-$	$\alpha_{i-} = \pi r^2 \sqrt{\frac{8k_b T}{\pi m_{i-}}} \left(1 + \sqrt{\frac{e^2}{8\pi\epsilon_0 r k_B T}} \right)$	<i>Natanson</i> [1960]
10	$e^- + MSP^+ \rightarrow MSP$	$\alpha_{e-} = \pi r^2 \sqrt{\frac{8k_b T}{\pi m_e}} \left(1 + \frac{e^2}{4\pi\epsilon_0 r k_B T} \right)$	<i>Natanson</i> [1960]
11	$I^+ + MSP^- \rightarrow MSP + I$	$\alpha_{I+} = \pi r^2 \sqrt{\frac{8k_b T}{\pi m_{i+}}} \left(1 + \frac{e^2}{4\pi\epsilon_0 r k_B T} \right)$	<i>Natanson</i> [1960]
12	$I^- + MSP^+ \rightarrow MSP + I$	$\alpha_{I-} = \pi r^2 \sqrt{\frac{8k_b T}{\pi m_{i-}}} \left(1 + \frac{e^2}{4\pi\epsilon_0 r k_B T} \right)$	<i>Natanson</i> [1960]
13	$I^+ + MSP^{2-} \rightarrow MSP^- + I$	$\alpha_{I+} = \pi r^2 \sqrt{\frac{8k_b T}{\pi m_{i+}}} \left(1 + \frac{2e^2}{4\pi\epsilon_0 r k_B T} \right)$	<i>Natanson</i> [1960]
14	$e^- + MSP^- \rightarrow MSP^{2-}$	$\alpha_{e-} = \pi r^2 \sqrt{\frac{8k_b T}{\pi m_e}} g^2 \exp a,$ $g = 1.62, a = \left(\frac{-e^2}{4\pi\epsilon_0 r k_B T} \right) \left(1 - \frac{1}{2g(g^2-1)} \right)$	<i>Natanson</i> [1960]

However, γ_{ch} is rather uncertain until now and varied dramatically in previous works [e.g., *Plane et al.*, 2014; *Baumann et al.*, 2015]. In addition *Plane et al.* [2014] showed by electronic structure calculations and Rice-Ramsperger-Kassel-Marcus theory that even small MSP can be charged. Meteor smoke particles are charged during nighttime via electron attachment or charge transfer from ions. Due to their high mobility relative to ions, the charging by electrons is much more efficient and hence in absence of other ionization effects such as photodetachment, the majority of MSP will be negatively charged. Since in the frame of this work only the nighttime D-region is studied photodetachment is not active in the model.

Tab. 6.1 summarizes the reactions involved in the model, their respective reaction rates and references the values and equations are taken from.

6.3 Model inputs for WADIS-2 condition

A vast number of parameters used as input in the model were measured in situ in the course of the WADIS-2 sounding rocket campaign. Neutral molecular nitrogen and oxygen were inferred from total neutral density measurements made by CONE neglecting all minor constituents (like Argon). Also thermal equilibrium was assumed for all species up to 100 km and the temperature is calculated from neutral density measurements using hydrostatic

¹Bimolecular reactions: $\text{cm}^3 \text{ molecule}^{-1} \text{ s}^{-1}$; termolecular reactions: $\text{cm}^6 \text{ molecule}^{-2} \text{ s}^{-1}$

equilibrium. Atomic oxygen densities are obtained from FIPEX and photometer measurements (see Sec. 5.1) [Eberhart *et al.*, 2015]. However, there are also parameters which have to be assumed or taken from other models. In addition to the O-density obtained from in situ measurements, data from the MSIS model are used for comparison [Picone *et al.*, 2002]. The density profiles of N_2 , O_2 and O measured by CONE, Photometer and FIPEX are shown in the left panel of Fig. 6.2. We assume a constant fraction of N_2 (79 %) and O_2 (21 %) and neglect minor trace gases. The right panel shows temperature measured by CONE. The mesopause with temperatures down to 160 K was at ~ 95 km. Additionally there is an layer at 82 km showing enhanced temperatures. Besides, as mentioned earlier those layers appear in combination with neutral air turbulence [Szewczyk *et al.*, 2013]. The neutral meteor smoke

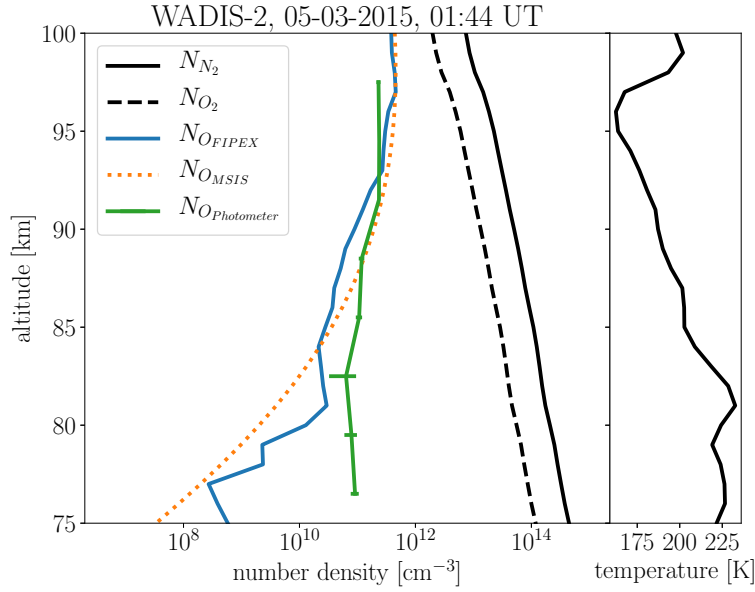


Figure 6.2: **Left:** Density profiles of N_2 (solid black), O_2 (dashed black) as well as O from different sources. The blue solid line shows FIPEX data, dashed orange are MSIS data and green solid with errorbars represent photometer data. **Right:** Temperature profile as obtained from neutral density measurements of CONE.

particle densities were obtained from the CARMA/CHEM2d model [Megner *et al.*, 2006]. The explicit data set was taken from a calculation done for day of the year (doy) 61 and is shown in Fig. 6.3. The maximum density is at small radii around 80 km. For increasing radii the density peak height decreases mainly due to gravitational sedimentation of the dust particles [Megner *et al.*, 2006]. Above 75 km MSP density rapidly vanishes for large radii. This is also apparent from the size distribution shown for 82 km in Fig. 6.4, where the histogram bars are the size bins which are spaced logarithmically to account for the log-normal like behavior of the distribution function. Input parameter which were also not measured are the electron-ion pair production rate Q and the recombination rate of electrons and positive ions α_{ie} . Both, the production rate and the electron-ion recombination rate is plotted in Fig. 6.5. Importantly, the derivation of Q by assuming that the concentration of electrons and positive ions is the same may overestimate the production rate in the altitude range where electron and positive ion densities were actually not the same. This is due to the fact that recombination of positive ions with negative ions or MSPs is slower than recombination with free electrons [Plane *et al.*, 2014].

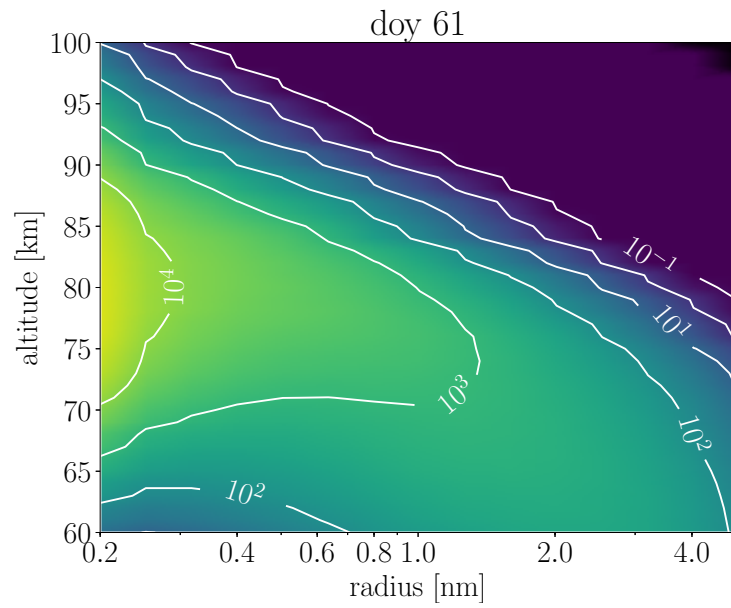


Figure 6.3: Neutral MSP density as a function of MSP radius and altitude for day-of-years 61.

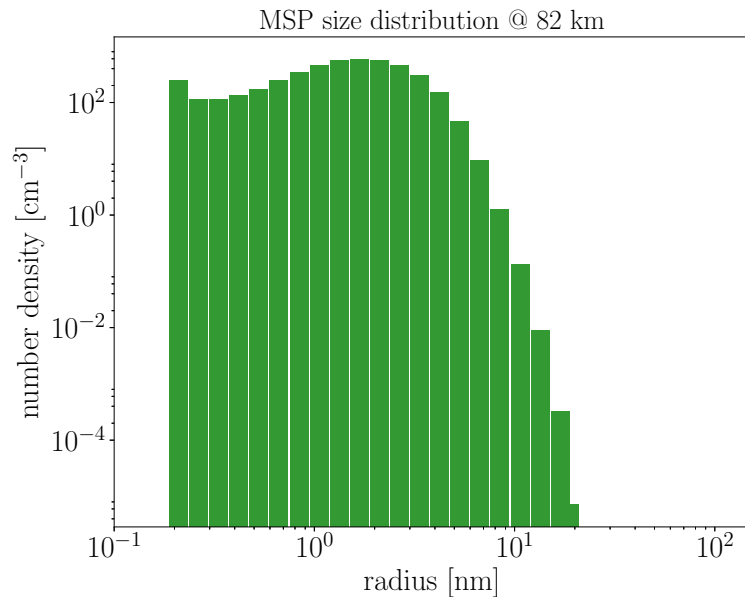


Figure 6.4: Size distribution of neutral MSP at 82 km. The biggest size bins are out of the plotting range of this figure.

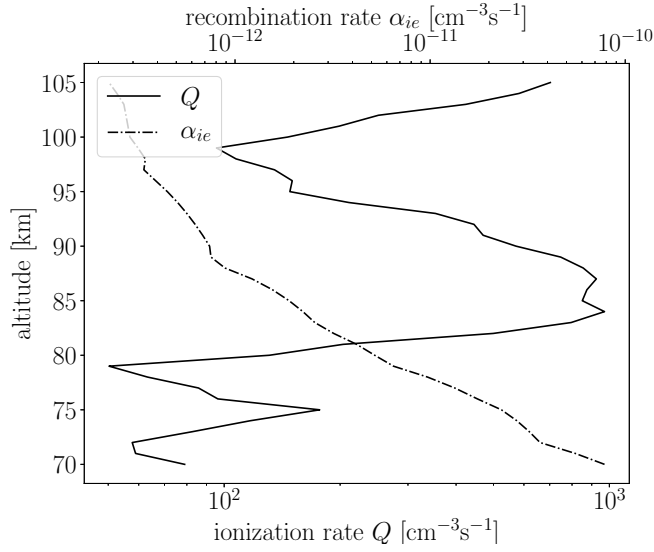


Figure 6.5: Electron-ion pair production rate Q and electron-ion recombination rate α_{ie} as a function of altitude. Q was derived using $Q \approx \alpha_{ie} n_{i^+}^2$. α_{ie} was obtained by means of an empirical model by *Friedrich et al.* [2004].

In this section results of the charging model are presented. First some light will be shed onto the influence of atomic oxygen on the charge balance with and without the inclusion of MSP. Afterwards an attempt to reproduce the dusty plasma measurements of WADIS-2 including electrons, positive ions and heavy charged particles is presented. Finally, the estimated size distribution (see Sec. 5.8) will be compared to size distributions obtained by the model.

6.4 The influence of atomic oxygen

Since atomic oxygen can have a large impact onto the presence of negative ions and hence also electrons, we will investigate that impact as a function of atomic oxygen density. For this purpose a fixed density of $n_n = 1 \times 10^{21} \text{ m}^{-3}$, a typical ionization rate of $Q = 10 \text{ cm}^3 \text{ s}^{-1}$ and temperature $T = 250 \text{ K}$ were chosen. These values are representative for an altitude of $\sim 80 \text{ km}$ which is the region of large variability of atomic oxygen [*Gumbel, 1997*]. The density of atomic oxygen was varied from $1 \times 10^{12} \text{ m}^{-3}$ to $1 \times 10^{17} \text{ m}^{-3}$. In this first step we do not account for MSPs. Thus, charged species are electrons, positive and negative ions. The results are shown in Fig. 6.6. For large concentrations of atomic oxygen the negative ion density decreases as can be seen in the right panel of Fig. 6.6. The number of negative ions increases linearly with decreasing concentration of O until the electron density is too low to produce more negative ions. *Plane et al.* [2014] stated that negative ion production is shut off when the atomic oxygen density exceeds $1 \times 10^{10} \text{ cm}^{-3}$. In Fig. 6.6 the decrease of negative ion concentration starts at a atomic oxygen density of roughly $1 \times 10^8 \text{ cm}^{-3}$. However, the density of negative ions is negligibly small around $n_O \approx 1 \times 10^{10} \text{ cm}^{-3}$ which can be interpreted as a shut off of negative ions and hence is in agreement with *Plane et al.* [2014]. Electron density does significantly decrease for atomic oxygen densities lower than $n_O \approx 1 \times 10^9 \text{ cm}^{-3}$. At the same time the positive ion density does increase reaching a plateau at $n_{i^+} \approx 1 \times 10^4 \text{ cm}^{-3}$. The reason for that is the difference between rates of electron-ion and ion-ion recombination causing a longer lifetime of the ion species. This increases the degree

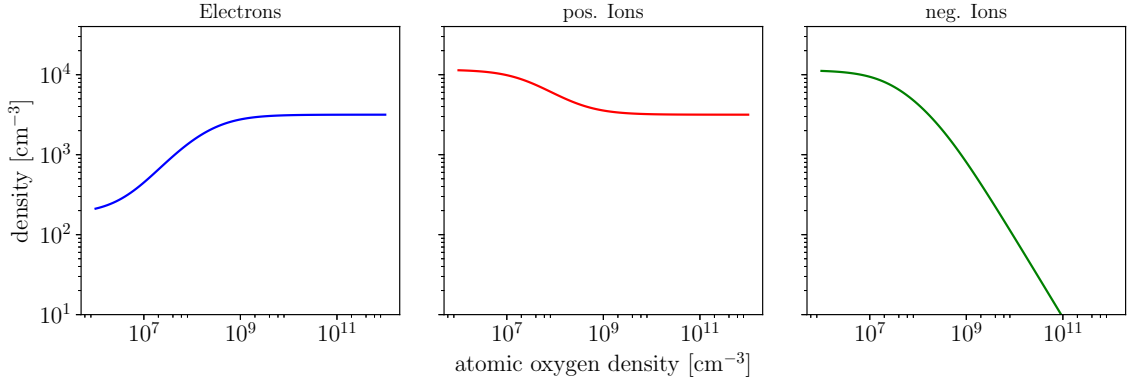


Figure 6.6: Density of plasma constituent as a function of atomic oxygen density. Left panel is for electrons, central panel for positive and the right panel for negative ions.

of ionization in the plasma in this case by approximately a factor of 3.3. The main results from the charge balance with negative ions but without MSP are:

- high densities of atomic oxygen will decrease negative ion density
- for $n_O \lesssim 1 \times 10^{10} \text{ cm}^{-3}$ negative ion density becomes negligible
- low densities of atomic oxygen ($< 1 \times 10^8 \text{ cm}^{-3}$) will decrease the density of free electrons
- low densities of atomic oxygen cause increased degree of ionization

The next step is to introduce meteor smoke particles. However, since we want to focus on the impact of atomic oxygen on the charging of the plasma constituents we assume a single size of particles for each model run. The MSP radii used are $r = \{0.4, 0.8, 1.2, 1.6\}$ nm. As in the previous case we varied the atomic oxygen density and calculated the steady state density of each component. The results of the model runs are shown in Fig. 6.7. The left column of plots in Fig. 6.7 show the densities of MSPs: negatively charged, neutral and positively charged. Electrons, positive and negative ions behave similar to the case without MSP. The main difference here is that most of the electrons are either on the MSPs as can be seen in the upper left plot or on the negative ions. However, as in the previous model version without MSP, negative ions become important for atomic oxygen densities below $\sim 1 \times 10^9 \text{ cm}^{-3}$ only. Below O densities of around $1 \times 10^8 \text{ cm}^{-3}$ negative ion density start to exceed the negative MSP density. The change of the neutral MSP density is small. Positively charged MSP do not play a significant role in this model run. However, there is an increase of N_d^+ at low atomic oxygen densities. The difference between the model runs using different particle radii is most obvious in the densities of negative MSP, positive MSP, electrons and negative ions. While the density of large negative MSP is less decreased at low atomic oxygen densities, the electron density shows an opposite behavior. The largest absolute difference between the electron densities of the different model runs is observed at atomic oxygen densities larger than $1 \times 10^8 \text{ cm}^{-3}$. The density of negative ions is reduced as MSP radii become larger. Last but not least, the density of positive MSP increases at atomic oxygen densities lower than $1 \times 10^8 \text{ cm}^{-3}$. The difference between the model runs can be attributed to the size dependence of the charging rate of MSPs. Large particles are more likely to catch

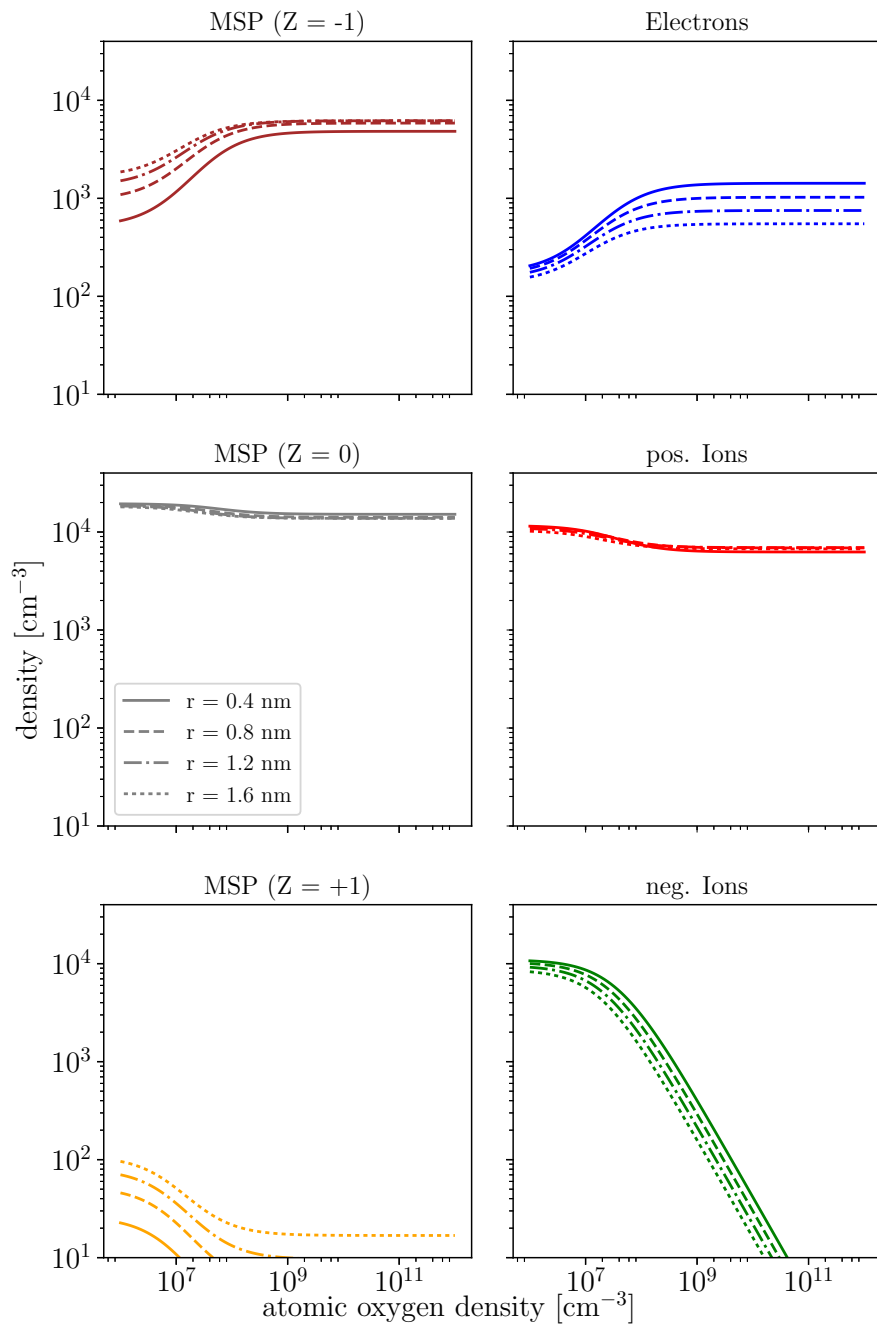


Figure 6.7: Density of plasma constituent as a function of atomic oxygen at 80 km. The line styles indicate calculations for different MSP radii. The three plots in the left column show densities of negatively charged, neutral and positively charged MSP. Electrons, positive and negative ions are shown in the plots on the right hand side of the figure.

an electron relative to small ones. One conclusion here is that the density of large charged MSPs is less influenced by the presence of atomic oxygen. Consequently, atomic oxygen does have an impact on the size distribution of charged MSP, meaning that in the absence of atomic oxygen there are more large charged MSP relative to small MSP in contrast to the presence of high atomic oxygen concentrations. Hence, since atomic oxygen is usually absent at altitudes below ~ 80 km in the night-time D-region there are more large charged particles. However, this effect is superposed with e.g., the changing of neutral MSP size distribution in vertical direction. The main points of the influence of atomic oxygen onto MSP density can be summarized as follows

- the general behavior of electron, positive and negative ion densities is the same as without MSPs
- MSPs are primarily charged by electrons and decreasing electron density yields decreasing charged MSP density
- large MSPs are charged more efficiently, density of large negatively charged MSPs is less reduced at low O densities
- atomic oxygen has an effect on the charged MSP size distribution \rightarrow less O means fewer small charged MSP relative to large ones

In the next section the model is fed with inputs given by data obtained during the WADIS-2 sounding rocket campaign or from models run for the WADIS-2 conditions (see Sec. 6.3).

6.5 Model results for WADIS-2

In this section the model results are compared to measured values of dusty plasma components. The in situ data are described in Sec. 5.4. As some input parameters are given by other models, we use these to adjust the model results to satisfy the in situ measurements. However, to have a reference case to compare with, a model run with standard inputs was performed. These standard inputs are given in Tab. 6.2. The result of the reference model run is shown in Fig. 6.8. The model results (dashed lines) are shown together with the in situ measurements (solid lines). First of all we see that the positive ion density (green) is well reproduced by the model above 85 km. Below that height the density is larger than the measured one. The model electron density (dashed blue) is larger than the measured all below 103 km. For comparing the derived negatively charged MSP density with the measured values the model result for negative MSP is weighted by the PD detection efficiency (see Sec. 4.1.1). This gives the MSP density detectable by the PD (red dashed) which then is compared with the actual measured density (black solid). At around 80 km calculated and measured density of negatively charged MSPs are in good agreement. However, above that height the model results are much lower. One main reason for the differences between model and measurements can be attributed to the absence of MSP in the model at high altitudes. This can be easily tested by adjusting the input neutral MSP density made in the next section.

6.5.1 Adjusting model inputs to reproduce WADIS-2 measurements

The input neutral MSP density is given for discrete size ranges (see Fig. 6.4). The density peak height in the smallest size bin is highly dependent on the ablation peak height. This was shown by model sensitivity studies by *Megner et al.* [2006]. Importantly, the ablation peak height is still not well known as can be seen from the study by *Carrillo-Sánchez et al.*

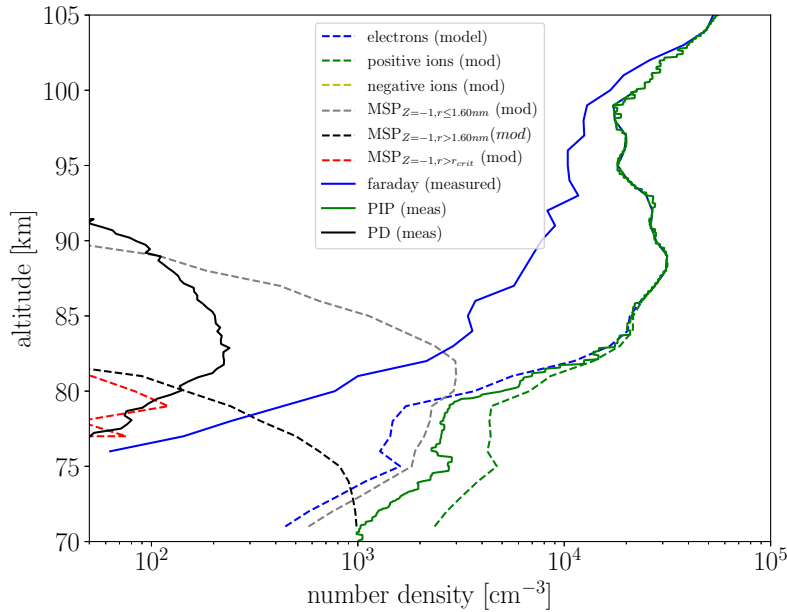


Figure 6.8: Case 0: In-situ measurements and reference model results for WADIS-2. In-situ measurements are given by solid lines, model results are indicated by dashed lines. Blue is electron, green positive ion, yellow negative ion, gray and black are negative charged MSP density, whereas the gray dashed line are all MSP with radii smaller than 1.6 nm and the black dashed line are all particles greater than that. The solid black line is the density of all MSP seen by the PD. The red dashed line is the density of negatively charged MSP seen by the PD as inferred from the model results.

[2015]. By shifting the initial neutral MSP 12.5 km upwards we assume that a change in the ablation peak height will equally shift all size bins of the neutral MSP. According to the results found by *Megner et al.* [2006] this is a good approximation between 73 and 93 km. The elevated neutral MSP density input is shown in Fig. 6.9. The new density peak height in the smallest size bin can be found between 90 and 95 km. All other parameters given in Tab. 6.2 are the same allowing for an easy comparison to the reference model run. The results of the adjusted density peak height model run are shown in Fig. 6.10. Let us now compare the model run with the shifted neutral MSP density input to the reference case given in Fig. 6.8. The changes in electron and positive ion density are relatively small. The electron density decreases while positive ion density increases. The major difference to the reference case is the estimated charged MSP density seen by the PD (red dashed) which increased dramatically. The calculated peak density at 82 km is a factor two larger than the measured value of $224 e \text{ cm}^{-3}$. Nevertheless, the shape of the measured charged particle layer is well reproduced. As the derived electron density is still not in agreement with the measurements there is still a process missing that efficiently reduces electron density. By now both model runs, reference and shifted MSP density were performed using reduced sticking coefficients for the smallest MSP. However, as these coefficients are highly uncertain we will set them to unity for the next model run allowing more electrons to be attached to MSP. The results of this model run are shown in Fig. 6.11.

In contrast to the previous model run the electron density is now more reduced since electrons are attached to the smaller MSP. This results in a larger density difference between

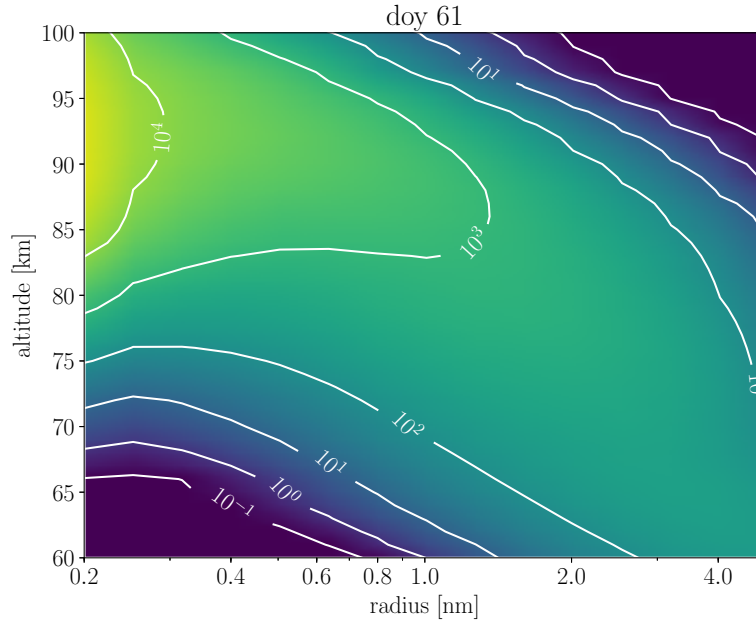


Figure 6.9: Upward shifted (+12.5 km) neutral MSP density as a function of MSP radius and altitude for day 61.

electrons and positive ions which is in agreement with the measurements. However, the absolute value of this difference is not reproduced in every altitude. There are two apparent regions where the absolute difference between electrons and positive ions in the model is less than seen by measurements. One region is between 80 km to 95 km and the other is below 77 km. The latter is a region where typically negative ions play an important role. However, using the FIPEX oxygen profile in the model prohibits production of a significant amount of negative ions. Nevertheless, since neutral MSP density decreases with decreasing altitude there are too many free electrons in the model. This is an indication that either the atomic oxygen density in this altitude range is too large or that the input neutral MSP density is too low. The latter case can be excluded since we have a larger MSP density in the reference case and the electron density remains too large. Since the atomic oxygen density by the MSIS model (see Fig. 6.2) reveals lower densities below 80 km than the in situ measurements we used this O-profile in the next model run. The results of this model run are shown in Fig. 6.12.

As the atomic oxygen from MSIS model is more than 2 orders of magnitude lower below 80 km, the negative ion density increases dramatically in this region. Moreover, the absolute value of negative and positive ions is overestimated by one order of magnitude at 71 km. The density of free electrons is also too large at those altitudes indicating that the ionization rate have to be lower to reproduce the measurements.

In the last step, we will adjust the neutral MSP vertical shift and the ionization rate in order to obtain the best fit of model results to the in situ measurements. The ionization rate is adjusted iteratively until the measured electron and positive ion density is reproduced by the model. The resulting ionization rate is shown in Fig. 6.13 (black line). In contrast to the original Q (blue line) the adjusted profile has a more exponential behavior. Additionally, as a lower ionization limit an Q -profile obtained from $Q = \alpha_{ie} n_e^2$ is shown in Fig. 6.13 (orange line) which reveals even lower ionization rates as the adjusted Q -profile. Earlier calculations

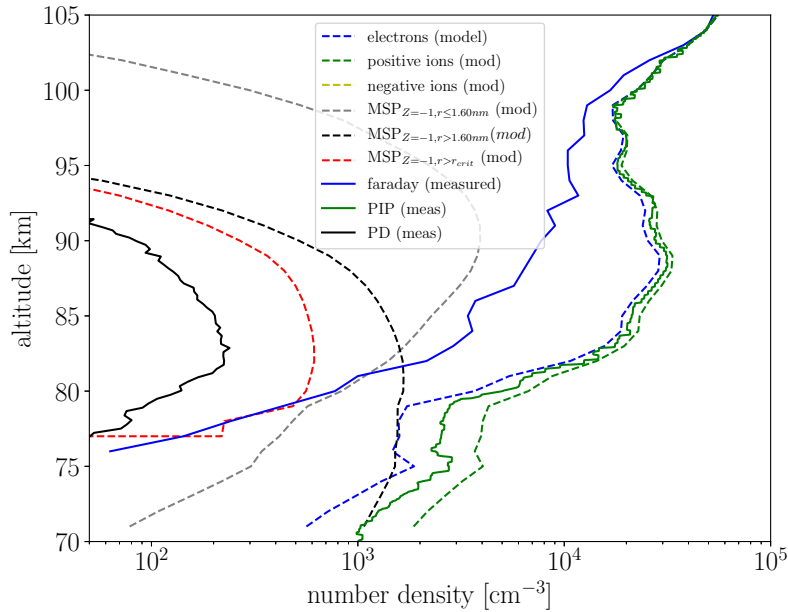


Figure 6.10: Case 1 : Same as Fig. 6.8 but for shifted neutral MSP density input for WADIS-2.

of Q by e.g., *Gumbel et al.* [2003] showed comparable results. Notably, these calculations were made for twilight and daytime conditions.

To satisfy the in situ dusty plasma measurements also the input neutral MSP density was again shifted. In this case a vertical shift of 8.5 km for all size bins was used. This shift results in a peak density height for the smallest size bin of about ~ 88 km. The measured atomic iron layer shown in Fig. 5.11 indicates a meteor ablation peak height at the same altitude supporting the shift of the neutral MSP. The best fitting model result can be seen in Fig. 6.14. Electron and positive ion density from the charging model are in good agreement with the in situ measurements. In addition, the obtained density of charged MSP expected to be seen by the PD (red dashed line) overestimates the actual measured dust density (black solid line) by a factor of ~ 2 . However, this difference is smaller than the estimated uncertainty of the model. Note, the full detection efficiency consists of the probability of particles reaching the PD outer grid/entrance and particles reaching the PD electrode. The latter was just calculated for 82 km. As a rough estimate the critical radius as a function of altitude was calculated using the critical radius given in Fig. 4.8 and multiply the dust density of particle larger than r_{crit} with the probability of particles reaching the PD electrode at 82 km. Importantly, negative ions are the most important negative plasma constituents below 75 km which is in agreement with earlier findings [*Baumann et al.*, 2015]. The rough estimate of negative MSP seen by the PD from model (red dashed) endorses the measurement (black solid). Note, that this assessment underestimates detectable particle densities above 82 km and overestimates it below that height.

In summary the simple model calculations show that:

- In order to reproduce the measured data the ablation peak height for meteoroids was set to approximately 88 km which is in agreement with meteor input derived from radar meteor head echoes [*Carrillo-Sánchez et al.*, 2015].

MSP z-shift: 12.5 km, MSP dens * 1.0, Sticking Coeff: 1
 O profile: FIPEN, Production rate: $Q = \alpha_{ie} \cdot N_i^2$

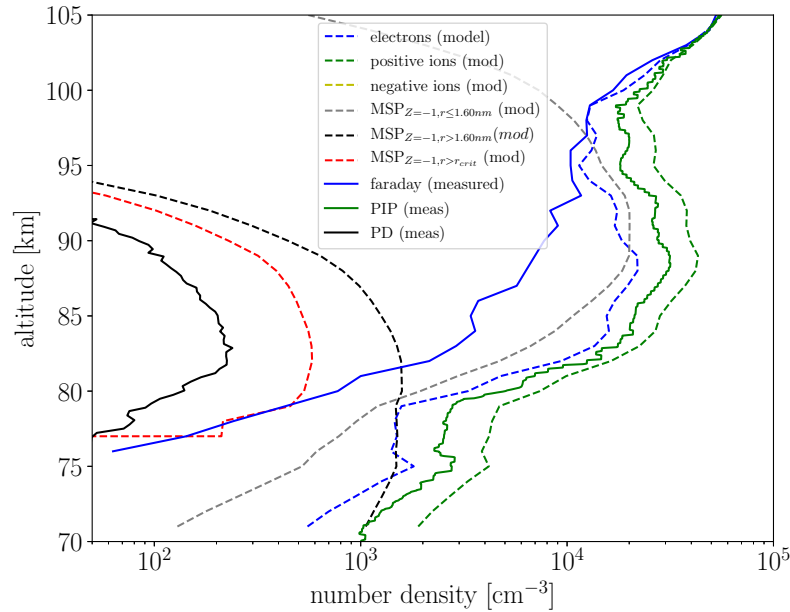


Figure 6.11: Case 2: Same as Fig. 6.8 but for shifted neutral MSP density input as well as electron sticking coefficient set to unity for WADIS-2.

- In order to reproduce the low electron densities below 80 km atomic oxygen density has to be smaller than $1 \times 10^9 \text{ cm}^{-3}$
- Derivation of the production rate Q from positive ion density yields too large electron densities and therefore has to be decreased/adjusted
- Measured charged MSP layer can successfully be reproduced by combining model results with results of the aerodynamic/electrostatic simulations.

6.5.2 Charged particle size distribution at 82 km

The charging model calculates densities of charged MSPs for every size bin which can be used to obtain a charged particle size distribution. This was done for each model run described in the previous paragraph. In Sec. 5.8 a size distribution for charged MSP was estimated from the in situ measurements at 82 km and thus can be compared to the model results. Therefore, the size distribution has to be integrated over each size bin of the model to yield densities of each size bin. Subsequently, the distribution of all model cases are compared. Tab. 6.2 gives an overview of the input parameters for all model cases. The results of all cases are shown in Fig. 6.15. The distributions are shown as a function of particle radius. Notably, the size distribution obtained from the charging model in the reference case 0 has a log-normal shape (blue line). Moreover, the mean radius of the distribution given by the dashed blue line agrees very well with the mean of the distribution which is described in Sec. 5.8.

However, the quantitative comparison shows, that the model produces too few charged MSPs with respect to the in situ result. Scaling the neutral MSP density by a factor of approximately 3.5 reproduces the distribution estimated from in situ measurements. However, the reference case does not reproduce the in situ densities. In case 1 which is shown by the orange line in Fig. 6.15 the neutral MSP input was shifted by 12.5 km. This also have

MSP z-shift: 12.5 km, MSP dens * 1.0, Sticking Coeff: 1
 O profile: MSIS, Production rate: $Q = \sigma_{te} \cdot N_e^2$

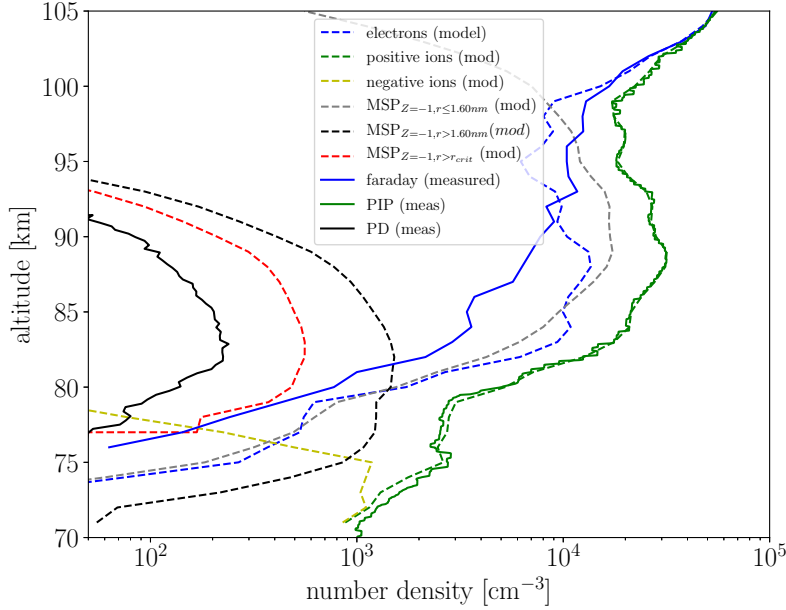


Figure 6.12: Case 3: Same as Fig. 6.8 but for MSIS-O profile, shifted neutral MSP density input as well as electron sticking coefficient set to unity for WADIS-2.

Table 6.2: Input keywords and values for all model case.

Parameter	case 0 (reference)	case 1	case 2	case 3	case 4
O-profile	FIPEX	FIPEX	FIPEX	MSIS	MSIS
neutral MSP vertical shift	0 km	12.5 km	12.5 km	12.5 km	8.5 km
sticking coefficient γ_{ch}	Eq. 6.12	Eq. 6.12	1	1	1
ionization profile	Eq. 6.10	Eq. 6.10	Eq. 6.10	Eq. 6.10	adjusted

an impact on the size distribution. As one can see from Fig. 6.15 the mean value of the distribution is shifted to larger particles which is caused by the absence of small MSP.

The best agreement with measured plasma densities was achieved by neglecting decreasing of the sticking coefficient of electrons. Increased charging of the smallest MSP however, has a dramatic impact on the size distribution of negatively charged particles. This can be seen from the case 2 green curve in Fig. 6.15 where the density increases strongly at smallest radii. This effect leaves the size distribution with two maxima, one at the smallest size bin and one at approximately 1.2 nm. However, the mean particle radius (green dashed line) is larger than the one found from in situ measurement. Moreover, the derived plasma densities of the model do not reproduce the measurements.

Finally, the size distribution found at 82 km for case 3, the model run which agrees best with the in situ results is shown by the red curve in Fig. 6.15. The peak at smallest radii is even larger than in case 2. The absolute value of the second peak at larger radii remains the same compared to the previous case. However, the peak is shifted to smaller radii of approximately 1 nm.

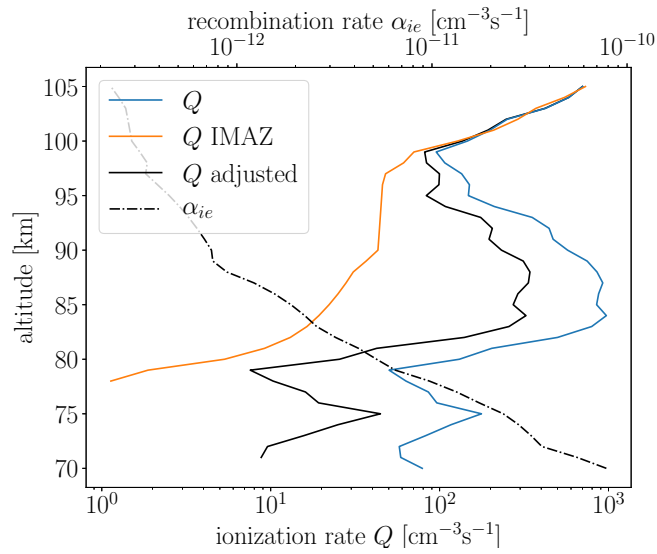


Figure 6.13: Ionization rate profiles as a function of altitude obtained from positive ion density (blue line), adjusted positive ion density (black line) and from electron density. The dashed black line shows the dissociative recombination rate for electrons and ions.

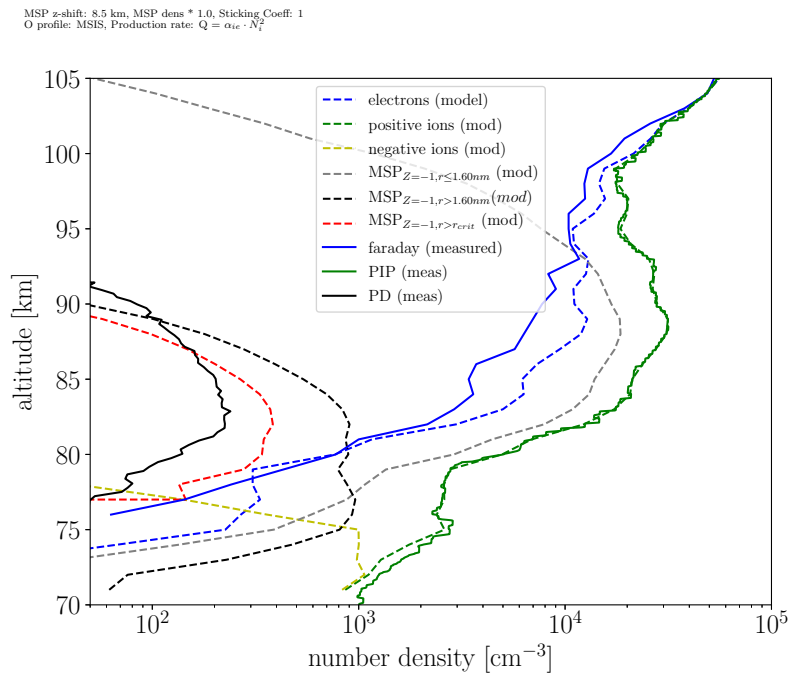


Figure 6.14: Case 4: Same as Fig. 6.8 but for shifted neutral MSP density input, adjusted Q as well as electron sticking coefficient set to unity for WADIS-2.

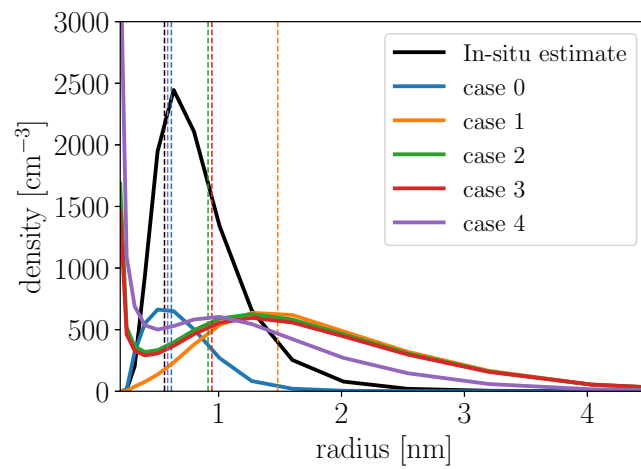


Figure 6.15: Size distributions of the in situ estimate described in Sec. 5.8 (black line), the reference case 0 (blue line), case 1 with upward shifted neutral MSP density (orange line), case 2 with upward shifted neutral MSP density and electron sticking coefficient set to one for all sizes (green curve), case 3 same as case 2 but with O-density from MSIS and the best fit case 3 with additionally adjusted Q and neutral MSP density shifted by 8.5 km (red curve). The dashed lines mark the mean particle radii of the corresponding distribution having the same colors.

Chapter 7

Discussion

In this chapter the results of the WADIS-2 sounding rocket campaign are discussed in context of the up-to-date knowledge about this field. In the first step the charge balance during WADIS-2 will be discussed. It will be followed by the discussion of small scale structures and mean particle radius. Afterwards particle size distributions are discussed followed by size dependent layering and finally the role of atomic oxygen.

7.1 Charge balance

In the absence of Sun light the presence of aerosols can lead to electron density depletion as the electrons are likely to attach to the heavy particles [Brattli *et al.*, 2009; Rapp *et al.*, 2011; Baumann *et al.*, 2013, 2015]. Since the mobility of electrons is ~ 3 orders of magnitude larger than the mobility of ions the attachment of electrons to aerosols is more efficient and can cause huge differences between electron and positive ion densities [Friedrich *et al.*, 2011]. As shown in Fig. 5.10 this is also seen in the WADIS-2 plasma measurements. The density profiles of electrons and positive ions reveal an increasing difference below 104 km which indicates the presence of charged MSPs is necessary to satisfy quasi neutrality. During WADIS-2 the PD measurements indicate the presence of heavy, predominately negatively charged MSPs at least between 92 and 75 km which can explain the discrepancy qualitatively. By the difference between electron and positive ion density we found that the amount of charged MSPs can by far exceed the amount of free electrons (~ 1 order of magnitude). Electron depletions found by Friedrich *et al.* [2012] show lower values.

Moreover, there are also negative ions which besides charged MSPs are playing an important role in the D-region charge balance but they were not measured during WADIS-2 [e.g., Baumann *et al.*, 2013, 2015; Asmus *et al.*, 2015b]. Model results showed that negative ion density (predominantly NO_3^- and O_2^- at night around 80 km) is thought to rapidly decrease above 80 km during night time due to increase of atomic oxygen densities [Thomas and Bowman, 1985; Plane *et al.*, 2014; Baumann *et al.*, 2015]. This was also confirmed by the results of the simple charging model presented in Sec. 6.2 and the measured O-density (see Fig. 6.2). The charged particle density measured by the PD is limited due to aerodynamics and therefore do not quantitatively explain the difference between electrons and positive ions. Nevertheless in this work it was shown that the instrumental limitations of the PD allows only qualitatively measurements of charged MSPs in all altitude ranges. Aerodynamical effects dominate below ~ 80 km whereas electrostatic filtering are important above. By means of the charging model and the results of the combined aerodynamical and electrostatic simulations we were able to explain the remaining charge difference between positive and negative

species. The instrumental limitations determine the observed density profile. Above 82 km the decrease of measured dust density is due to the decrease of MSP-density with sizes ≥ 1 nm which are shielded by the PD grids potential. Aerodynamic filtering becomes more important below 82 km and limits the particle detection to approximately 75 km. Moreover, the charge density seen by the PD as estimated from the model agrees well with the actual in situ measurements. In contrast to current model results by e.g., *Megner et al.* [2008] and *Plane et al.* [2014] the findings from the charging model presented in this work indicates a higher meteor ablation peak height around 90 km which supports meteor input function deduced from radar measurements [*Carrillo-Sánchez et al.*, 2015].

Summarizing, we found that a large number of negatively charged MSP were present between 75 and ~ 100 km which exceeded the number of electrons by up to one order of magnitude. The electron depletion starting near 100 km seen during WADIS-2 was not seen in earlier flights indicating a large variability of the number of charged MSPs and their height distribution.

7.2 Small scale structures and mean particle radius

As the motion of plasma constituents in the D-region is dominated by collision with neutrals, neutral air turbulence creates small-scale structures in all plasma species, including charged aerosols, electrons, and ions [e.g., *Rapp and Lübken*, 2004]. The degree of ionization is rather low and the influence of motions due to electrostatic fields can be neglected. Thus, the plasma components are passive tracers and reproduce the neutral gas movement. Electrons, as part of the dusty plasma follow the same motion as they are electrostatically coupled to positive ions. This is also seen in the measurements of electrons and neutral gas density fluctuations, showing structures at the same altitude range in both, neutrals and electrons. Interestingly, electrons are structured down to smaller scales than the neutrals (see Fig. 5.15). In summer this is known to be the underlying process for the polar mesosphere summer echoes (PMSE) as huge ice particles are part of the dusty plasma [e.g., *Cho et al.*, 1992; *Rapp and Lübken*, 2004]. The extension of electron density fluctuation power spectra to smaller spatial scales can be described by an enhanced Schmidt number $Sc = \frac{\nu}{D}$, i.e. the ratio of kinematic viscosity of air ν , to diffusivity D , of electrons. In the presence of large charged particles the diffusivity of electrons decrease and causes the Schmidt number to increase significantly. For summer, in the presence of large ice particles typical values for Sc found in PMSE are several hundreds on average and can often be several thousands [*Lübken et al.*, 1994; *Li et al.*, 2010; *Rapp et al.*, 2011]. Moreover, the fluctuations of electron and neutral density are anti correlated as previously seen by *Lübken et al.* [1994]. In analogy, this phenomenon has been investigated comparing neutral and positive ion density fluctuations by *Fritts and Thrane* [1990] and *Thrane et al.* [1994]. In case of neutral and positive ion density fluctuations the anti correlation is linked to turbulent processes, whereas correlation is due to chemical processes [*Fritts and Thrane*, 1990].

During winter conditions there are no ice particles in the MLT-region. However, it was proposed that polar mesosphere winter echoes (PMWE) are formed by the same effect but involving the smaller MSP [e.g., *Kavanagh et al.*, 2006; *Lübken et al.*, 2007; *Kero et al.*, 2008; *La Hoz and Havnes*, 2008; *Havnes and Kassa*, 2009; *Havnes et al.*, 2011; *Strelnikova and Rapp*, 2013; *Stebel et al.*, 2004; *Belova et al.*, 2008]. Importantly, this has not been confirmed by direct measurements yet and it has been shown that some echoes can be explained by only neutral turbulence acting on the plasma [*Lübken et al.*, 2007]. The ice particles in summer can grow to large aerosols with radii of tens to hundred nanometers by accumulating water molecules [e.g., *Berger and von Zahn*, 2002; *Bailey et al.*, 2015]. MSPs on the other hand which are present

all year round reveal much smaller sizes down to sub-nanometer [e.g., *Strelnikova et al.*, 2007; *Megner et al.*, 2008; *Kero et al.*, 2008; *La Hoz and Havnes*, 2008; *Belova et al.*, 2008; *Havnes and Kassa*, 2009; *Fentzke et al.*, 2009; *Robertson et al.*, 2014; *Rapp et al.*, 2010, 2012; *Strelnikov et al.*, 2012]. Thus, the effect of reducing the electron diffusivity and hence increasing Sc should be much smaller in winter since it is connected to the radius by $Sc \sim r^2$ [*Lübken et al.*, 1998]. In this work Schmidt numbers were calculated for the first time for charged MSPs in night time winter conditions. The derived Schmidt numbers have small values between 1 and 6 above 78 km. Nevertheless, there is an effect of charged MSPs on electron diffusivity since values of Sc were found to be considerably larger than 1. The conversion of Schmidt number to mean particle radius using the classical theory of *Cho et al.* [1992] showed that particles in the polarization interaction regime are rather small i.e. in the size range of molecules. Whether or not the diffusivity of electrons in the polarization interaction regime is dominated by MSPs can not be ascertained. Thus, the conversion of Schmidt number to mean charged particle radius is not applicable for Schmidt numbers smaller than Sc_{tr} , i.e. in the polarization interaction regime. The lower limit of the possible derivation of particle size from Schmidt number is therefore the transition between hard sphere and polarization interaction which is given by the transition radius r_{tr} and the corresponding Sc_{tr} . For the winter time mesopause region we found this limit to be $Sc_{tr} \approx 3$.

Summarizing one can say that electron density fluctuations were found to be structured to smaller scales as neutral density fluctuations. This results in Schmidt numbers larger than one indicating an impact of charged MSPs onto the electrons diffusivity. For winter conditions this was found for the first time. In addition, Schmidt numbers can be converted to mean particle radii down to a transition limit. This limit was found to be $Sc_{tr} \approx 3$.

7.3 Charged particle size distribution

Incoming meteorites deposit their material in the mesosphere by ablation and MSPs are formed from the remnants of those meteorites [e.g., *Rosinski and Snow*, 1961; *Hunten et al.*, 1980]. The growth of those particles is thought to be initiated by homogeneous nucleation and governed by coagulation processes which yield an altitude dependent size distribution [e.g., *Hunten et al.*, 1980; *Megner et al.*, 2006]. Since measuring neutral MSP properties is rather complicated most in situ and remote sensing techniques use the charged state of MSPs. Rocket borne measurements were presented by e.g., *Rapp et al.* [2010, 2012]; *Strelnikov et al.* [2012]; *Robertson et al.* [2014] but also ground based radar techniques were used to obtain MSP properties [e.g., *Rapp et al.*, 2007; *Strelnikova et al.*, 2007; *Fentzke et al.*, 2009]. Radar backscatter depends on changes in the refractive index of the atmosphere which in the MLT region is solely determined by electron density [*Skolnik*, 2008]. Thus, obtaining particle properties from radar backscatter is only possible if the particles alter the electron density e.g., by decreasing the electron diffusion. The connection of radar echoes and particles have also been studied using active radar experiments that heat free electrons at MLT heights by HF-waves emitted from the ground and, in parallel examine the behavior of PMWE in VHF band [*Kero et al.*, 2008; *Havnes and Kassa*, 2009; *La Hoz and Havnes*, 2008; *Belova et al.*, 2008]. Moreover, it was shown that MSPs with radii of less than 1 nm exist in the winter mesosphere by remote sensing and in situ experiments [e.g., *Strelnikova et al.*, 2007; *Fentzke et al.*, 2009; *Robertson et al.*, 2014]. Charged particles, i.e. their size play a key role in the diffusivity of electrons in a dusty plasma and hence have to be studied rigorously in terms of radar backscatter theory. The magnitude of this influence is mainly driven by the size of the particles. However, the determination of particle sizes by direct measurements are rare and rather coarse [*Robertson et al.*, 2014].

In Sec. 5.8 it was shown that by means of mean radius obtained from Sc (see Sec. 5.6) and the integrated density of charged particles down to the detection limit of the PD one can derive a size distribution of charged MSPs. This method is limited to distributions which are described by the integrated charged particle density, a mean radius and a distribution width. The width was derived in an iterative process. The main assumption here was that the charged particles are log-normal distributed. This estimate is justified by mainly two conditions. First of all, the charging rate of aerosols increase proportional to their cross section with r^2 [Natanson, 1960]. Secondly, the number density of all MSPs decreases with size as has been shown by model calculations [Megner *et al.*, 2006]. Thus, the size distribution of charged MSPs $f(r)$ is a product of the charging probability and the neutral dust size distribution. Moreover, the probability of electrons to stick to MSPs is also depending on its material. This so-called sticking factor is not well known and introduces a large uncertainty in the amount of charged particles in the sub nanometer size regime [e.g., Plane *et al.*, 2014].

The resulting size distribution reveals particle radii in the range of 0.5 nm to 1.5 nm which is in agreement with other in situ and remote findings [Strelnikova *et al.*, 2007; Fentzke *et al.*, 2009, 2012; Robertson *et al.*, 2014]. Comparing the size distribution regardless of charging to the neutral MSP size distribution from Megner *et al.* [2006] at 90 km one finds that the number concentration of particles around the mean particle radius $r = 0.56$ nm is of the same order of magnitude [Megner *et al.*, 2006, Fig. 2]. Since it is assumed that the smallest particles are less efficiently charged the presented results imply that compared to the model results by Megner *et al.* [2006] the amount of neutral MSP had to be larger to explain the observed density of charged MSP. This differences, however, is in the uncertainties of the model due to poorly known parameters such as e.g., coagulation rate, eddy diffusion and meteoric input [Megner *et al.*, 2006].

Aerosols in the MLT region during night time are charged by attachment of electrons or charge transfer from ions [e.g., Baumann *et al.*, 2015; Asmus *et al.*, 2015b]. However, previous model results show that not the whole MSP ensemble is charged [Megner and Gumbel, 2009; Plane *et al.*, 2014; Baumann *et al.*, 2015; Asmus *et al.*, 2015b]. The attachment of electrons to the smallest particles is thought to depend on the structure of the particles since they are consisting of only a view atoms which have different electron affinities [Plane *et al.*, 2014]. An olivine (FeMgSiO_4) particle for example has four oxygen atoms and might in the first stage of growth not contain a silicon atom which has a large electron affinity. This would decrease the electron attachment rate significantly according to Plane *et al.* [2014]. Megner and Gumbel [2009] stated that not the whole MSP population is charged, otherwise one would expect large electron density depletions which are not observed. However, in contrast to that a huge difference between electrons and positive ions was observed during WADIS-2 indicating such a large electron depletion. Comparably strong depletions were seen during the night time flight of the CHAMPS campaign in October 2011 [Friedrich *et al.*, 2012; Robertson *et al.*, 2014; Asmus *et al.*, 2015b]. The variability of electron depletion observed during night time in winter was found to be very large [Friedrich *et al.*, 2012; Baumann *et al.*, 2013]. However, the reason for this variability is not known so far. Electron depletions which are of a large vertical extent may only be recognized if positive ion density is measured simultaneously. Due to the large uncertainties in the charging process of the smallest MSP the estimated size distribution from the in situ measurements was compared to the results of the model. In Sec. 6.5.2 the size distributions which were calculated using the results of the simple charging model are presented. The best agreement with the size distribution estimated from the measurements was found by using the original neutral MSP input and the sticking coefficient γ_{ch} from Baumann *et al.* [2013, 2015]. However, the charging model does not reproduce the measured

electron and positive ion densities using these input parameters. The derived charged MSP densities are too small to explain the difference between measured electron and positive ion density. Assuming that the input neutral MSP size distribution is valid, more of the smallest particles had to be charged which implies that the charged particle size distribution has a more sophisticated shape. Hence, a second model run was performed assuming that once an electron attaches to a MSP the probability that it remains on the MSP γ_{ch} is one. This implies that there are charged MSP of every size. However, the amount of charged MSPs is still depending on the particle size. It turns out, that by allowing also the smallest MSP to be charged the model results are in a better agreement with the in situ measurements of plasma densities. The resulting size distribution of charged MSP from the model has a mean radius 0.59 nm which is in good agreement with the charged particle mean radius obtained from the measured Schmidt number. Both, the size distribution from in situ measurements and charging model are in agreement with the measured charged MSP densities at 82 km. However, only the charging model is able to reproduce the plasma densities in all altitudes. Reproducing the size distribution estimated by in situ measurements with the model yield electron and positive ion densities which are not in agreement with the measurements. Thus, the approach that the charged particle size distribution follows a simple log-normal shape may not be appropriate for the WADIS-2 conditions as also noted in *Asmus et al.* [2017].

We now discuss the results found in this work in comparison to measurements of a rocket-borne mass spectrometer (MASS) described by *Knappmiller et al.* [2008]; *Robertson et al.* [2014]. These measurements were obtained from the night time launch during the CHAMPS (Charge And Mass of meteoric smoke ParticleS) sounding rocket campaign conducted in October 2011 [*Robertson et al.*, 2014]. MASS had five channels which are designated for detecting different particle masses (size bins). For comparison the size distributions derived in this work are scaled to the size bins of MASS. This is achieved by integrating Eq. 5.2 numerically and calculating the sum of the densities derived by the model for each MASS size bin. The result is shown in Fig. 7.1. In the upper panel one can see that the absolute amount of charged MSPs measured by MASS is lower compared to the WADIS-2 results. The differences between electrons and ions for CHAMPS at ~ 82 km was found to be comparably large as seen during WADIS-2 ($\sim 10\,000\ e\ cm^{-3}$) [*Robertson et al.*, 2014; *Asmus et al.*, 2015b]. Obviously the MASS instrument did not measured the complete ensemble of charged MSPs. This is most likely due to aerodynamical filtering of the MASS instrument. To compare the shape of the distributions the charged particle density of every size bin is normalized to the density of all charged MSPs which is shown in the lower panel of Fig. 7.1. Over 60% of the charged particles are in the mass range between 0 to 500 amu for the distribution of the charging model. For CHAMPS this is around 30% and 7% for the distribution estimated from WADIS-2 measurements. Smallest particles (<500 amu) can be charged as shown by the CHAMPS in situ measurements. The findings of this work support the thesis that even smallest particles are negatively charged if large electron depletions are present during night time above 80 km. As stated by *Plane et al.* [2014] the ability of a small MSP to keep an electron once the electron hits the MSP is depending on the MSP's electron affinity. Hence the model results imply that the MSPs had high electron affinities. However, the charge state of the smallest MSPs still introduce the largest uncertainty in the derivation of a size distribution as it determines the shape of the distribution. Thus there is a need of further investigation of the charging of sub-nanometer sized MSPs.

Concluding the discussion of charged particle size distributions one can say that it is possible to derive a distribution using independent in situ measurements under the assumption of a certain shape of the distribution with one maximum. The model calculation show that the uncertainty of charging processes i.e. the so-called sticking factor of MSPs smaller than

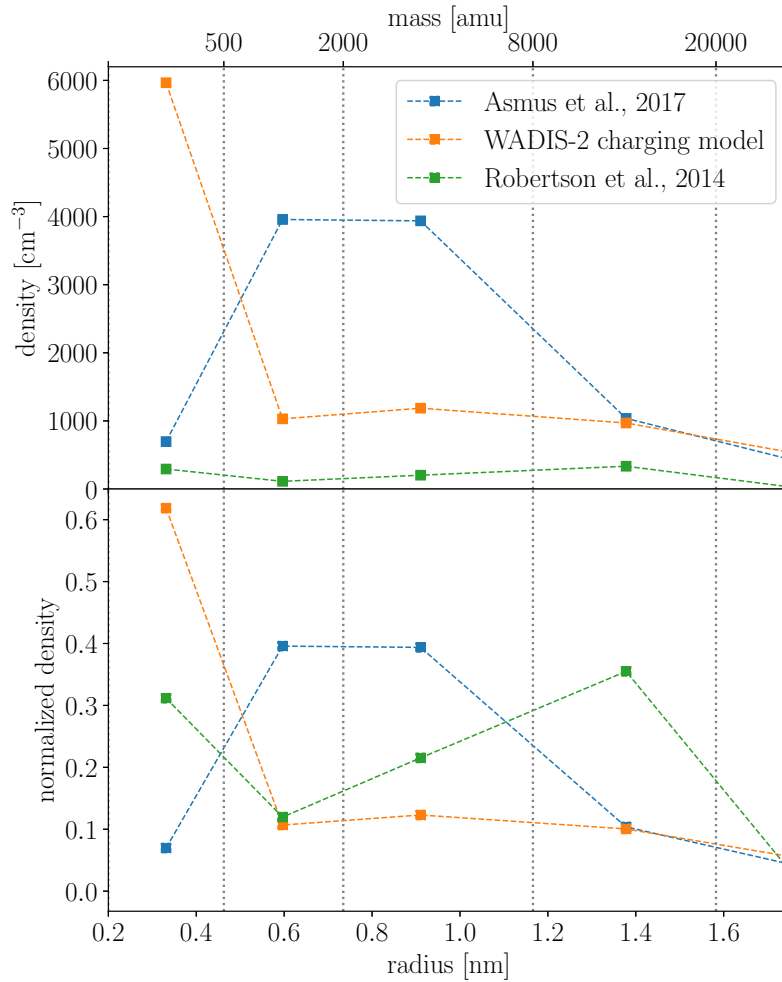


Figure 7.1: **Upper panel:** Charge densities at 82 km derived from the size distribution function obtained by in situ measurements (blue), from the charging model (orange) and as comparison the result from the CHAMPS night time flight (green) separated in size bins given by the MASS instrument used in *Robertson et al.* [2014]. **Lower panel:** The same but normalized to the total density of negative charged MSP. MASS data courtesy of Scott Robertson.

1 nm has a huge effect onto the shape of the size distribution. Moreover the model shows that to explain the extended electron depletion below 104 km there have to be a much larger number of smallest charged MSPs which does indicate a more complex shape of the charged particle size distribution. The comparison of the size distributions obtained from measurements and model to results of a previous work showed that charging of the smallest particles is indeed likely. This emphasizes the need for a better understanding of charging processes of particles smaller than 1 nm.

7.4 Size dependent layering of charged MSPs

The Schmidt number obtained from the electron density fluctuations is structured vertically in layers as can be seen in Fig. 5.19. Since Sc can be related to a mean charged particle radius (see Sec. 4.5), these layers can be interpreted as layers of different charged particle size distributions. Small Sc indicate low amount of large charged particles whereas large Sc imply the presence of a relatively large amount of big charged MSP. Model results show that the size is developing smoothly from small at high to large at low altitudes [Megner *et al.*, 2006]. Hence, locally enhanced mean particle size might be linked to temporally short processes for instance turbulence or updraft by propagating gravity waves. Growth rates of MSP are in the range of days to month [Toon and Farlow, 1981]. Since this is significantly longer than the persistence of turbulent structures which is in range of minutes to hours, fluctuations of MSP growth due to turbulence can be neglected [e.g., Rapp, 2003]. Indeed, in the measurements of WADIS-2 there was no clear correlation between the strength of turbulent motions and the charged particle mean radius. However, there can be size depend transport of MSP by the background flow which is most significant at larger scale motions ~ 1 km [Maxey and Riley, 1983]. In addition, direct numerical simulation showed that inhomogeneities in the distribution of heavy particles can occur in a turbulent inhomogeneous flow which is the effect of so-called *Turbophoresis* [e.g., De Lillo *et al.*, 2015]. Also vertical transport by gravity waves can be possible as it was proposed for mesospheric ice particles in summer by Li *et al.* [2010, 2016]. Since this mechanism also depends on the particle radius it may have segregating effects on the MSP population.

The main conclusion here is that there is no clear relation between the presence of turbulence and layers of larger or smaller particles. However, this has to be further investigated since the Schmidt numbers indicate changes in the charge particle size distribution as a function of height.

7.5 The role of atomic oxygen in the charging process of MSPs

Atomic oxygen is essential for the MLT chemistry as it is the main carrier of chemical energy in this region. Its abundance determines the electron density in the D-region during night time by the destruction of negative ions [Fehsenfeld and Ferguson, 1969; Thomas and Bowman, 1985]. Recently, there have been a variety of simple and more sophisticated ionospheric models which consider among electrons and negative ions the presence of MSPs as another plasma constituent [e.g., Baumann *et al.*, 2013; Plane *et al.*, 2014; Robertson *et al.*, 2014; Baumann *et al.*, 2015; Asmus *et al.*, 2015b]. A threshold density of atomic oxygen density above which negative ion formation is widely reduced is for the MLT region $n_O > 1 \times 10^{10} \text{ cm}^{-3}$ [Plane *et al.*, 2014]. This is also seen in the results of the simple charging model showed in Fig. 6.6. The release of electrons from negative ions enables more MSP to become charged by those free electrons [e.g., Asmus *et al.*, 2015b]. To explain the difference between electrons and

positive ions below 80 km one has to account for negative ions in addition to negatively charged MSP. Therefore the atomic oxygen density has to be lower than the threshold. The measurements of atomic oxygen shown in Fig. 6.2 gave values below the threshold at least for the FIPEX measurements. Atomic oxygen measurements by photometers are based on assumptions which might have large uncertainties below 80 km [e.g., Dickinson *et al.*, 1980; Hedin *et al.*, 2009]. These measurements, however, are yet the most established in situ atomic oxygen measurements. A relatively new concept is used by the FIPEX instrument. The major influence on the absolute values of atomic oxygen measured by FIPEX is due to the aerodynamics and instrument absolute calibration [Eberhart *et al.*, 2015].

To reproduce the low electron density below 80 km the atomic oxygen density has to be sufficiently low. The best fit to the measured plasma densities of WADIS-2 is therefore found by using atomic oxygen density by MSIS model which gives the lowest values of [O] below 80 km [Picone *et al.*, 2002]. The difference between the photometer and MSIS atomic oxygen densities is almost three orders of magnitude. Despite the error in the oxygen measurements can be easily a factor of two or larger [Hedin *et al.*, 2009], this huge difference cannot be attributed to measurement uncertainty alone. The difference may be due to the assumption that ozone, which is part of the atomic oxygen retrieval, is in photochemical equilibrium [Smith *et al.*, 2010]. This assumption may not be valid below 80 km anymore [Kulikov *et al.*, 2018]. The FIPEX measurements show lower values below 80 km comparable to MSIS. The difference between FIPEX and MSIS around 70 km is most likely due to instrumental effects as atomic oxygen density usually decreases below 80 km [Gumbel, 1997; Hedin *et al.*, 2009]. A change of atomic oxygen below $1 \times 10^9 \text{ cm}^{-3}$ can cause a large change in the electron density (up to 1 order of magnitude as seen in upper right panel of Fig. 6.7). Hence, the low electron densities below 80 km are most likely due to creation of negative ions which presupposes a low atomic density.

The model calculations of this work shows, that the depletion of electrons by production of negative ions is more efficient than loss of electron due to attachment to MSPs. Using the measured atomic oxygen density, the charging model produces to less MSPs below 80 km to explain the observed electron depletion. This indicates lower atomic oxygen densities as observed at the lower heights. This can be either addressed to uncertainties in the model inputs or to uncertainties in the measurement techniques in the lower altitude range. More in situ measurements of dusty plasma parameters together with absolute atomic oxygen densities are needed to resolve the influence of [O] onto the charge balance below 80 km.

In summary it was found that the larger the atomic oxygen density the more free electrons are available to charge MSPs. Low electron densities below 80 km indicate low atomic oxygen densities which contradicts the photometer measurements. Depletion of electrons is more effective due to formation of negative ions compared to attachment to MSPs.

Chapter 8

Summary and Outlook

In this chapter the results of the thesis are summarized in such a way, that first the results are generally summarized and subsequently that the work's objectives formulated in Sec. 1.4 are met. Finally an outlook with open questions and further topics of interest is given.

8.1 Summary

This work consists of two parts. In the first part in situ measurements of dusty plasma in the polar MLT region including electrons, positive ions and heavy charged particles are analyzed. For the first time such measurements were performed with high spatial resolution in common volume. The main aim was the investigation of dusty plasma properties which includes charged particle size distribution, charge balance, plasma diffusion and charging processes. Data from one sounding rocket launched during night time in March 2015 from Andøya Space Center (69 °N) in Northern Norway were analyzed. The data were measured by seven different instruments. Electron density was measured by means of wave propagation experiment and an electrostatic probe. An ionization gauge yields neutral gas parameters such as density and temperature but also turbulent energy dissipation rates. Charged dust densities were obtained using a Faraday cup instrument. In the second part of this work measured parameters were used as input for a simple charging model. This model describes basic physical processes and the main aim was the geophysical interpretation of changes to model inputs in order to reproduce the measured plasma densities. The model inputs originating from other models were adjusted. Subsequently, results of both, instrumental analysis and modeling are summarized.

For the first time the WADIS payload configuration allowed common volume in situ measurements of neutral and all dusty plasma components namely, positive ions, electrons and charged dust. In order to enable the interpretation of the particle detector measurements, aerodynamical and electrostatic simulations were performed. The simulations show, that below 80 km aerodynamic effects increase and particle detection becomes rapidly inefficient which is in agreement with earlier observations. For the WADIS configuration particles with radii down to roughly 1.4 nm can be detected at 82 km. From the measurements of plasma densities it was found that there was a large electron depletion below 100 km which can be explained by the existence of negatively charged MSPs at least down to 80 km. This supports the findings of earlier studies. Electron density was measured down to 70 km, however, negative ions have not been measured and hence introduce some uncertainty determining charge balance below 80 km. Additionally, the measured charged dust layer was found to

coincide with a layer of enhanced atomic iron density which supports the assumption that iron is a part of MSP material.

It is known that there can be phase shifts between density fluctuations of neutrals and plasma constituents such as electrons and positive ions. This is due to difference between the scale heights of neutrals and plasma components. In this work it was found that regions where the fluctuations of neutral and electron density are in anti-phase coincide with measured turbulence which is in analogy to previously studies of neutral and positive ion density fluctuations. The anti-correlation indicates that the plasma fluctuations measured during WADIS-2 were purely driven by turbulent processes. Neutrals and electrons were structured down to spatial scales of a couple of meters and reveal, in anti-correlation, the same structures in the same altitude. This once more shows the strong coupling between neutral and plasma components. An additional finding was that the electron density fluctuation spectrum was extended to smaller scales than the spectrum of neutral density fluctuations in some altitude ranges. For the first time this has been observed for electrons in polar winter night time indicating the presence of heavy charged MSPs and their influence on electron diffusivity. Energy dissipation rates were used to calculate Schmidt numbers from electron density fluctuations. In the context of layering of Schmidt numbers it was found that energy dissipation rates and Schmidt numbers, i.e. mean particle radii do not show a clear correlation indicating no connection between turbulence and electron diffusivity. Hence, the layering of Schmidt numbers is not mainly driven by turbulence, e.g. by size depending segregation. The measurements of electron density fluctuation showed that the Schmidt numbers for electrons in the winter mesosphere can be larger than 1. However, the values are smaller than found during summer time meaning that the influence of charged particles on the electron diffusivity is small if there are no large ice particles. As known from previous investigations, there is a connection between Schmidt number and mean particle size. This was previously applied to measurements in the vicinity of large ice particles ($r > 8$ nm).

In this work, for the first time, the relation between Schmidt number and mean particle size was applied to particle radii below 1 nm. Notably the measurements were conducted in the presence of pure MSPs instead of ice particles. It was found in this study that there is a lower limit down to which the conversion of Schmidt number to particle radii is reasonable. The limit was found to be $Sc \approx 3$ or $r \approx 0.45$ nm. The largest mean particle radius was found to be 0.75 nm which is in good agreement with previous studies. To explain the absence of polar mesospheric winter echoes during WADIS-2 turbulent energy dissipation rates and electron Schmidt numbers obtained from the in situ measurements were used to derive radar volume reflectivity η for the MAARSY radar. Resulting η -values are several orders of magnitude smaller than the detection limit of MAARSY. Hence, the signal was way too small to be detected which perfectly explains the absence of echoes.

A new method of deriving a charged particle size distribution function was presented in this work using independent in situ measurements. Available parameters deduced from measurements were total density of charged MSPs, density of a fraction of charged MSPs and the mean radius of all charged MSPs. Due to these constraints only simple distribution functions with one maximum were applicable. The lognormal distribution obtained the best results for this method. The results show that the majority of the particles were smaller than 1.5 nm which is in agreement with earlier findings.

In addition the charge balance was studied in more detail. First of all a simple appro-

ach was used to estimate the number of electrons from the measured positive ion density. The difference to the measured electron density gives the estimated charged MSP density, which was in the order of $20\,000\text{ cm}^{-3}$. A simple 1d charging model was adapted trying to reproduce the measured data. This model includes electrons, positive ions, negative ions, neutral and charged MSP of different sizes. Most of the model inputs were taken from measurements. Additional inputs were taken from models. It is known that the existence of negative ions in the lower D-region mainly depends on the density of atomic oxygen because it destroys the primary negative ion O_2^- . The modeling results show that at low atomic oxygen densities the overall degree of ionization increases whereas electron density decreases which is in agreement with earlier findings. The increase of ionization is due to the longer lifetime of negative ions compared to free electrons. In this work the feedback of atomic oxygen onto charging of MSPs was investigated. It was shown in previous works that charging of MSPs is strongly coupled to electron density. The presented modeling results show that if atomic oxygen densities are low the negatively charged MSPs density decreases due to the formation of negative ions. Additionally it was found that smaller MSPs are more affected by the presence of negative ions since the charging rate of a MSP scales with its size.

In the second part of this work measured plasma densities are compared to modeling results. In order to reproduce the measured plasma densities, the model inputs originating from other models were adjusted. One finding was that the neutral MSP background had to be shifted from $\sim 80\text{ km}$ to $\sim 88\text{ km}$ in order to yield model results in better agreement with the measurements. This shift indicates that the meteor ablation peak height is also in this altitude range which is in agreement with meteor input function obtained by radar measurements. Furthermore a reduced atomic oxygen density compared to photometer measurements was necessary to reproduce the electron density below $\sim 80\text{ km}$. It is believed that at these altitudes both measurements might have uncertainties justifying the adjustment of density to lower values.

Different shapes of charged particle size distributions were tested in order to reproduce the observations in the first part of this work. The size distribution of negatively charged MSPs from the model has a more complex shape with more than one maximum. This finding supports size depending measurements of charged MSP density of previous measurements by *Robertson et al.* [2014]. In order to reproduce the WADIS-2 plasma densities electrons in the model have to attach to and remain on smallest MSPs ($r < 1\text{ nm}$). This indicates that the probability that electrons stay on very small MSP is large, i.e., they consist of molecules with high electron affinity.

The objectives of this work are given in Sec. 1.4. Subsequently the results are summarized with respect to these objectives.

1. Do charged dust particles alter the response of free electrons to neutral turbulent motions in winter?

There are very few measurements of dust in winter. The unique payload configuration of the WADIS-2 rocket enabled common volume measurements of all dusty plasma components. By means of this instrument constellation we could show for the first time that charged MSPs can have an effect on free electron motion in the presence of neutral turbulence even though their mean radius is small ($\sim 0.5\text{ nm}$). As the presented results show, in the presence of charged MSP free electrons are structured to smaller scales than neutrals. This effect, however, is much smaller compared to the influence

by large ice particles in summer which requires very sensitive instrumentation.

2. Which dust sizes contribute to charged fraction of the dust ensemble? How is the shape of their size distribution?

In this work it was shown that the conversion of Schmidt number to mean particle radius can be applied to MSP down to a lower limit of $Sc \approx 3$ and $r \approx 0.45$ nm. The mean radius of charged particles found in this study was between 0.5 nm to 0.8 nm which is in agreement with earlier findings. A new method to derive a charged particle size distribution by means of independent measurements yields a lognormal distribution where the majority of particles are smaller than 1.5 nm which also supports previous works.

The modeling results presented in this work revealed that to reproduce the measured dusty plasma densities the resulting charged particle size distribution is of a more complex shape with two maxima. This finding indicate that smallest MSPs might be efficiently charged which supports previous measurements by *Robertson et al.* [2014].

3. Can smallest charged dust particles explain huge electron depletions above 80 km?

In agreement with earlier measurements the WADIS-2 measurements and model calculations presented in this work confirm that the electron depletion is caused by charged MSPs. It was furthermore found that the huge difference between electron and positive ion density above 80 km can be explained by a large amount of charged MSPs with radii around 0.5 nm or smaller.

4. How does atomic oxygen influence the charging of MSP?

It is known that atomic oxygen controls the amount of negative ions during night time. The model calculations show that for oxygen densities larger than $\sim 1 \times 10^9$ cm⁻³ there are no negative ions which supports earlier work. It was previously shown that the charging of MSP mainly depends on the presence of electrons which is confirmed by the presented modeling results. Moreover, the model calculations show that the larger atomic oxygen density the larger is the charged MSP density. Possibly, atomic oxygen controls the amount of MSPs by regulating the available amount of free electrons.

The findings of this work support that charged MSPs play an important role in the lower D-region. Notably a first experimental proof was presented that charged MSPs can decrease the diffusivity of free electrons in winter. It was shown that above 80 km during winter night time the majority of the charged MSPs is likely to be smaller than 1 nm and their density can exceed the electron density by one order of magnitude.

8.2 Outlook

The deeper one delves into a topic the more questions arise and the initial to-do list rather grows. This work focuses on the properties of dusty plasma during winter night time. However, analysis and instrument techniques developed in the course of this work are planned to be applied to the future project called PMWE whose first campaign was conducted in April 2018. The plasma to neutral coupling is an essential mechanism to form the so-called polar mesospheric winter echoes. Here it is important to estimate the particles size distribution but also the role of charged MSP in turbulent MLT plasma. Based on the results of combined aerodynamical and electrostatic simulations a new particle detector design

was developed. The new detector should be capable of detecting smaller particles at lower altitudes.

In context of PMWE investigation of segregation effects on charged MSP size distribution by neutral turbulence should be considered. One first step could be done by using existing turbulent fields from DNS with SIMION. Here a wide range of particle sizes can be simulated to estimate their distribution in a turbulent field. The scope of this investigation is whether layers of enhanced mean particle size are produced by turbulence via segregation.

The influence of payload charging onto the measurements is still not well known. It is usually very difficult to obtain the payloads potential without multiple fixed biased or swept Langmuir probes. A new idea of calculating payload potential may be obtained using a fixed biased probe for electrons (CONE) and absolute electron density by the wave propagation experiment. A comparison of both should lead to the missing payload potential. Therefore the probe characteristics should be well known in order to apply the appropriate theory.

The simple charging model includes photodetachment and might be used to estimate charge dust densities during daytime.

Appendix A

WADIS-2

A.1 Launch information

Table A.1: Launch parameter of the WADIS-2 flight.

	value
Date	05.03.2015
Time	01:44 UT
Location	Andøya Space Center (69° N, 16° E)
apogee	126.05 km @ T+ 175 s
Exp. Phase	54 km to 100 km, T+52 s to T+ 101 s
Roll (spin) rate	3.27 Hz

A.2 Trajectory fit parameter

The trajectory of a rocket can completely be described by altitude, latitude and longitude. Those quantities are measured for example by a GPS receiver on board the rocket which has a low sampling rate (~ 50 Hz). To assign a position in the 3 dimensional space to each time step defined by the instruments sampling rate usually 4 order polynomials are used. For altitude at time t this relation is given by

$$z(t) = \sum_i c_i (t - t_{ref})^i,$$

where $i = 0..4$, c_i are the polynomial coefficients and t_{ref} is a reference time which in this case is 0. Hereafter, the coefficients are given for altitude, latitude and longitude.

A.2.1 Altitude

$$c_0 = -1.93991645 \cdot 10^4$$

$$c_1 = 1.67153022 \cdot 10^3$$

$$c_2 = -4.87771935$$

$$c_3 = 5.72293713 \cdot 10^{-4}$$

$$c_4 = -8.07050311 \cdot 10^{-7}$$

A.2.2 Latitude

$$\begin{aligned}c_0 &= 6.92690861 \cdot 10^1 \\c_1 &= 1.97388105 \cdot 10^{-3} \\c_2 &= -4.79121001 \cdot 10^{-7} \\c_3 &= 1.10732055 \cdot 10^{-9} \\c_4 &= -3.16217099 \cdot 10^{-13}\end{aligned}$$

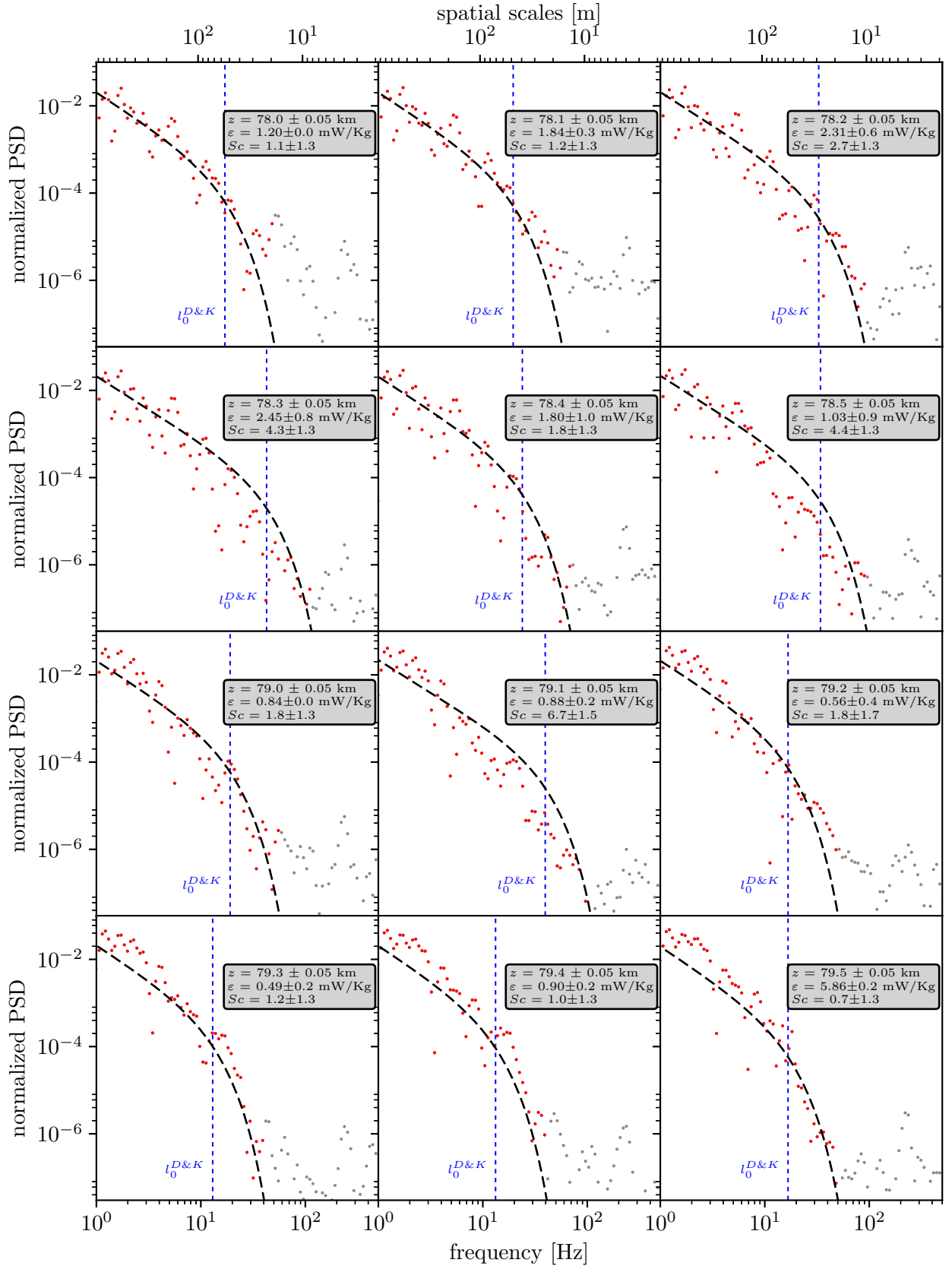
A.2.3 Longitude

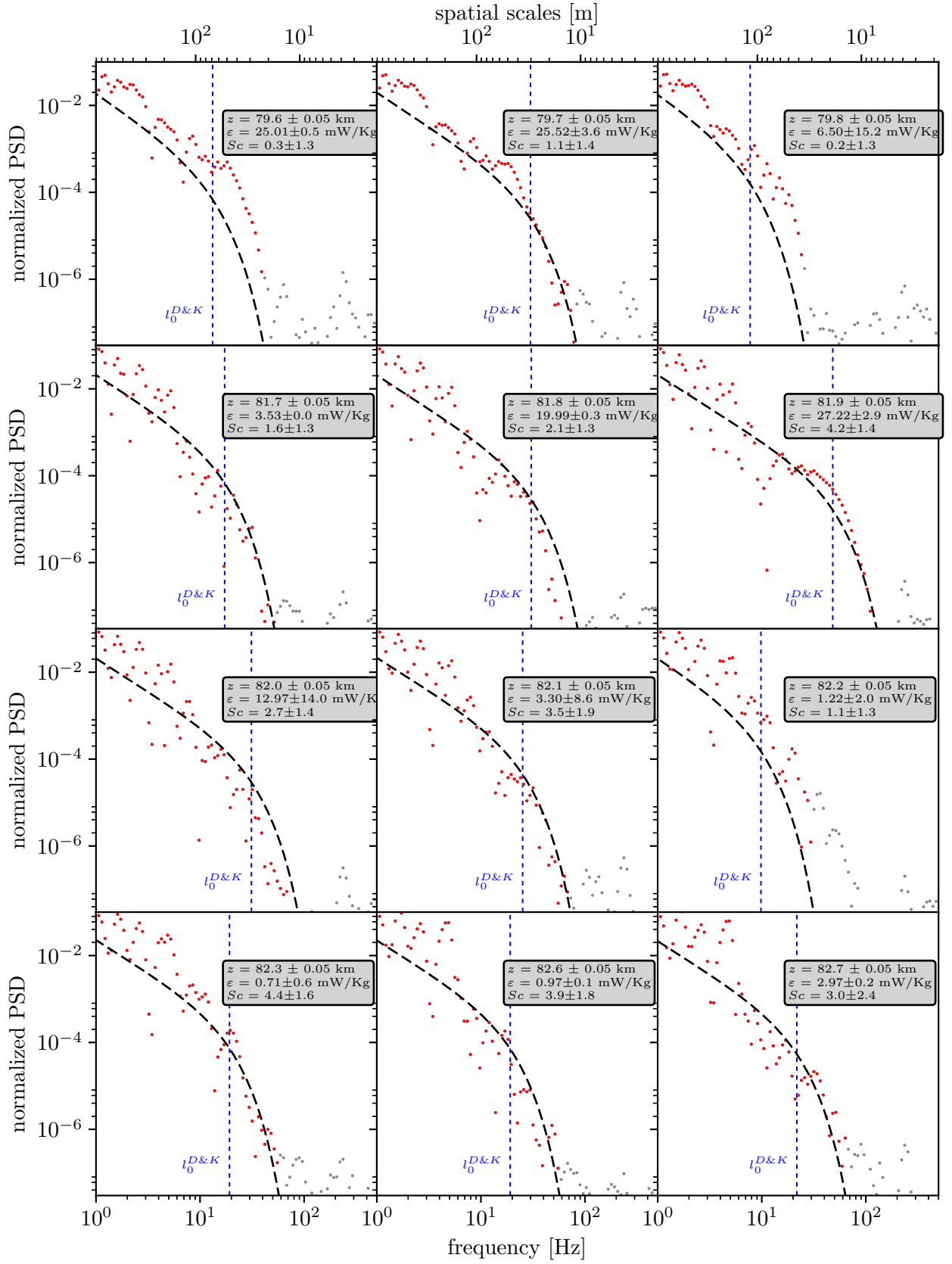
$$\begin{aligned}c_0 &= 1.60557040 \cdot 10^1 \\c_1 &= -2.71227221e \cdot 10^{-3} \\c_2 &= -1.36104321 \cdot 10^{-7} \\c_3 &= 1.86960448 \cdot 10^{-10} \\c_4 &= 8.62366644 \cdot 10^{-13}\end{aligned}$$

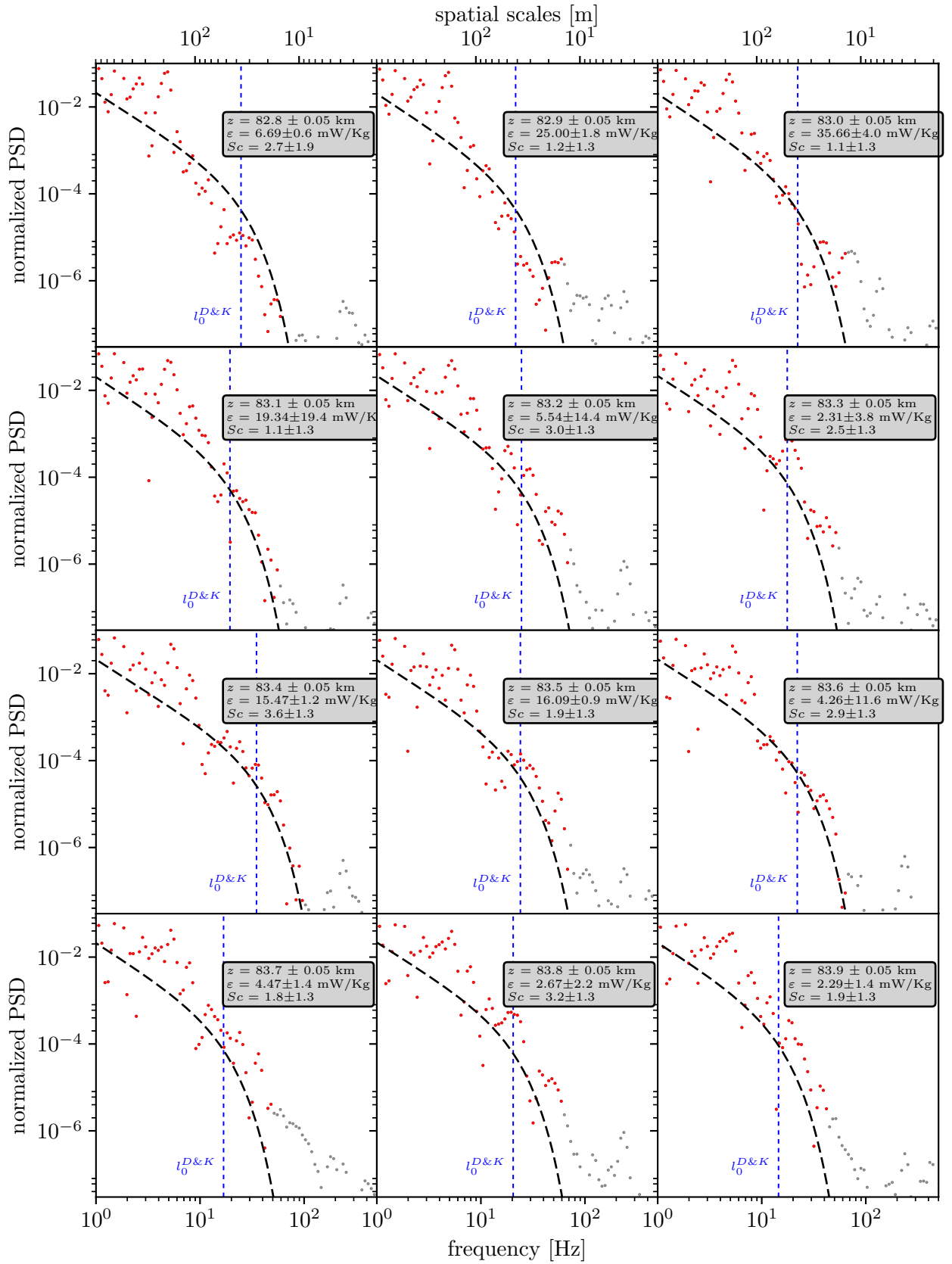
Appendix B

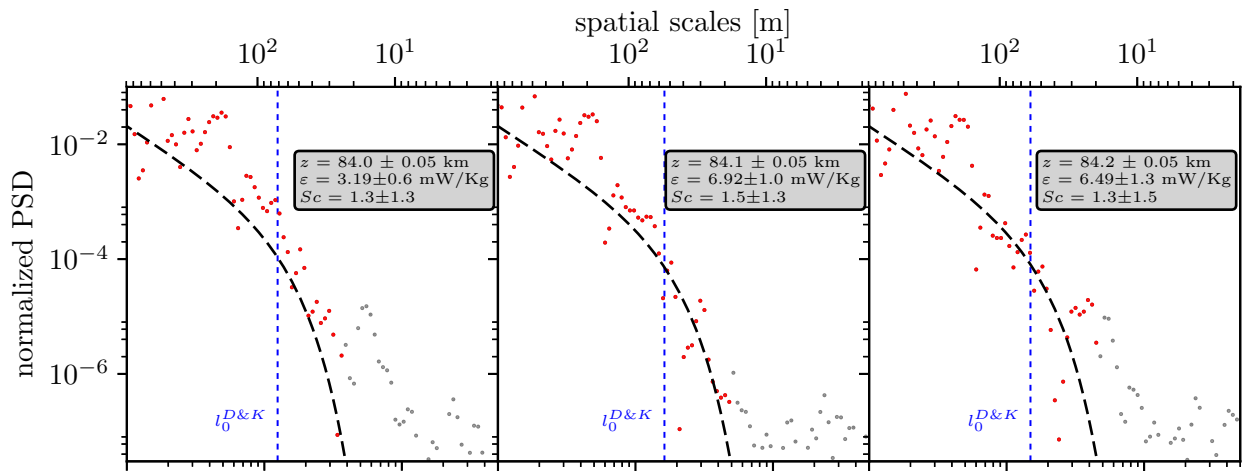
WADIS-2 CONE EP spectra fits

In this part of the appendix all used spectra of the electron density fluctuations with the corresponding fit of the *Driscoll & Kennedy*-model are shown.





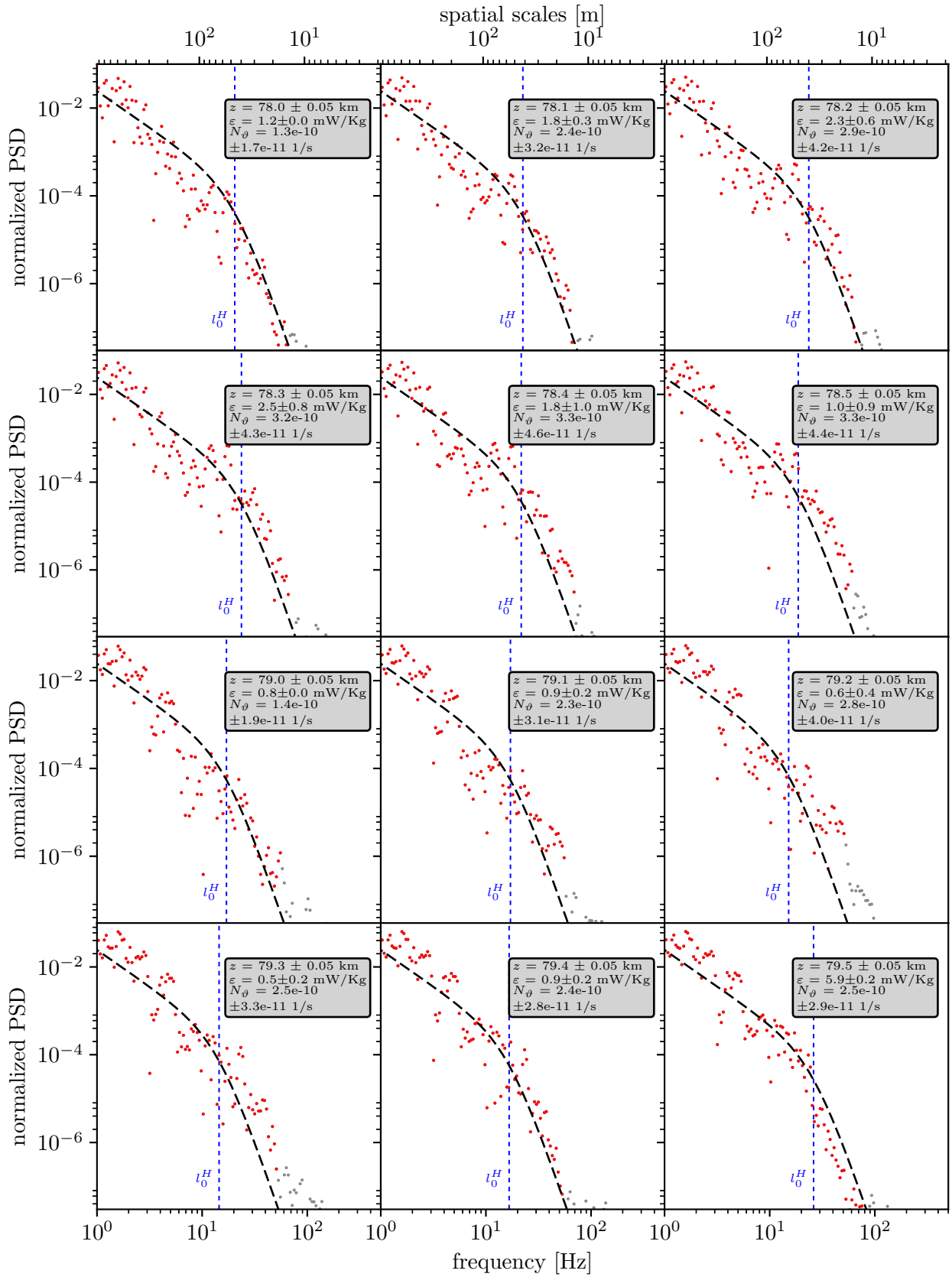


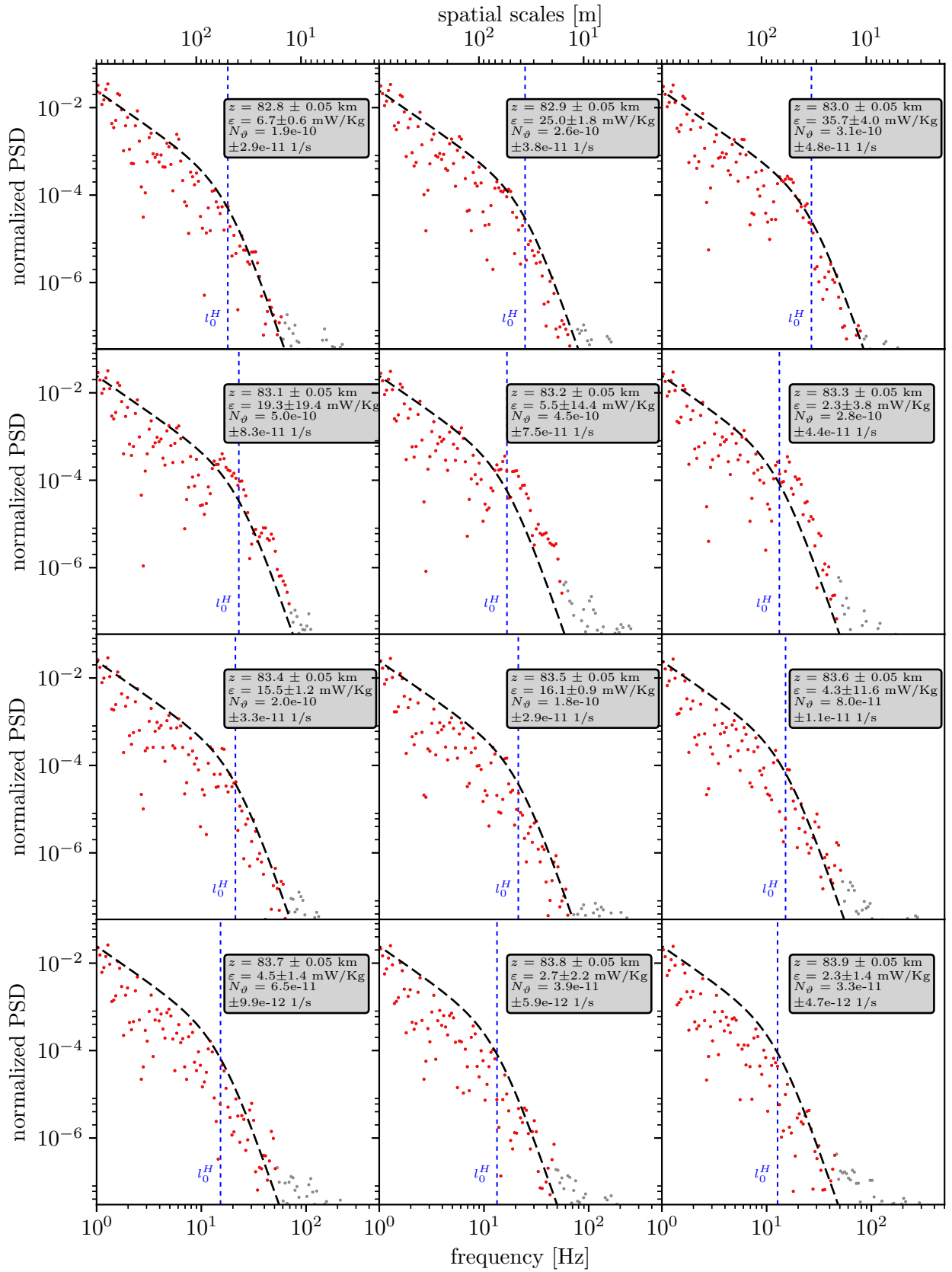


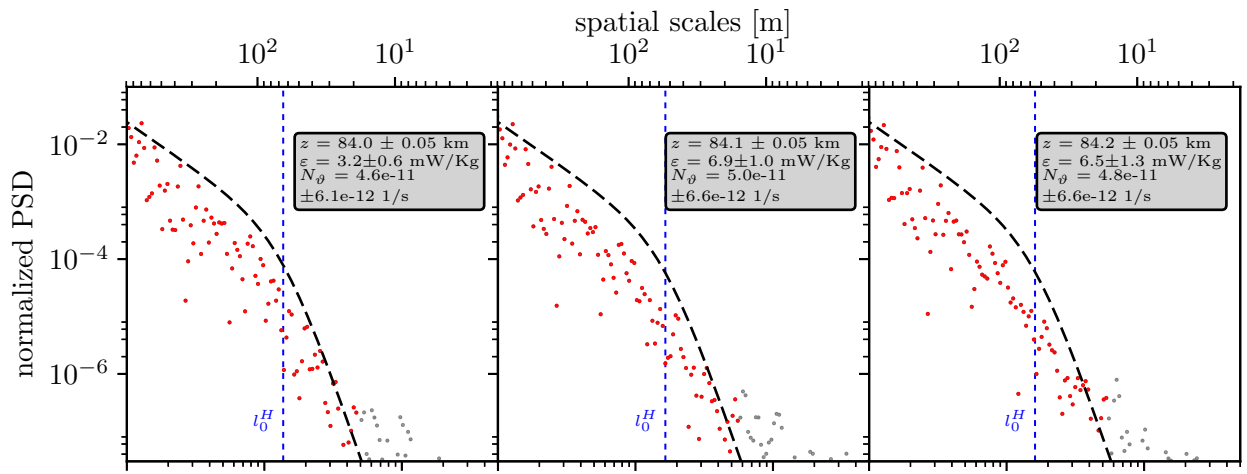
Appendix C

WADIS-2 CONE NP spectra fits

In this part of the appendix all used spectra of the neutral density fluctuations with the corresponding fit of the *Heisenberg*-model are shown.







Appendix D

Uncertainty estimation

Subsequently the estimation of uncertainties is described. This is done for parameters obtained from the analysis of neutral and electron density fluctuations. These are the turbulent energy dissipation rate ε , Schmidt number Sc and particle radius r obtained by spectral method described in Sec. 2.1.2 and the relation to the particle size given in Sec. 4.5.

D.1 Uncertainty of ε and Sc

The turbulent energy dissipation rate obtained from the neutral density fluctuation inherits uncertainties which arise mainly from the quality of fitting the *Heisenberg*-model and number of fitted parameters. Uncertainties introduced by aerodynamics are neglected in this study. The uncertainty of ε for the Levenberg-Marquardt technique of solving least-square problem is then solely given by the 1- σ error scaled by the measured χ^2 -value.

$$u_\varepsilon = \sqrt{C_{kk}^{-1} \frac{\chi^2}{n-p}}, \quad (\text{D.1})$$

where C_{kk}^{-1} is the 1- σ error of each fitted parameter derived from the covariance matrix, χ^2 is the weighted chi-squared value, n is the number of data values and p the number of parameters to fit. In the case of neutral air turbulence this are two parameters, ε and the variance dissipation rate N_ϑ . A more rigorous treatment of error estimation can be found in *Szewczyk [2015]*.

As the Schmidt number is also obtained fitting a spectral model to a measured spectra of tracer density fluctuations, its uncertainty is depending on the quality of the fit. Since one uses the ε -value from the neutral density fluctuations as fixed parameter, the uncertainty of ε propagates into the Schmidt number uncertainty. This influence was estimated varying ε by its uncertainty, fit for the Schmidt number and measure the variance of it. The maximum was found to be 0.8. An additional uncertainty enters the derivation of Sc by using only a part of the measured spectrum to be fitted. By varying this part also the obtained Schmidt number alters. this influence was estimated by perform ten fits with randomly sized fitting windows. Afterwards the 1- σ error of Sc was calculated ($\sigma = 0.5$). The final uncertainty of Schmidt number is than

$$u_{Sc} = \sqrt{u_{fit}^2 + u_{prop,\varepsilon}^2} + u_{window}, \quad (\text{D.2})$$

where u_{fit} is uncertainty corresponding to the fit quality (analog to u_ε explained above), $u_{prop,\varepsilon}$ is the propagating error of the ε derivation and u_{window} is a statistical error introduced

by using different fitting windows.

D.2 Uncertainty of particle radius

Main influence on the particle radius uncertainty is introduced by the Schmidt number. Uncertainties of other quantities such as neutral density and temperature are considered to be negligible.

D.2.1 Polarization model

Following standard theory of propagation of error the uncertainty of radii derived by the polarization model is

$$u_{r^P} = \left| \frac{dr_d^P}{dSc} \right| \cdot \Delta Sc, \quad (\text{D.3})$$

where ΔSc is the Schmidt number uncertainty defined in Sec. D.1. Inserting Eq. 4.20 into D.3 and differentiating yields

$$u_{r^P} = \left| -\frac{2}{3} \frac{v^2}{Sc^3 C_P^2} \left(\frac{3m_n}{4\pi\rho} \frac{1}{\left(\frac{v}{Sc C_P} \right)^2 - 1} \right)^{-\frac{2}{3}} \cdot \left(-\frac{3m_n}{4\pi\rho} \frac{1}{\left(\frac{v}{Sc C_P} \right)^2 - 1} \right) \right| \cdot \Delta Sc \quad (\text{D.4})$$

where $C_P = \frac{9.06 \times 10^5 k_B T}{N_n |Z_a| e} \sqrt{\frac{\epsilon_0}{\pi a m_n}}$.

D.2.2 Hard sphere model

In analogy to the previous section uncertainty of radii derived by the hard sphere model is

$$u_{r^H} = \left| \frac{dr_d^H}{dSc} \right| \cdot \Delta Sc \quad (\text{D.5})$$

inserting Eq. 4.24 and differentiating yields

$$u_{r^H} = \left| \frac{a}{2} \frac{1}{\sqrt{Sc} C_H} \right| \cdot \Delta Sc \quad (\text{D.6})$$

where $C_H = \frac{8}{3} v N_n \sqrt{\frac{2\pi m_n}{k_B T}}$.

Appendix E

SIMION Lua user program

In order to use external fields SIMION[®] there is a need for an additional so called user program written in Lua language. This program calls the collision model (collision_hs1.lua) which is a hard sphere collision model. For documentation reasons the user program code is listed in the following.

```
1 simion.workbench_program()
2 local HS1 = simion.import "collision_hs1.lua" -- Import HS1 collision model
3 -- Number of example to test.
4 adjustable _gas_mass_amu = 28
5
6 function HS1.init()
7     -- First make sure P,T,v arrays from previous runs are unloaded
8     -- to prevent accumulating multiple copies in memory. Then install
9     for i=#simion.pas,1,-1 do
10         print(i,simion.pas[i].filename)
11         if simion.pas[i].filename == 'pressure.pa' or
12            simion.pas[i].filename == 'temperature.pa' or
13            simion.pas[i].filename == 'u.pa' or
14            simion.pas[i].filename == 'v.pa' or
15            simion.pas[i].filename == 'w.pa'
16         then
17             simion.pas[i]:close()
18         end
19     end
20     -- velocity in x direction
21     local vel_x = simion.pas:open('u.pa')
22     function HS1.velocity_x(x_gu, y_gu, z_gu)
23
24         return vel_x:potential_vc(x_gu, y_gu, z_gu)/1000 -- /1000 from m/s to
25
26     end
27     -- velocity in y direction
28     local vel_y = simion.pas:open('v.pa')
29     function HS1.velocity_y(x_gu, y_gu, z_gu)
30
31         return vel_y:potential_vc(x_gu, y_gu, z_gu)/1000 -- /1000 from m/s to m
```

32
33
34
35
36
37
38
39
40
41
42
43
44
45
46
47
48
49
50
51
52
53
54
55
56
57
58
59
60
61
62
63
64
65
66
67
68

```
    end
    -- velocity in z direction
    local vel_z = simion.pas:open('w.pa')
    function HS1.velocity_z(x_gu, y_gu, z_gu)

return vel_z:potential_vc(x_gu, y_gu, z_gu)/1000 -- /1000 from m/s to mm/Å

    end
    -- temperature
    local temp = simion.pas:open('temperature.pa')
    function HS1.temperature(x_gu, y_gu, z_gu)

return temp:potential_vc(x_gu, y_gu, z_gu)

    end
    -- pressure
    local pres = simion.pas:open('pressure.pa')
    function HS1.pressure(x_gu, y_gu, z_gu)

return pres:potential_vc(x_gu, y_gu, z_gu)

    end
end
```

Bibliography

- Antonsen, T., O. Havnes, and I. Mann, Estimates of the size distribution of meteoric smoke particles from rocket-borne impact probes, *Journal of Geophysical Research: Atmospheres*, 122(22), doi:10.1002/2017JD027220, 2017.
- Appleton, E. V., and M. a. F. Barnett, Local Reflection of Wireless Waves from the Upper Atmosphere, *Nature*, 115(2888), 333–334, doi:10.1038/115333a0, 1925.
- Archenhold, F., Die verwendung der Photographie bei der Erforschung der leuchtenden Nachtwolken, Sternschnuppen und Nebelflecken, *Photogr Mitt*, 31, 3–6, 1894.
- Arnold, F., and A. A. Viggiano, Combined mass spectrometric composition measurements of positive and negative ions in the lower ionosphere-I. Positive ions, *Planetary and Space Science*, 30(12), 1295–1305, doi:10.1016/0032-0633(82)90103-9, 1982.
- Arnold, F., A. A. Viggiano, and E. E. Ferguson, Combined mass spectrometric composition measurements of positive and negative ions in the lower ionosphere-II. Negative ions, *Planetary and Space Science*, 30(12), 1307–1314, doi:10.1016/0032-0633(82)90104-0, 1982.
- Arnold, K. S., and C. Y. She, Metal fluorescence lidar (light detection and ranging) and the middle atmosphere, *Contemporary Physics*, 44(1), 35–49, doi:10.1080/00107510302713, 2003.
- Asmus, H., B. Strelnikov, and M. Rapp, In situ measurements of charged mesospheric ice particles during the PHOCUS 2011 campaign and comparison of the results with a microphysical model, in *European Space Agency, (Special Publication) ESA SP*, vol. 721 SP, pp. 489–493, 2013.
- Asmus, H., H. Wilms, B. Strelnikov, and M. Rapp, On the heterogeneous nucleation of mesospheric ice on meteoric smoke particles: Microphysical modeling, *Journal of Atmospheric and Solar-Terrestrial Physics*, 118, 180–189, doi:10.1016/j.jastp.2014.03.009, 2014.
- Asmus, H., C. Baumann, T. Staszak, N. Karow, P. Schünemann, A. Fencik, R. Mainz, E. Jeglorz, and B. Strelnikov, MEDUSA - measurements of the D-region plasma using active falling plasma probes on board of the REXUS15 sounding rocket, *Proceedings of the 22th ESA Symposium on European Rocket and Balloon Programmes and Related Research*, 2015a.
- Asmus, H., S. Robertson, S. Dickson, M. Friedrich, and L. Megner, Charge balance for the mesosphere with meteoric dust particles, *Journal of Atmospheric and Solar-Terrestrial Physics*, 127, 137–149, doi:10.1016/j.jastp.2014.07.010, 2015b.
- Asmus, H., T. Staszak, B. Strelnikov, F.-J. Lübken, M. Friedrich, and M. Rapp, Estimate of size distribution of charged MSP measured in-situ in winter during WADIS-2 sounding rocket campaign, *Annales Geophysicae*, (4), 979–998, doi:10.5194/angeo-35-979-2017, 2017.

- Backhouse, T., The luminous cirrus cloud of June and July, *Meteorological Magazine*, 20, 133, 1885.
- Bailey, S. M., et al., Comparing nadir and limb observations of polar mesospheric clouds: The effect of the assumed particle size distribution, *Journal of Atmospheric and Solar-Terrestrial Physics*, 127, 51–65, doi:10.1016/j.jastp.2015.02.007, 2015.
- Bartels, J., N. H. Heck, and H. F. Johnston, The three-hour-range index measuring geomagnetic activity, *Journal of Geophysical Research*, 44(4), 411, doi:10.1029/TE044i004p00411, 1939.
- Batchelor, G. K., Small-scale variation of convected quantities like temperature in turbulent fluid Part 1. General discussion and the case of small conductivity, *Journal of Fluid Mechanics*, 5(01), 113, doi:10.1017/S002211205900009X, 1959.
- Baumann, C., M. Rapp, A. Kero, and C.-F. Enell, Meteor smoke influences on the D-region charge balance: review of recent in situ measurements and one-dimensional model results, *Annales Geophysicae*, 31(11), 2049–2062, doi:10.5194/angeo-31-2049-2013, 2013.
- Baumann, C., M. Rapp, M. Anttila, A. Kero, and P. T. Verronen, Effects of meteoric smoke particles on the D region ion chemistry, *Journal of Geophysical Research: Space Physics*, 120(12), 10,823–10,839, doi:10.1002/2015JA021927, 2015.
- Baumann, C., M. Rapp, and A. Kero, Secondary electron emission from meteoric smoke particles inside the polar ionosphere, *Ann. Geophys*, 34, 573–580, doi:10.5194/angeo-34-573-2016, 2016.
- Baumgarten, G., and H. K. Fricke, Investigation of the shape of noctilucent cloud particles by polarization lidar technique, *Geophysical Research Letters*, 29(13), 1–4, doi:10.1029/2001GL013877, 2002.
- Becker, E., and G. Schmitz, Climatological Effects of Orography and Land-Sea Heating Contrasts on the Gravity Wave-Driven Circulation of the Mesosphere, *Journal of the Atmospheric Sciences*, 60(1983), 103–118, doi:10.1175/1520-0469(2003)060<0103:CEOAL>2.0.CO;2, 2003.
- Belova, E., M. Smirnova, M. T. Rietveld, B. Isham, S. Kirkwood, and T. Sergienko, First observation of the overshoot effect for polar mesosphere winter echoes during radiowave electron temperature modulation, *Geophysical Research Letters*, 35(3), L03,110, doi:10.1029/2007GL032457, 2008.
- Bennett, F., J. Hall, and P. Dickinson, D-region electron densities and collision frequencies from Faraday rotation and differential absorption measurements, *Journal of Atmospheric and Terrestrial Physics*, 34(8), 1321–1335, doi:10.1016/0021-9169(72)90188-2, 1972.
- Berger, U., and U. von Zahn, Icy particles in the summer mesopause region: Three-dimensional modeling of their environment and two-dimensional modeling of their transport, *Journal of Geophysical Research: Space Physics*, 107(A11), 1366, doi:10.1029/2001JA000316, 2002.
- Berger, U., and U. von Zahn, Three-dimensional modeling of the trajectories of visible noctilucent cloud particles: An indication of particle nucleation well below the mesopause, *Journal of Geophysical Research*, 112(D16), D16,204, doi:10.1029/2006JD008106, 2007.

- Bilitza, D., D. Altadill, Y. Zhang, C. Mertens, V. Truhlik, P. Richards, L.-A. McKinnell, and B. Reinisch, The International Reference Ionosphere 2012 - a model of international collaboration, *Journal of Space Weather and Space Climate*, 4(27), A07, doi:10.1051/swsc/2014004, 2014.
- Bird, G., <http://www.gab.com.au/>, 2017.
- Bird, G. A., *Molecular gas dynamics and the direct simulation of gas flows*, Oxford engineering science series, vol. 42, {Clarendon Press} and {Oxford University Press}, Oxford and New York, 1994.
- Blix, T. A., E. V. Thrane, and Ø. Andreassen, In situ measurements of the fine-scale structure and turbulence in the mesosphere and lower thermosphere by means of electrostatic positive ion probes, *Journal of Geophysical Research*, 95(D5), 5533, doi:10.1029/JD095iD05p05533, 1990.
- Brasseur, G., and S. Solomon, *Aeronomy of the middle atmosphere: Chemistry and physics of the stratosphere and mesosphere*, 3 ed., Springer, Dordrecht, 2005.
- Brattli, A., Ø. Lie-Svendsen, K. Svenes, U.-P. Hoppe, I. Strelnikova, M. Rapp, R. Latteck, and M. Friedrich, The ECOMA 2007 campaign: Rocket observations and numerical modelling of aerosol particle charging and plasma depletion in a PMSE/NLC layer, *Annales Geophysicae*, 27(2), 781–796, doi:10.5194/angeo-27-781-2009, 2009.
- Carrillo-Sánchez, J. D., J. M. Plane, W. Feng, D. Nesvorný, and D. Janches, On the size and velocity distribution of cosmic dust particles entering the atmosphere, *Geophysical Research Letters*, 42(15), 6518–6525, doi:10.1002/2015GL065149, 2015.
- Cepelcha, Z., J. Borovička, W. G. Elford, D. O. ReVelle, R. L. Hawkes, V. Porubčan, and M. Šimek, Meteor Phenomena and Bodies, *Space Science Reviews*, 84(3/4), 327–471, doi:10.1023/A:1005069928850, 1998.
- Cho, J. Y. N., T. M. Hall, and M. C. Kelley, On the Role of Charged Aerosols in Polar Mesosphere Summer Echoes, *Journal of Geophysical Research*, 97(D1), 875, 1992.
- Clemesha, B., Sporadic neutral metal layers in the mesosphere and lower thermosphere, *Journal of Atmospheric and Terrestrial Physics*, 57(7), 725–736, doi:10.1016/0021-9169(94)00049-T, 1995.
- Dalmann, B.-K., E. Grün, J. Kissel, and H. Dietzel, The ion-composition of the plasma produced by impacts of fast dust particles, *Planetary and Space Science*, 25(2), 135–147, doi:10.1016/0032-0633(77)90017-4, 1977.
- De Lillo, F., M. Cencini, S. Musacchio, and G. Boffetta, Clustering and Turbophoresis in a Shear Flow without Walls, doi:10.1063/1.4943274, 2015.
- Dickinson, P. H. G., W. C. Bain, L. Thomas, E. R. Williams, D. B. Jenkins, and N. D. Twiddy, The Determination of the Atomic Oxygen Concentration and Associated Parameters in the Lower Ionosphere, *Proceedings of the Royal Society of London A: Mathematical, Physical and Engineering Sciences*, 369(1738), 1980.
- Dieminger, W., G. K. Hartmann, and R. Leitinger, *The Upper Atmosphere : Data Analysis and Interpretation*, 1014 pp., Springer Berlin Heidelberg, 1996.

- Dohnanyi, J. S., On the origin and distribution of meteoroids, *Journal of Geophysical Research*, 75(17), 3468–3493, doi:10.1029/JB075i017p03468, 1970.
- Driscoll, R. J., and L. A. Kennedy, Model for the Spectrum of Passive Scalars in an Isotropic Turbulence Field., *Physics of fluids*, 28(1), 72–80, doi:10.1063/1.865128, 1985.
- Duft, D., M. Nachbar, M. Eritt, and T. Leisner, A Linear Trap for Studying the Interaction of Nanoparticles with Supersaturated Vapors, *Aerosol Science and Technology*, 49(9), 683–691, doi:10.1080/02786826.2015.1063583, 2015.
- Eberhart, M., S. Löhle, A. Steinbeck, T. Binder, and S. Fasoulas, Measurement of atomic oxygen in the middle atmosphere using solid electrolyte sensors and catalytic probes, *Atmospheric Measurement Techniques Discussions*, 8(3), 3245–3282, doi:10.5194/amtd-8-3245-2015, 2015.
- Eidhammer, T., and O. Havnes, Size dependence of the mesospheric dust temperature And its influence on the noctilucent clouds and polar mesosphere summer echo phenomena, *Journal of Geophysical Research: Space Physics*, 106(A11), 24,831–24,841, doi:10.1029/2001JA900036, 2001.
- Elford, W., and W. G., A study of winds between 80 and 100 km in medium latitudes, *Planetary and Space Science*, 1(2), 94–101, doi:10.1016/0032-0633(59)90003-0, 1959.
- Elford, W., and D. Robertson, Measurements of winds in the upper atmosphere by means of drifting meteor trails II, *Journal of Atmospheric and Terrestrial Physics*, 4(4-5), 271–284, doi:10.1016/0021-9169(53)90060-9, 1953.
- Espy, P., and H. Jutt, Equilibrium temperature of water–ice aerosols in the high-latitude summer mesosphere, *Journal of Atmospheric and Solar-Terrestrial Physics*, 64(17), 1823–1832, doi:10.1016/S1364-6826(02)00191-8, 2002.
- Fehsenfeld, F., and E. Ferguson, Origin of water cluster ions in the D region, *Journal of Geophysical . . .*, 74(9), 2217–2222, doi:10.1029/JA074i009p02217, 1969.
- Fentzke, J., D. Janches, I. Strelnikova, and M. Rapp, Meteoric smoke particle properties derived using dual-beam Arecibo UHF observations of D-region spectra during different seasons, *Journal of Atmospheric and Solar-Terrestrial Physics*, 71(17-18), 1982–1991, doi:10.1016/j.jastp.2009.09.002, 2009.
- Fentzke, J. T., V. Hsu, C. G. M. Brum, I. Strelnikova, M. Rapp, and M. Nicolls, D region meteoric smoke and neutral temperature retrieval using the Poker Flat incoherent scatter radar, *Geophysical Research Letters*, 39(21), n/a–n/a, doi:10.1029/2012GL053841, 2012.
- Fiedler, J., G. Baumgarten, and F.-J. Lübken, NLC observations during one solar cycle above ALOMAR, *Journal of Atmospheric and Solar-Terrestrial Physics*, 71(3-4), 424–433, doi:10.1016/j.jastp.2008.11.010, 2009.
- Florescu-Mitchell, A., and J. Mitchell, Dissociative recombination, *Physics Reports*, 430(5-6), 277–374, doi:10.1016/J.PHYSREP.2006.04.002, 2006.
- Foerster, W., and O. Jesse, Aufforderung zu Beobachtungen der leuchtenden Nachtwolken., *Astronomische Nachrichten*, 130(28), 425–430, doi:10.1002/asna.18921302802, 1892.
- Folkestad, K., Ionospheric Studies by in situ measurements in sounding rockets, Phd, University of Oslo, 1970.

- Friedrich, M., *Handbook of the Lower Ionosphere*, 1 ed., 161 pp., Verlag der Technischen Universität Graz, Graz, 2016.
- Friedrich, M., and K. M. Torkar, Empirical transition heights of cluster ions, *Advances in Space Research*, 8(4), 235–238, doi:10.1016/0273-1177(88)90249-9, 1988.
- Friedrich, M., and K. M. Torkar, FIRI: A semiempirical model of the lower ionosphere, *Journal of Geophysical Research: Space Physics*, 106(A10), 21,409–21,418, doi:10.1029/2001JA900070, 2001.
- Friedrich, M., K. M. Torkar, R. A. Goldberg, J. D. Mitchell, C. Croskey, and G. Lehmacher, Comparison of plasma probes in the lower ionosphere, in *ESA-SP-397*, pp. 381–386, 1997.
- Friedrich, M., K. M. Torkar, and R. J. Steiner, Empirical recombination rates in the lower ionosphere, *Advances in Space Research*, 34(9), 1937–1942, doi:10.1016/j.asr.2004.04.010, 2004.
- Friedrich, M., M. Rapp, J. M. C. Plane, and K. M. Torkar, Bite-outs and other depletions of mesospheric electrons., *Journal of atmospheric and solar-terrestrial physics*, 73(14-15), 2201–2211, doi:10.1016/j.jastp.2010.10.018, 2011.
- Friedrich, M., M. Rapp, T. Blix, U.-P. Hoppe, K. Torkar, S. Robertson, S. Dickson, and K. Lynch, Electron loss and meteoric dust in the mesosphere, *Annales Geophysicae*, 30(10), 1495–1501, doi:10.5194/angeo-30-1495-2012, 2012.
- Fritts, D. C., and E. V. Thrane, Computation of the ion/neutral density ratio in the presence of wave and chemical effects, *Journal of Atmospheric and Terrestrial Physics*, 52(10-11), 827–834, doi:10.1016/0021-9169(90)90019-J, 1990.
- Gardner, C. S., D. G. Voelz, C. F. Sechrist, and A. C. Segal, Lidar studies of the nighttime sodium layer over Urbana, Illinois: 1. Seasonal and nocturnal variations, *Journal of Geophysical Research*, 91(A12), 13,659, doi:10.1029/JA091iA12p13659, 1986.
- Gelinas, L. J., K. A. Lynch, M. C. Kelley, S. Collins, S. Baker, Q. Zhou, and J. S. Friedman, First observation of meteoritic charged dust in the tropical mesosphere, *Geophysical Research Letters*, 25(21), 4047–4050, doi:10.1029/1998GL900089, 1998.
- Giebeler, J., In-situ-Messungen zur Untersuchung der Rolle von Turbulenz bei der Erzeugung von Radarechos in der polaren Mesosphäre im Sommer, Ph.D. thesis, Bonn University, Bonn, 1995.
- Giebeler, J., F.-J. Lübken, and M. Nägele, CONE - a new sensor for in-situ observations of neutral and plasma density fluctuations, *ESA-SP-355*, (ESA-SP-355), 311–318, 1993.
- Granier, C., J. P. Jegou, and G. Megie, Atomic and ionic calcium in the Earth's upper atmosphere, *Journal of Geophysical Research*, 94(D7), 9917, doi:10.1029/JD094iD07p09917, 1989.
- Grossmann, K. U., et al., Middle atmosphere abundances of water vapor and ozone during MAP/WINE, *Journal of Atmospheric and Terrestrial Physics*, 49(7-8), 827–841, doi:10.1016/0021-9169(87)90022-5, 1987.
- Gumbel, J., Rocket-borne optical measurements of minor constituents in the middle atmosphere, 1997.

- Gumbel, J., Aerodynamic influences on atmospheric in situ measurements from sounding rockets, *Journal of Geophysical Research: Space Physics*, 106(A6), 10,553–10,563, doi:10.1029/2000JA900166, 2001.
- Gumbel, J., D. E. Siskind, G. Witt, K. M. Torkar, and M. Friedrich, Influences of ice particles on the ion chemistry of the polar summer mesosphere, *Journal of Geophysical Research*, 108(D8), 8436, doi:10.1029/2002JD002413, 2003.
- Hall, C., Geomagnetic Data from TGO, 2017.
- Hannemann, M., N. Koborov, and M. Rapp, Probe Measurements in a Low Density Large Volume Afterglow Plasma, in *26th ICPIG Proceedings Vol. 1*, p. 131, 2003.
- Havnes, O., and M. Kassa, On the sizes and observable effects of dust particles in polar mesospheric winter echoes, *Journal of Geophysical Research*, 114(D9), D09,209, doi:10.1029/2008JD011276, 2009.
- Havnes, O., and L. I. Næsheim, On the secondary charging effects and structure of mesospheric dust particles impacting on rocket probes, *Ann. Geophys*, 25(3), 623–637, doi:10.5194/angeo-25-623-2007, 2007.
- Havnes, O., J. Trøim, T. Blix, W. Mortensen, L. I. Næsheim, E. Thrane, and T. Tønnesen, First detection of charged dust particles in the Earth's mesosphere, *Journal of Geophysical Research*, 101(A5), 10,839–10,847, 1996.
- Havnes, O., T. Aslaksen, and A. Brattli, Charged Dust in the Earth's Middle Atmosphere, *Physica Scripta*, 89(1), 133, 2001.
- Havnes, O., C. La Hoz, M. T. Rietveld, M. Kassa, G. Baroni, and A. Biebricher, Dust charging and density conditions deduced from observations of PMWE modulated by artificial electron heating, *Journal of Geophysical Research: Atmospheres*, 116(D24), n/a–n/a, doi:10.1029/2011JD016411, 2011.
- Hedin, J., J. Gumbel, and M. Rapp, On the efficiency of rocket-borne particle detection in the mesosphere, *Atmospheric Chemistry & Physics*, 7, 3701–3711, doi:10.5194/acpd-7-1183-2007, 2007.
- Hedin, J., J. Gumbel, J. Stegman, and G. Witt, Use of O₂ airglow for calibrating direct atomic oxygen measurements from sounding rockets, *Atmospheric Measurement Techniques*, 2(2), 801–812, doi:10.5194/amt-2-801-2009, 2009.
- Heisenberg, W., Zur statistischen Theorie der Turbulenz, *Zeitschrift für Physik*, 124(7-12), 628–657, doi:10.1007/BF01668899, 1948.
- Hervig, M., R. E. Thompson, M. McHugh, L. L. Gordley, J. M. Russell, and M. E. Summers, First confirmation that water ice is the primary component of polar mesospheric clouds, *Geophysical Research Letters*, 28(6), 971–974, doi:10.1029/2000GL012104, 2001.
- Hervig, M. E., L. L. Gordley, L. E. Deaver, D. E. Siskind, M. H. Stevens, J. M. Russell, S. M. Bailey, L. Megner, and C. G. Bardeen, First Satellite Observations of Meteoric Smoke in the Middle Atmosphere, *Geophysical Research Letters*, 36(18), L18,805, doi:10.1029/2009GL039737, 2009.

- Hervig, M. E., L. E. Deaver, C. G. Bardeen, J. M. Russell, S. M. Bailey, and L. L. Gordley, The content and composition of meteoric smoke in mesospheric ice particles from SOFIE observations, *Journal of Atmospheric and Solar-Terrestrial Physics*, 84-85, 1–6, doi:\url{10.1016/j.jastp.2012.04.005}, 2012.
- Hill, R. J., Nonneutral and quasi-neutral diffusion of weakly ionized multiconstituent plasma, *Journal of Geophysical Research*, 83(A3), 989, doi:10.1029/JA083iA03p00989, 1978.
- Hocking, W. K., Measurement of turbulent energy dissipation rates in the middle atmosphere by radar techniques: A review, *Radio Science*, 20(6), 1403–1422, doi:10.1029/RS020i006p01403, 1985.
- Hocking, W. K., J. Rottger, R. D. Palmer, T. Sato, and P. B. Chilson, *Atmospheric Radar*, Cambridge University Press, Cambridge, doi:10.1017/9781316556115, 2016.
- Hughes, D. W., and D. W., Cosmic dust influx to the earth., *Space Research XV*, p. 531 - 539, pp. 531–539, 1975.
- Hunten, D. M., R. P. Turco, and O. B. Toon, Smoke and Dust Particles of Meteoric Origin in the Mesosphere and Stratosphere, *Journal of the Atmospheric Sciences*, 37(6), 1342–1357, 1980.
- Jensen, E. J., and G. E. Thomas, Charging of mesospheric particles: Implications for electron density and particle coagulation, *Journal of Geophysical Research*, 96(D10), 18,603, doi:10.1029/91JD01966, 1991.
- Jesse, O., Auffallende Abenderscheinung am Himmel, *Meteorologische Zeitung*, 1885.
- Jesse, O., Die Höhe der leuchtenden Nachtwolken, *Astronomische Nachrichten*, 140(11), 161–168, doi:10.1002/asna.18961401102, 1896.
- Kavanagh, A., F. Honary, M. Rietveld, and A. Senior, First observations of the artificial modulation of polar mesospheric winter echoes, 33, 19,801, doi:10.1029/2006GL027565, 2006.
- Kero, A., C.-F. Enell, A. J. Kavanagh, J. Vierinen, I. Virtanen, and E. Turunen, Could negative ion production explain the polar mesosphere winter echo (PMWE) modulation in active HF heating experiments?, *Geophysical Research Letters*, 35(23), L23,102, doi:10.1029/2008GL035798, 2008.
- Kiliani, J., G. Baumgarten, F.-J. Lübken, and U. Berger, Impact of particle shape on the morphology of noctilucent clouds, *Atmospheric Chemistry and Physics*, 15(22), 12,897–12,907, doi:10.5194/acp-15-12897-2015, 2015.
- Knappmiller, S., S. Robertson, Z. Sternovsky, and M. Friedrich, A rocket-borne mass analyzer for charged aerosol particles in the mesosphere, *Review of Scientific Instruments*, 79(10), 104,502, doi:10.1063/1.2999580, 2008.
- Kulikov, M. Y., M. V. Belikovich, M. Grygalashvyly, G. R. Sonnemann, T. S. Ermakova, A. A. Nechaev, and A. M. Feigin, Nighttime Ozone Chemical Equilibrium in the Mesopause Region, *Journal of Geophysical Research: Atmospheres*, 123(6), 3228–3242, doi:10.1002/2017JD026717, 2018.

- La Hoz, C., and O. Havnes, Artificial modification of polar mesospheric winter echoes with an RF heater: Do charged dust particles play an active role?, *Journal of Geophysical Research*, 113(D19), D19,205, doi:10.1029/2008JD010460, 2008.
- Landau, L. D., and E. M. Lifschitz, *Hydrodynamik*, 5., überar ed., Akademie-Verl, Berlin, 1991.
- Latteck, R., and J. Bremer, Occurrence frequencies of polar mesosphere summer echoes observed at 69° N during a full solar cycle, *Advances in Radio Science*, 11, 327–332, doi:10.5194/ars-11-327-2013, 2013.
- Latteck, R., and I. Strelnikova, Extended observations of polar mesosphere winter echoes over Andøya (69° N) using MAARSY, *Journal of Geophysical Research: Atmospheres*, 120(16), 8216–8226, doi:10.1002/2015JD023291, 2015.
- Latteck, R., W. Singer, M. Rapp, B. Vandeppeer, T. Renkwitz, M. Zecha, and G. Stober, MAARSY: The new MST radar on Andøya-System description and first results, *Radio Science*, 47(1), n/a–n/a, doi:10.1029/2011RS004775, 2012.
- Lautenbach, J., and J. Höffner, Scanning iron temperature lidar for mesopause temperature observation., *Applied optics*, 43(23), 4559–63, doi:10.1364/AO.43.004559, 2004.
- Leslie, R. C., Sky Glows, *Nature*, 32(820), 245, 1885.
- Li, H., J. Wu, J. Wu, Z. W. Xu, and B. Xu, Study on the layered dusty plasma structures in the summer polar mesopause, *Annales Geophysicae*, 28(9), 1679–1686, doi:10.5194/angeo-28-1679-2010, 2010.
- Li, H., J. Wu, and Z. Zhou, The formation of multiple layers of ice particles in the polar summer mesopause region, *Ann. Geophys*, 34, 117–122, doi:10.5194/angeo-34-117-2016, 2016.
- Love, S. G., and D. E. Brownlee, A Direct Measurement of the Terrestrial Mass Accretion Rate of Cosmic Dust, *Science*, 262(5133), 550–553, doi:10.1126/science.262.5133.550, 1993.
- Lübken, F.-J., TOTAL: A new instrument to study turbulent parameters in the mesosphere and lower thermosphere, in *ESA SP-270: European Rocket & Balloon Programmes and Related Research*, pp. 215–218, 1987.
- Lübken, F.-J., On the extraction of turbulent parameters from atmospheric density fluctuations, *Journal of Geophysical Research*, 97(D18), 20,385, doi:10.1029/92JD01916, 1992.
- Lübken, F.-J., Experimental Results on the Role of Turbulence for the Heat Budget of the Upper Atmosphere, Habilitation, Bonn University, 1993.
- Lübken, F.-J., Seasonal variation of turbulent energy dissipation rates at high latitudes as determined by in situ measurements of neutral density fluctuations, *Journal of Geophysical Research: Atmospheres*, 102(D12), 13,441–13,456, doi:10.1029/97JD00853, 1997.
- Lübken, F.-J., Turbulent scattering for radars: A summary, *Journal of Atmospheric and Solar-Terrestrial Physics*, 107, 1–7, doi:10.1016/j.jastp.2013.10.015, 2014.
- Lübken, F.-J., J. Giebeler, T. Blix, E. Thrane, W. Singer, and J. Bremer, In-situ measurement of the Schmidt number within a PMSE layer, *Geophysical Research Letters*, 21(15), 1651–1654, doi:10.1029/94GL01355, 1994.

- Lübken, F. J., M. Rapp, T. Blix, and E. Thrane, Microphysical and turbulent measurements of the Schmidt number in the vicinity of polar mesosphere summer echoes, *Geophysical Research Letters*, 25(6), 893–896, doi:10.1029/98GL50479, 1998.
- Lübken, F. J., W. Singer, R. Latteck, and I. Strelnikova, Radar measurements of turbulence, electron densities, and absolute reflectivities during polar mesosphere winter echoes (PMWE), *Advances in Space Research*, 40(6), 758–764, doi:10.1016/j.asr.2007.01.015, 2007.
- Lübken, F.-J., et al., Mean state densities, temperatures and winds during the MAC/SINE and MAC/EPSILON campaigns, *Journal of Atmospheric and Terrestrial Physics*, 52(10-11), 955–970, 1990.
- Lynch, K. A., Multiple sounding rocket observations of charged dust in the polar winter mesosphere, *Journal of Geophysical Research*, 110(A3), doi:10.1029/2004JA010502, 2005.
- Mathews, J. D., D. Janches, D. D. Meisel, and Q. H. Zhou, The micrometeoroid mass flux into the upper atmosphere: Arecibo results and a comparison with prior estimates, *Geophysical Research Letters*, 28(10), 1929–1932, doi:10.1029/2000GL012621, 2001.
- Maxey, M. R., and J. J. Riley, Equation of motion for a small rigid sphere in a nonuniform flow, *Physics of Fluids*, 26(4), 883, doi:10.1063/1.864230, 1983.
- McNeil, W. J., S. T. Lai, and E. Murad, Differential ablation of cosmic dust and implications for the relative abundances of atmospheric metals, *Journal of Geophysical Research: Atmospheres*, 103(D9), 10,899–10,911, doi:10.1029/98JD00282, 1998.
- Mechtly, E. A., Accuracy of rocket measurements of lower ionosphere electron concentrations, *Radio Science*, 9(3), 373–378, doi:10.1029/RS009i003p00373, 1974.
- Mechtly, E. A., S. A. Bowhill, L. G. Smith, and H. W. Knoebel, Lower ionosphere electron concentration and collision frequency from rocket measurements of Faraday rotation, differential absorption, and probe current, *Journal of Geophysical Research*, 72(21), 5239–5245, doi:10.1029/JZ072i021p05239, 1967.
- Megner, L., and J. Gumbel, Charged meteoric particles as ice nuclei in the mesosphere: Part 2, *Journal of Atmospheric and Solar-Terrestrial Physics*, 71(12), 1236–1244, 2009.
- Megner, L., M. Rapp, and J. Gumbel, Distribution of meteoric smoke: sensitivity to microphysical properties and atmospheric conditions, *Atmospheric Chemistry and Physics*, 6(12), 4415–4426, 2006.
- Megner, L., D. E. Siskind, M. Rapp, and J. Gumbel, Global and temporal distribution of meteoric smoke: A two-dimensional simulation study, *Journal of Geophysical Research*, 113(D3), D03,202, doi:10.1029/2007JD009054, 2008.
- Meriwether, J. W., and A. J. Gerrard, Mesosphere inversion layers and stratosphere temperature enhancements, *Reviews of Geophysics*, 42(3), RG3003, doi:10.1029/2003RG000133, 2004.
- Millman, P. M., and P. M., Dust in the solar system, In: *The dusty universe. (A76-15076 04-90)* New York, Neale Watson Academic Publications, Inc., 1975, p. 185–209., pp. 185–209, 1975.
- Murray, B. J., and E. J. Jensen, Homogeneous nucleation of amorphous solid water particles in the upper mesosphere, *Journal of Atmospheric and Solar-Terrestrial Physics*, 72(1), 51–61, 2010.

- Natanson, G. L., On the theory of the charging of microscopic aerosol particles as a result of capture of gas ions., *Sov. Phys. - Tech. Phys (Engl. Transl.)*, 5, 538–551, 1960.
- Picone, J. M., A. E. Hedin, D. P. Drob, and A. C. Aikin, NRLMSISE-00 empirical model of the atmosphere: Statistical comparisons and scientific issues, *Journal of Geophysical Research: Space Physics*, 107(A12), SIA 15–1–SIA 15–16, doi:10.1029/2002JA009430, 2002.
- Plane, J., D. Self, T. Vondrak, and K. Woodcock, Laboratory studies and modelling of mesospheric iron chemistry, *Advances in Space Research*, 32(5), 699–708, doi:10.1016/S0273-1177(03)00401-0, 2003.
- Plane, J. M., et al., A combined rocket-borne and ground-based study of the sodium layer and charged dust in the upper mesosphere, *Journal of Atmospheric and Solar-Terrestrial Physics*, 118, 151–160, doi:10.1016/j.jastp.2013.11.008, 2014.
- Plane, J. M. C., The role of sodium bicarbonate in the nucleation of noctilucent clouds, *Annales Geophysicae*, 18(7), 807–814, 2000.
- Plane, J. M. C., W. Feng, and E. C. M. Dawkins, The mesosphere and metals: chemistry and changes., *Chemical reviews*, 115(10), 4497–541, doi:10.1021/cr500501m, 2015.
- Rapp, M., On the nature of PMSE: Electron diffusion in the vicinity of charged particles revisited, *Journal of Geophysical Research*, 108(D8), 2003.
- Rapp, M., and F.-J. Lübken, Modelling of particle charging in the polar summer mesosphere: Part 1-General results, *Journal of Atmospheric and Solar-Terrestrial Physics*, 63(8), 759–770, doi:10.1016/S1364-6826(01)00006-2, 2001.
- Rapp, M., and F.-J. Lübken, Polar mesosphere summer echoes (PMSE): Review of observations and current understanding, *Atmospheric Chemistry and Physics*, 4(11/12), 2601–2633, 2004.
- Rapp, M., and G. E. Thomas, Modeling the microphysics of mesospheric ice particles: Assessment of current capabilities and basic sensitivities, *Journal of Atmospheric and Solar-Terrestrial Physics*, 68(7), 715–744, 2006.
- Rapp, M., J. Hedin, I. Strelnikova, M. Friedrich, J. Gumbel, and F.-J. Lübken, Observations of positively charged nanoparticles in the nighttime polar mesosphere, *Geophysical Research Letters*, 32(23), doi:10.1029/2005GL024676, 2005.
- Rapp, M., I. Strelnikova, and J. Gumbel, Meteoric smoke particles: Evidence from rocket and radar techniques, *Advances in Space Research*, 40(6), 809–817, doi:10.1016/j.asr.2006.11.021, 2007.
- Rapp, M., I. Strelnikova, R. Latteck, P. Hoffmann, U.-P. Hoppe, I. Häggström, and M. T. Rietveld, Polar mesosphere summer echoes (PMSE) studied at Bragg wavelengths of 2.8 m, 67 cm, and 16 cm, *Journal of Atmospheric and Solar-Terrestrial Physics*, 70(7), 947–961, doi:10.1016/j.jastp.2007.11.005, 2008.
- Rapp, M., R. Latteck, G. Stober, P. Hoffmann, W. Singer, and M. Zeche, First three-dimensional observations of polar mesosphere winter echoes: Resolving space-time ambiguity, *Journal of Geophysical Research: Space Physics*, 116(A11), n/a–n/a, doi:10.1029/2011JA016858, 2011.

- Rapp, M., J. M. C. Plane, B. Strelnikov, G. Stober, S. Ernst, J. Hedin, M. Friedrich, and U.-P. Hoppe, In situ observations of meteor smoke particles (MSP) during the Geminids 2010: Constraints on MSP size, work function and composition, *Annales Geophysicae*, 30(12), 1661–1673, doi:10.5194/angeo-30-1661-2012, 2012.
- Rapp, M., et al., First in situ measurement of the vertical distribution of ice volume in a mesospheric ice cloud during the ECOMA/MASS rocket-campaign, *Annales Geophysicae*, 27(2), 755–766, 2009.
- Rapp, M., et al., Rocket-borne in situ measurements of meteor smoke: Charging properties and implications for seasonal variation, *Journal of Geophysical Research*, 115, 2010.
- Reid, G. C., Ice Particles and Electron “Bite-Outs” at the Summer Polar Mesopause, *Journal of Geophysical Research*, 95(D9), 13,891–13,896, 1990.
- Robertson, S., S. Dickson, M. Horányi, Z. Sternovsky, M. Friedrich, D. Janches, L. Megner, and B. Williams, Detection of meteoric smoke particles in the mesosphere by a rocket-borne mass spectrometer, *Journal of Atmospheric and Solar-Terrestrial Physics*, 118, 161–179, doi:10.1016/j.jastp.2013.07.007, 2014.
- Robertson, S., et al., Mass analysis of charged aerosol particles in NLC and PMSE during the ECOMA/MASS campaign, *Annales Geophysicae*, 27(3), 1213–1232, doi:10.5194/angeo-27-1213-2009, 2009.
- Roper, R. G., Atmospheric turbulence in the meteor region, *Journal of Geophysical Research*, 71(24), 5785–5792, doi:10.1029/JZ071i024p05785, 1966.
- Rosinski, J., and R. H. Snow, Secondary particulate matter from meteor vapors, 1961.
- Röttger, J., C. La Hoz, M. C. Kelley, U.-P. Hoppe, and C. Hall, The structure and dynamics of polar mesosphere summer echoes observed with the EISCAT 224 MHz radar, *Geophysical Research Letters*, 15(12), 1353, 1988.
- Rusch, D., et al., Large ice particles associated with small ice water content observed by AIM CIPS imagery of polar mesospheric clouds: Evidence for microphysical coupling with small-scale dynamics, doi:10.1016/j.jastp.2016.04.018, 2016.
- Saunders, R. W., and J. M. Plane, A laboratory study of meteor smoke analogues: Composition, optical properties and growth kinetics, *Journal of Atmospheric and Solar-Terrestrial Physics*, 68(18), 2182–2202, doi:10.1016/j.jastp.2006.09.006, 2006.
- Saunders, R. W., et al., An aerosol chamber investigation of the heterogeneous ice nucleating potential of refractory nanoparticles, *Atmospheric Chemistry and Physics*, 10(3), 1227–1247, 2010.
- Scanlon, T. J., E. Roohi, C. White, M. Darbandi, and J. M. Reese, An open source, parallel DSMC code for rarefied gas flows in arbitrary geometries, *Computers and Fluids*, 39(10), 2078–2089, doi:10.1016/j.compfluid.2010.07.014, 2010.
- Schult, C., G. Stober, J. L. Chau, and R. Latteck, Determination of meteor-head echo trajectories using the interferometric capabilities of MAARSY, *Annales Geophysicae*, 31(10), 1843–1851, doi:10.5194/angeo-31-1843-2013, 2013.
- Schunk, R. W., and A. F. Nagy, *Ionospheres: Physics, Plasma Physics, and Chemistry*, 628 pp., Cambridge University Press, 2004.

- Sen, H. K., and A. A. Wyller, On the generalization of the Appleton-Hartree magnetoionic formulas, *Journal of Geophysical Research*, 65(12), 3931–3950, doi:10.1029/JZ065i012p03931, 1960.
- Sharp, W. E., The measurement of atomic oxygen in the mesosphere and lower thermosphere, *Planetary and Space Science*, 39(4), 617–626, doi:10.1016/0032-0633(91)90056-G, 1991.
- She, C. Y., J. D. Vance, B. P. Williams, D. A. Krueger, H. Moosmüller, D. Gibson-Wilde, and D. Fritts, Lidar studies of atmospheric dynamics near polar mesopause, *Eos, Transactions American Geophysical Union*, 83(27), 289, doi:10.1029/2002EO000206, 2002.
- Skolnik, M. I. M. I., *Radar handbook*, McGraw-Hill, 2008.
- Smith, A. K., D. R. Marsh, M. G. Mlynczak, and J. C. Mast, Temporal variations of atomic oxygen in the upper mesosphere from SABER, *Journal of Geophysical Research*, 115(D18), D18,309, doi:10.1029/2009JD013434, 2010.
- Staszak, T., Aerodynamische Simulationen von raketenge tragenen in-situ Dichtemessungen in der MLT-region, Ph.D. thesis, University of Rostock, Rostock, 2015.
- Staszak, T., M. Brede, and B. Strelnikov, Open source software OPENFOAM as a new aerodynamical simulation tool for rocket-borne measurements, *Proceedings of the 22th ESA Symposium on European Rocket and Balloon Programmes and Related Research (ESA SP-730)*, pp. 201–207, 2015.
- Stebel, K., U. Blum, K.-H. Fricke, S. Kirkwood, N. J. Mitchell, and A. Osepian, Joint radar/lidar observations of possible aerosol layers in the winter mesosphere, *Journal of Atmospheric and Solar-Terrestrial Physics*, 66(11), 957–970, doi:10.1016/j.jastp.2004.03.008, 2004.
- Strelnikov, B., In situ measurements of small scale neutral and plasma dynamics in the mesosphere/lower thermosphere region, Phd thesis, University of Rostock, 2006.
- Strelnikov, B., M. Rapp, and F.-J. Lübken, A new technique for the analysis of neutral air density fluctuations measured in situ in the middle atmosphere, *Geophysical Research Letters*, 30(20), n/a–n/a, doi:10.1029/2003GL018271, 2003.
- Strelnikov, B., M. Rapp, T. A. Blix, N. Engler, J. Höffner, J. Lautenbach, F.-J. Lübken, B. Smiley, and M. Friedrich, In situ observations of small scale neutral and plasma dynamics in the mesosphere/lower thermosphere at 79° N, *Advances in Space Research*, 38(11), 2388–2393, 2006.
- Strelnikov, B., M. Rapp, I. Strelnikova, N. Engler, and R. Latteck, Small-scale structures in neutrals and charged aerosol particles as observed during the ECOMA/MASS rocket campaign, *Annales Geophysicae*, 27(4), 1449–1456, 2009.
- Strelnikov, B., A. Szewczyk, and M. Rapp, In-situ measurements of small-scale structures in neutrals and plasma species during ECOMA-2010, in *EGU General Assembly Conference Abstracts*, *EGU General Assembly Conference Abstracts*, vol. 14, edited by A. Abbasi and N. Giesen, p. 11861, 2012.
- Strelnikov, B., et al., Spatial and temporal variability of MLT turbulence inferred from in-situ and ground based observations during the WADIS-1 sounding rocket campaign, *Ann. Geophys*, 2017.

- Strelnikova, I., and M. Rapp, Statistical characteristics of PMWE observations by the EISCAT VHF radar, *Annales Geophysicae*, 31(2), 359–375, doi:10.5194/angeo-31-359-2013, 2013.
- Strelnikova, I., M. Rapp, S. Raizada, and M. Sulzer, Meteor smoke particle properties derived from Arecibo incoherent scatter radar observations, *Geophysical Research Letters*, 34(15), doi:10.1029/2007GL030635, 2007.
- Strelnikova, I., et al., Measurements of meteor smoke particles during the ECOMA-2006 campaign: 2. Results, *Journal of Atmospheric and Solar-Terrestrial Physics*, 71(3-4), 486–496, 2009.
- Szewczyk, A., Mesospheric Turbulence: The Role in the Creation of Mesospheric Inversion Layers and Statistical Results, Ph.D. thesis, University Rostock, 2015.
- Szewczyk, A., B. Strelnikov, M. Rapp, I. Strelnikova, G. Baumgarten, N. Kaifler, T. Dunker, and U. P. Hoppe, Simultaneous observations of a Mesospheric Inversion Layer and turbulence during the ECOMA-2010 rocket campaign, *Annales Geophysicae*, 31(5), 775–785, doi:10.5194/angeo-31-775-2013, 2013.
- Szuszczewicz, E. P., Area Influences and Floating Potentials in Langmuir Probe Measurements, *Journal of Applied Physics*, 43(3), 874, doi:10.1063/1.1661297, 1972.
- Tatarskii, V., The effects of the turbulent atmosphere on wave propagation, *Program for Scientific Translations. U.S. Department of Commerce*, pp. 74–76, doi:10.1017/CBO9781107415324.004, 1971.
- Thomas, L., and M. R. Bowman, Model studies of the D-region negative-ion composition during day-time and night-time, *Journal of Atmospheric and Terrestrial Physics*, 47(6), 547–556, doi:10.1016/0021-9169(85)90037-6, 1985.
- Thrane, E., and B. Grandal, Observations of fine scale structure in the mesosphere and lower thermosphere, *Journal of Atmospheric and Terrestrial Physics*, 43(3), 179–189, doi:10.1016/0021-9169(81)90037-4, 1981.
- Thrane, E., T. Blix, U.-P. Hoppe, F.-J. Lübken, W. Hillert, G. Lehmacher, and D. Fritts, A study of small-scale waves and turbulence in the mesosphere using simultaneous in situ observations of neutral gas and plasma fluctuations, *Journal of Atmospheric and Terrestrial Physics*, 56(13-14), 1797–1808, doi:10.1016/0021-9169(94)90011-6, 1994.
- Toon, O. B., and N. H. Farlow, Particles Above the Tropopause: Measurements and Models of Stratospheric Aerosols, Meteoric Debris, Nacreous Clouds, and Noctilucent Clouds, *Annual Review of Earth and Planetary Sciences*, 9(1), 19–58, doi:10.1146/annurev.ea.09.050181.000315, 1981.
- Torrence, C., and G. Compo, A Practical Guide to Wavelet Analysis, *Bulletin of the American Meteorological Society*, 79(1), 61–78, 1998.
- Tseraskii, V., Luminous clouds, *Ann Observ Moscow*, 1890.
- von Cossart, G., J. Fiedler, U. von Zahn, G. von Cossart, J. Fiedler, and U. von Zahn, Size distributions of NLC particles as determined from 3-color observations of NLC by ground-based lidar, *Geophysical Research Letters*, 26(11), 1513, doi:10.1029/1999GL900226, 1999.

- Von Zahn, U., and T. Hansen, Sudden neutral sodium layers: a strong link to sporadic E layers, *Journal of Atmospheric and Terrestrial Physics*, 50(2), 93–104, doi:10.1016/0021-9169(88)90047-5, 1988.
- von Zahn, U., G. von Cossart, J. Fiedler, K. H. Fricke, G. Nelke, G. Baumgarten, D. Rees, A. Hauchecorne, and K. Adolfsen, The ALOMAR Rayleigh/Mie/Raman lidar: objectives, configuration, and performance, *Annales Geophysicae*, 18(7), 815–833, doi:10.1007/s005850000210, 2000.
- Vondrak, T., J. M. C. Plane, S. Broadley, and D. Janches, A chemical model of meteoric ablation, *Atmos. Chem. Phys. Atmospheric Chemistry and Physics*, 8, 7015–7031, 2008.
- Wallace, L., and L. Wallace, The OH nightglow emission, *Journal of the Atmospheric Sciences*, 19(1), 1–16, doi:10.1175/1520-0469(1962)019<0001:TONE>2.0.CO;2, 1962.
- Weinstock, J., On the Theory of Turbulence in the Buoyancy Subrange of Stably Stratified Flows, *Journal of the Atmospheric Sciences*, 35(4), 634–649, doi:10.1175/1520-0469(1978)035<0634:OTTOTI>2.0.CO;2, 1978.
- Wilms, H., M. Rapp, and A. Kirsch, Nucleation of mesospheric cloud particles: Sensitivities and limits, *Journal of Geophysical Research: Space Physics*, 121(3), 2621–2644, doi:10.1002/2015JA021764, 2016.
- Witt, G., The nature of noctilucent clouds., *Space Research*, (IX), p. 157 – 169, 1969.
- Yamamoto, M., A Moment Method of the Log-Normal Size Distribution with the Critical Size Limit in the Free-Molecular Regime, *Aerosol Science and Technology*, 48(7), 725–737, doi:10.1080/02786826.2014.922161, 2014.
- Zeller, O., M. Zecha, J. Bremer, R. Latteck, and W. Singer, Mean characteristics of mesosphere winter echoes at mid- and high-latitudes, *Journal of Atmospheric and Solar-Terrestrial Physics*, 68(10), 1087–1104, doi:10.1016/j.jastp.2006.02.015, 2006.

Acknowledgments

First of all I would like to thank Prof. Dr. Franz-Josef Lübken for giving me the great opportunity to work in the rocket group as part of his department and his willingness to supervise this thesis. I always appreciated his sense for the significant matters. I am grateful to Dr. Boris Strelnikov who guided me through the past years with good advises, unswerving patience and great ideas. In case of problems or questions, Boris was available anytime. I thank Hans-Jürgen Heckl and Torsten Köpnick for making scientists dreams come true and their readiness to help in the laboratory or giving insights into instruments circuitry anytime. Completing the rocket group, I thank Tristan Staszak my PhD-student companion for fruitful discussions, great teamwork and his friendship.

I thank Prof. Dr. Martin Friedrich from Technical University of Graz, for his readiness to share his tremendous knowledge about rocket science and for helpful comments on the text. I thank Prof. Dr. Scott Robertson and Prof. Dr. Zoltan Sternovsky from University of Colorado, Boulder for hosting me and teaching me so much things.

I thank the DLR-Moraba (Mobile rocket base) for being great team players and helping to lift science into near space.

I would like to thank IAP students and former staff, especially Carsten Schult, Carsten Baumann, Svenja Sommer and Sven Willhelm for their friendship and making the everyday work even more interesting.

Last but not least I am thankful to my family for supporting me through all this years, especially I am grateful to my wife Maria for taking me the way I am and her great heart.

Erklärung

Hiermit versichere ich, dass ich die vorliegende Arbeit selbstständig angefertigt und ohne fremde Hilfe verfasst habe, keine außer den von mir angegebenen Hilfsmitteln und Quellen dazu verwendet habe und die den benutzten Werken inhaltlich oder wörtlich entnommenen Stellen als solche kenntlich gemacht habe.

Die Arbeit wurde bisher weder im Inland noch im Ausland in gleicher oder ähnlicher Form einer anderen Prüfungsbehörde vorgelegt. Weiterhin erkläre ich, dass ich ein Verfahren zur Erlangung des Doktorgrades an keiner anderen wissenschaftlichen Einrichtung beantragt habe.

Kühlungsborn, den 22.06.2018

Lebenslauf

Name	Heiner Asmus
Geburtsdatum	29.07.1986
Geburtsort	Wismar, Deutschland
Familienstand	verheiratet
Staatsangehörigkeit	Deutsch
Wohnsitz	Rostock, Deutschland
1993 – 1998	Grundschule, Kirchdorf/Poel
1998 – 2006	Gymnasium am Sonnenkamp, Neukloster
Juli 2006	Abitur
2006 – 2007	Fachkraft für Veranstaltungstechnik, Rostocker Messe- und Stadthallengesellschaft mbH
2007 – 2010	Bachelor of Science Studiengang Physik, Universität Rostock
2010 – 2012	Master of Science Studiengang Physik, Universität Rostock Masterarbeit zum Thema: "Aerosolpartikel in der mittleren Atmosphäre: In situ Messungen und mikrophysikalische Modellerierung"
seit Oktober 2012	Promotion im Studienfach Physik am Leibniz-Institut für Atmosphärenphysik an der Universität Rostock e.V., Anfertigung der Dissertation
April-Juli 2013	Gastwissenschaftler am Laboratory for Atmospheric & Space Physics, University of Colorado, Boulder, Colorado, USA